Università
Ca'Foscari
Venezia

Scuola Dottorale di Ateneo
Graduate School

Dottorato di ricerca
in Scienze Chimiche
Ciclo XXVII
Anno di discussione 2016

Inorganic nanosized UV filters for cosmetic applications

SETTORE SCIENTIFICO DISCIPLINARE DI AFFERENZA: CHIM/02
Tesi di Dottorato di Gloria Zaccariello, matricola 826290

Coordinatore del Dottorato	**Tutore del Dottorando**
Prof. Maurizio Selva	**Prof. Alvise Benedetti**

ABSTRACT

The PhD thesis was focused on the study of inorganic UV filters to apply in cosmetic and skin care formulations for the protection of human skin against UV radiations.
The importance of this topic is the need to optimize the solar protection formulations commercialized by the cosmetic companies, ensuring maximum protection of the skin and making products more effective and safe.

With this aim, the research project was based on the development of an innovative system, with a wide range of UV shielding and, at the same time, with a reduced photocatalytic activity. In particular, the research project included the synthesis and characterization of nanosized titania-based UV filters. The use of nanosized UV filters is necessary to avoid the so called “whitening effect” on the skin. However, the use of nanosystems is limited by the high photocatalytic activity that they show under UV irradiation, with the consequent degradation or the chemical transformation of the organic molecules present in the cosmetic formulations.

In this thesis, different strategies were considered, using mesoporous silica particles as matrix for the growth of the inorganic filter.

Firstly, mesoporous silica particles were loaded with titanium dioxide nanoparticles at different concentration. It was demonstrated that, even at the lowest concentrations, the samples show a high photocatalytic activity, since the active phase is available to the external environment

Secondly, the silica/titania-based systems were covered with a layer of non porous silica, in order to avoid the direct contact between the active phase and the external environment. This coating does not affect the UV properties of the system.

During the third phase, an innovative method was developed, by adding a bismuth salt to the silica/titania-based system. This procedure allowed to obtain bismuth titanate-based self-sealing nanomaterials. In fact, exploiting the capacity of the low-melting bismuth towards the silica matrix, a system with the active phase trapped within the silica structure and not accessible to the molecules present in the external environment was formed. In addition, the bismuth titanate offers interesting shielding properties, with a higher absorption compared to the commercial products. In conclusion, bismuth ions have a key role in the formation of a filter with enlarged UV properties and reduced the photocatalytic activity. For these reasons, the proposed nanosystem is a suitable candidate for the development of the next-generation for the sun shields.

In order to verify the applicability of the bismuth titanate-based UV filter, the research activity also dealt with several preliminary studies related to the biological effect of the samples kept in contact with cells. The results did not show no particular effects.

Finally, in order to evaluate the characteristics of the synthesized filter in a real system, a cosmetic prototype was formulated. The results related to SPF (Sun Protection Factor), UVA protection, critical wavelenght (λc), viscosity (η) and pH were compared to that of a commercial product, showing excellent properties.

In conclusion, the results indicate that the bismuth titanate in silica matrix can represent a valid alternative to the traditional materials based on titanium bioxide and zinc oxide. In fact, the interesting properties emerged from this study can be widely exploited in the design of a wide range UV filter nanomaterials with the aim of cutting their photocatalytic ability.

ESTRATTO IN LINGUA ITALIANA

Obbiettivo di questo lavoro di tesi è lo studio e lo sviluppo di filtri inorganici da applicare in formulazioni cosmetiche per la protezione della pelle contro gli effetti delle radiazioni ultraviolette. L'importanza di questa tematica di ricerca è dovuta alla necessità di ottimizzare le formulazioni cosmetiche presenti oggi in commercio, per assicurare la massima protezione della pelle e per realizzare prodotti più efficaci e sicuri.

A tal fine, l'attività di dottorato si è basata sullo sviluppo di un sistema innovativo, con un ampio intervallo di schermatura UV e allo stesso tempo con una ridotta attività fotocatalitica. Nello specifico, il progetto di ricerca ha previsto la sintesi e caratterizzazione di filtri ultravioletti a base di nanoparticelle di titania. L'uso di filtri solari inorganici in forma nanoparticellare è reso necessario per evitare il cosiddetto "effetto sbiancante" sulla pelle. Tuttavia, l'utilizzo di nanosistemi è limitato dall'elevata attività fotocatalitica che essi presentano nel momento in cui vengono sottoposti a radiazione ultravioletta, inducendo la conseguente degradazione o trasformazione delle molecole organiche presenti nelle stesse formulazioni cosmetiche.

In questo lavoro di tesi, sono state prese in considerazione diverse strategie, utilizzando particelle di silice mesoporosa come matrice in cui far crescere il filtro inorganico.

Nella prima fase del lavoro, sono state sintetizzate nanoparticelle di silice mesoporosa caricate con nanoparticelle di titania a diversa concentrazione. E' stato dimostrato che, anche alle concentrazioni inferiori, i campioni presentano un'elevata attività fotocatalitica, poiché la fase attiva è disponibile all'ambiente esterno.

Nella seconda fase, i filtri a base di silice e titania sono stati rivestiti con una strato sottile di silice non porosa, grazie al quale è stato possibile evitare il contatto diretto tra la fase attiva e l'ambiente circostante. I risultati emersi hanno dimostrato l'effettiva efficacia del rivestimento di silice con un abbattimento completo dell'attività fotocatalitica. Tale rivestimento, inoltre, non ha pregiudicato la proprietà UV del sistema.

Nella terza fase, si è cercato di mettere a punto un metodo innovativo, aggiungendo al sistema silice-titania un sale di bismuto. Tale procedura ha permesso di ottenere dei nanomateriali autosigillanti a base di titanato di bismuto. Infatti, sfruttando la capacità basso fondente del bismuto nei confronti della matrice di silice, si viene a formare un sistema in cui la fase attiva risulta intrappolata all'interno della struttura silicea e non raggiungibile dalle molecole presenti nell'ambiente esterno. Inoltre, il titanato di bismuto offre interessanti proprietà schermanti, con un assorbimento maggiore dei prodotti commerciali. Il doppio ruolo degli ioni bismuto nell'aumento delle proprietà UV e nell'abbattimento dell'attività

fotocatalitica fa sì che il nanosistema proposto sia un perfetto candidato per lo sviluppo di filtri ultravioletti di prossima generazione.

Con lo scopo di verificare l'applicabilità dei filtri a base di titanato di bismuto, l'attività di ricerca ha previsto una serie di studi preliminari relativi alla valutazione degli effetti biologici dei campioni messi a contatto con cellule. I risultati ottenuti non hanno evidenziato particolari criticità.

Infine, per poter valutare le caratteristiche del filtro UV in un sistema reale, è stato realizzato un prototipo cosmetico industriale. I risultati relativi ai valori SPF (Solar Protection Factor), protezione UVA, lunghezza critica (λc), viscosità (η) e pH sono stati confrontati con quelli di un prodotto solare commerciale, dimostrando ottime proprietà.

I risultati ottenuti indicano che il titanato di bismuto in silice può rappresentare una valida alternativa ai materiali tradizionali a base di biossido di titanio o ossido di zinco. Infatti, le interessanti proprietà emerse da questo studio possono essere ampiamente sfruttate nell'ambito dei filtri solari con l'obbiettivo di abbattere il fotodegrado delle matrici organiche presenti nella formulazione.

Table of contents

1 INTRODUCTION

1.1 Structure of the thesis

The PhD thesis is structured in eight chapters. In particular, the first chapter is dedicated to the introduction, in which the main topics developed during the research activity have been addressed, *i.e.* UV radiations (UVR) and their effects on human health, inorganic UV filters in sunscreen formulations, mesoporous silica nanoparticles as matrix for the embedding of inorganic sunblocks.

The second chapter concerns the materials and methods section, in which the utilized reagents and the description of the characterization methods are reported.

The third, fourth and fifth deals with synthesized nanostructured silica-based systems. For each chapter, the reason of the investigation, an accurate description of the followed synthesis processes, the obtained results and the conclusions about the study are presented.

In the sixth chapter preliminary results of *in vitro* tests on culture of human cells are reported, with a particular focus on the metabolic activity, the apoptosis and the oxidative stress of the cells exposed to the samples.

In the seventh chapter, the preparation of a solar protection prototype formulated in collaboration with an italian dermo-cosmetic company, is described, comparing it to a commercial formulation.

The eight chapter sums up the obtained results with the general conclusions and contains future perspectives to develop and improve the system proposed.

1.2 Aim of the thesis

The PhD thesis is focused on the study of inorganic UV filters to be used in cosmetic and skin care formulations for the protection of human skin against UV radiations.

In particular, the research project was based on the synthesis and characterization of nanostructured UV filters. The aim was to develop an innovative inorganic sunblock, with a wide range of ultraviolet protection and, at the same time, a reduced photocatalytic activity. In

order to verify the applicability of the studied materials, the research activity also dealt with the citotoxicity tests and the formulation of cosmetic prototypes.

The importance of this topic is the need to optimize the solar protection formulations commercialized by the cosmetic companies, ensuring maximum protection of the skin and making products more effective and safe.

The application of nanosized inorganic UV filters in cosmetic field is limited by their photocatalytic activity, that could induce the degradation or dangerous transformation of the organic molecules in sunscreen formulations. In order to overcome such problem and simultaneously spread the window of filter's absorption, different strategies were considered and developed during the research activity.

1.3 Health effects of UV radiation

1.3.1 The skin

The skin is the largest organ of the human body and it represents the 16% of its mass.[1] It covers the entire external surface of the body, acting as a waterproof, insulating shield, guarding the body against temperature extremes, bacteria, toxins, damaging sunlight and harmful chemicals.[2] The integument is made up of two layers: the dermis, a deeper skin layer, and the epidermis, the outermost stratum (Figure 1).[3]

The underlying dermis has a thickness of few millimetres and has the primary function of acting as support for the epidermis. It is constituted by several structural components, such as collagen, elastic fibers, and extrafibrilliar matrix.[4]

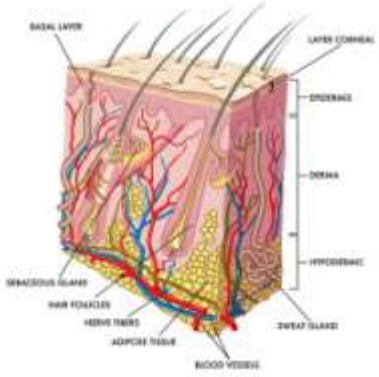

Figure 1 Cross section of human skin.

The epidermis is a stratified squamous ephitelium of about 70 μm[4] and it is formed by four sublayers named as stratum corneum, stratum granulosum, stratum spinosum, and stratum geminativum. Keratinocytes are the most important cell type that constitute approximately 95% of the total epidermal cells and they are made from the tough protein keratin present in the basal layer. In this bottom layer is also present the second most important cell type known as melanocytes. The basic features of these cells are the ability to synthesize melanin, the main pigment present in the skin that absorbs and scatters radiant energy from the sun and protect the skin from the dangerous effects of UV radiations.[2a, 5] Melanin represents the main factor that determines skin complexion, according to which people can be classified in six phototypes, as described by *Fitzpatrick Scale.* Fitzpatrick skin typing is useful to predict the possible sun damage in a person and the risk of skin cancer (Table 1).[6]

Table 1 Skin phototype classified by Fitzpatrick scale.

Phototype	Skin type	Tan	Burns	Individual groups, ethnicity
I	Very white	No	Always	Red hair, freckled, basques
II	White	Minimum	Very easily	Nordic and central European
III	Slightly brown	Gradual	Easily	Blonde hair/brunette
IV	Brown	Yes	Occasionally	Latin
V	Brown to black	Intense and fast	Rarely	Arab, Asian, Indians
VI	Black	Maximum	Never	Black

1.3.2 UV radiation

In the past, humans were exposed to solar radiations because of outdoors work activities. Since the twenties, instead, the UV exposure became a recreational activity to reach a certain tanning, culturally associated with health and well-being.[1] Furthermore, since the eighties, also the tanning indoor has became very popular for fashion and cosmetic purposes. Exposure to UV radiation led few benefit to human health, *i.e.* the synthesis of vitamin D; nevertheless, an excessive or wrong exposure, either from the direct sunlight or from artificial sources, causes several detrimental effects.[7]

As shown in Figure 2, solar radiation is divided in infrared radiation (700 nm-1 mm), that generate warmth; visible radiation (700-1 nm), which allow to distinguish colours; and ultraviolet radiation (10-400 nm), able to penetrate the skin in a wavelength-dependent manner (Figure 3), inducing deleterious photodamages and several consequences on cells, tissues and molecules.[1] In fact, the UVR is the most dangerous type of solar radiation and for this reason it is classified as carcinogenic.

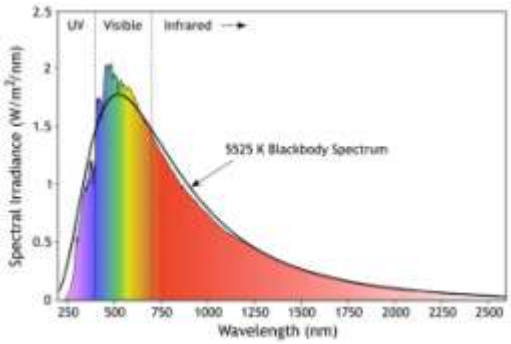

Figure 2 Solar radiation.

The UV region can be divided in UVA (320-400 nm), UVB and UVC components, based on their electro physical properties. The longer wavelength UVA (320-400 nm), further divided into UVA-I (340-400 nm) and UVA-II (320-340 nm), represents the most radiation that reaches the Earth's surface (95%). UVA is the radiation with the lower energy and it can penetrate the epidermis to reach the underlying dermis. UVA, through the promotion of the generation of reactive oxigen species (ROS), can damage DNA with indirect photoreactions. The wavelength UVB (280-320 nm) is able to alter the DNA from which it is absorbed. Mutations and cancer are the direct and detrimental results caused by these modifications of DNA. The shorter wavelength UVC (200-280 nm) is almost completely screened by atmospheric ozone layer.[1] Figure 3 reports a scheme of the effects of the UVR on the skin.

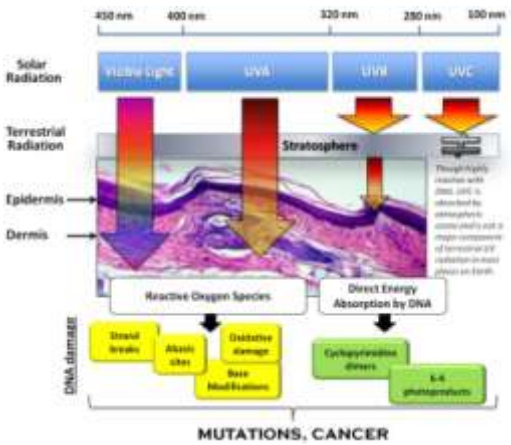

Figure 3 Penetration and effects on the skin of the different components of UVR.

1.3.3 UV radiation damages on the skin

Sunburn inflammation and tanning are among the major acute clinical consequences to a UVR overexposure. Sunburn inflammation is caused by keratinocytes apoptosis, provoking oedema (swelling) and erythema (reddening), the most conspicuous and well recognized cutaneous damages, especially in fair-skinned people. Tanning is a biphasic process. Firstly there is an immediate pigment darkening (IPD) with an alteration and redistribution of epidermal melanin, and secondly the synthesis of new melanin occurs.

UV irradiation led also to histological effects, such as hyperkeratosis, the thickening of epidermis and dermis, and to photoaging, manifested by the appearance of wrinkles, spots, freckles, moles and loss of skin elasticity.

However, the most dangerous risk factors induced by UVR are the development of melanoma and non-melanoma skin cancers (NMSCs), schematically illustrated in Figure 4. Melanoma is the deadliest skin cancer derived by melanocytes.[5a] NMSCs are the most frequent skin cancer and comprise two main types of malignant tumour that arise from epidermis and that are known as basal cell carcinoma (BCC) and squamous cell carcinoma (SCC). BCC and SCC present different distributions on human body and aetiological factors: while BCC is extremely locally invasive and destructive, but only rarely metastates, SCC has a destructive growth and it metastatizes.[8]

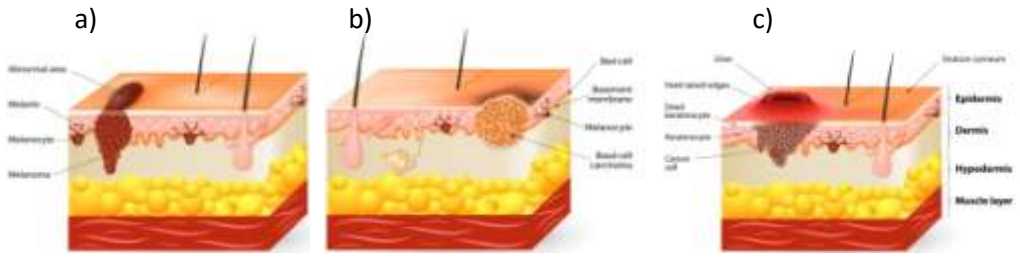

Figure 4 Schematic representation of melanoma (a), basal cell carcinoma (b) and squamous cell carcinoma (c).

1.4 Sunscreen

To avoid sunburns and to protect skin from the harmful effects of UVR, as previously discussed in 1.3, certain precautions must be taken. Besides wear clothes, hats and sunglasses, people should apply on skin a solar protection during sun exposure. Therefore, the rising awareness about the above-mentioned effects extended the widespread use of the sunscreen products, as a tool to prevent skin also in our daily life.

For a total protection against UV damages, a sunscreen must have some requirements. Firstly, they have to contain UV filters, as active ingredients, with a broad-spectrum sunscreen in order to prevent erythema and cell damages, minimizing the extent of UVR that might reach DNA in cell nuclei. The efficacy of a sunscreen is evaluated by its ability to protect the skin against both UVA and UVB and it is defined by its SPF (Sun Protection Factor) and by UVA Protection Factor (UVA-PF), as described in 1.4.3. For this reason the research is evolving towards the synthesis of broad-spectrum sunscreens.[9]

Secondly, the sunscreens have to contain inert and safe ingredients. In the specific case of the UV filters, they must be photostable (ideally 100%) and to rule out the formation of singlet oxygen or other reactive oxygen species and harmful reactive intermediates, they must dissipate the absorbed energy efficiently through photophysical and photochemical pathways. Therefore, they should not penetrate into the skin layers, and they should not be transported into the human cells where they can lead to deleterious damage to DNA.[10]

Finally, a sunscreen formulation has to satisfy some aesthetic targets, such as skin feel, transparency, fragrance, color and appearance. In particular, the sensory properties strongly influence the amount and the frequency of application of the sunscreen: to be very effective, the sunscreen formulation has to be spread roughly 2 mg/cm^2 as uniformly as possible. In order to achieve a uniform coating, the sunscreen formulation is designed to have a very specific rheological profile.[11] If these advices are not respected, the sunscreen will provide insufficient protection.[12]

1.4.1 Sunscreen formulation

A typical commercial sunscreen contain at least four main components: UV filters, water, emollients and emulsifiers.[9a] As described below, each of them has a specific role and must be present in a certain amount.

(i) *UV filters (10-20 wt%)*. They represent the active ingredients of a sunscreen formulation. To achieve a strong protection, a high concentration of UV filters is required.

(ii) *H_2O (60-*80 *wt%)*

(iii) *Emollients (≈15 wt%).* Usually they are constituted by esters or hydrocarbons. They have a triple role: to constitute the oil phase that solubilizes the filter; to photostabilize; and to enhance the sensorial properties, providing a light and no greasy skin feel.

(iv) *Emulsifiers (≈5 wt%).* They define the emulsion type, water in oil (W/O) or oil in water (O/W). O/W emulsions are preferred for their easier spreading and lighter skin feel, but they have low water resistance, as opposed to W/O emulsions, used for sunscreens intended for children.

In addition to these main components, there are also other secondary components:

(i) *Reology modifiers.* They are used to give the right viscosity and spreadability. Fumed silica, organophilic clays, waxes and glycerides are used as reology modifiers for W/O emulsions, while emulsions starch, cellulose or hydrophilic clays are generally employed for O/W.

(ii) *Boosters.* They increase the performance of a sunscreen or by boosting the efficacy of the UV filter or by improving the film-forming property on the skin. Hollow particles of styrene/acrylates copolymer increase optical pathlength of radiation due to their scattering properties, thereby increasing the probability of UV light meeting a UV filter molecule before reaching the skin surface.

(iii) *Sensory enhancers.* They have to make the formulation aesthetically appealing for the user. They mainly are silicone powders that absorb oil, ease the spreadability, provide a matte and powdered finish, and give a velvety touch.

Figure 5 summarizes the ingredients and their function of a typical sunscreen, including both the main and the secondary components.

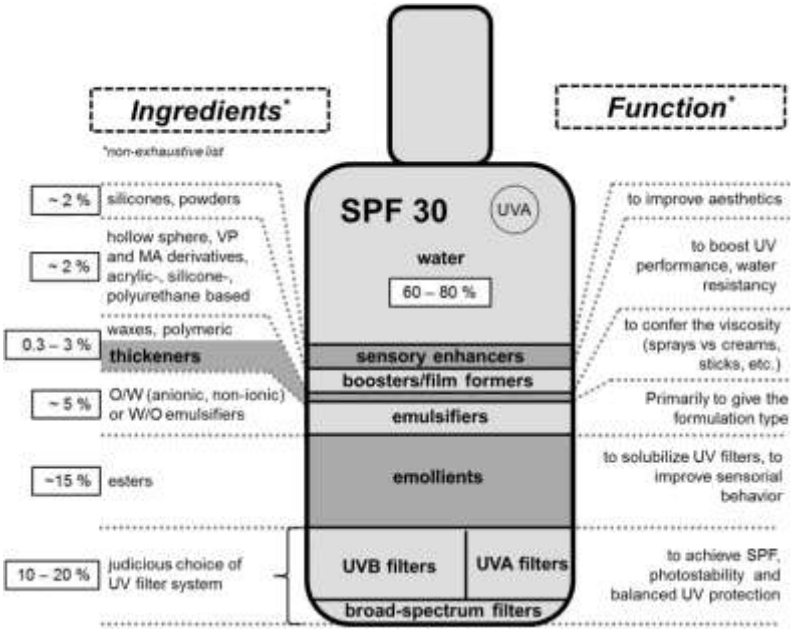

Figure 5 Ingredients and their function in a typical sunscreen formulation.

1.4.2 UV filters

A good UV filter should prevent the transmission of the light in the range between 290 and 400 nm range, by absorbing, reflecting or scattering the light. Usually, it is soluble in water or in oil phase, or it can be embedded into sunscreen formulation as a dispersion of fine particles.

A typical sunscreen contains two basic kind of UV filters as active ingredients: organic (or chemical) and inorganic (or physical) ones.[10]

Organic filters include aromatic compounds and, according to their chemical structure, they are able to absorb UVR energy within a specific wavelength: for this reason, usually, in a sunscreen formulation there is more than one organic filter to screen the whole range of UV radiation. The intensity of their absorption depend on the number of resonance structure. They often have an electron donor and an electron acceptor group in para position (push-pull systems). When UV radiation is absorbed, electrons are excited from the π HOMO orbital to the π* LUMO orbital. Then, they return to the ground state following three different pathways: the radiative decay (fluorescence), the non-radiative decay (heat) and the structural degradation (photochemistry).[10] If the latter pathway occurs, the filter is not photostable, compromising its screening properties. Their photodegradation produces reactive intermediates that can be absorbed thought the skin, causing photoallergy, phototoxic reaction and skin irritation.[13] Recently, in order to protect the organic UV filters against chemical degradation, some strategies are developing, such as the use of hydrotalcite-like compounds or MSN as matrix to host the organic UV filters.[14]

Organic UVB filters absorb 90% of the radiation with wavelength between 290 and 320 nm. P-amino-benzoic acid (PABA) was the first organic UV filter approved by the FDA (American Food and Drug Administration) in 1943,[9b] but recent studies have shown that it induces allergenic reactions.[15] The most used UVB filters are cinnamates, due to their low risk to cause skin irritability. Octyl methoxicinnamate (2-ethylhexyl 4-methoxycinnamate) could be the most powerful UVB filter, capable of absorbing in the wavelength range between 270 and 328 nm; but, it is strongly photounstable and it isomerizes from the trans form to the cis one, losing its effectiveness. Salicylates absorb in the 290-315 nm range and they are stable and safe, used also as solvents for poorly soluble sunscreens.

Figure 6 reports the above-mentioned organic UVB filters.

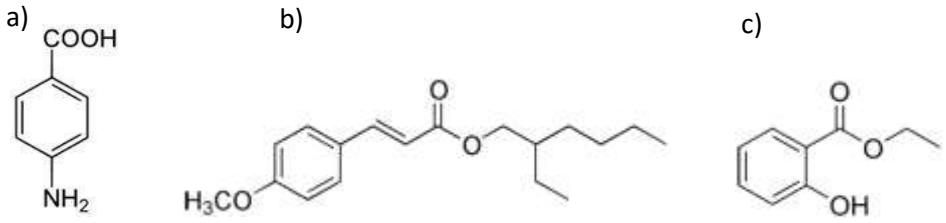

Figure 6 Organic UVB filters: PABA (a), octyl methoxicinnamate (b) and salicylate (c).

Among organic UVA filters, used starting from 1979,[9b] there are oxybenzone, avobenzone and terephthalylidene dicamphor sulfonic acid (Figure 7). Oxybenzone is an aromatic ketone, approved by FDA in the early 80s, that absorbs between 270 and 350 nm. Avobenzone was introduced in the late 80s and it was the first to provide a photoprotection in 310-400 nm range, but it suffers of significant degradation under UV irradiation, that lead to photocontact dermatitis.[16]. Terephthalylidene dicamphor sulfonic acid is a UVA filter that absorbs in the range 290-390 nm. It was recently developed by L'Oréal® and approved by FDA in 2006.[17]

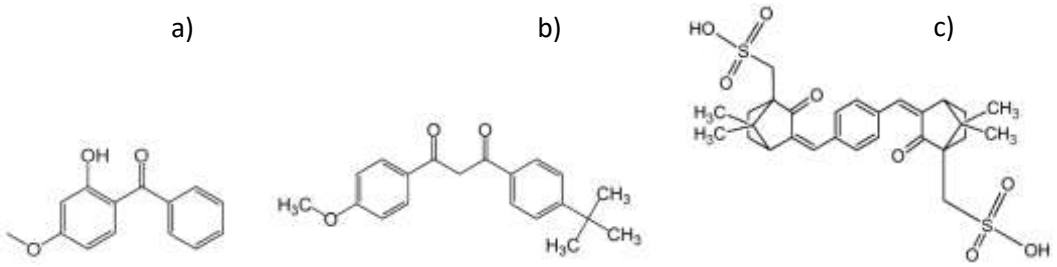

Figure 7 Organic UVA filters: oxybenzone (a), avobenzone (b) and terephthalylidene dicamphor sulfonic acid (c).

Metal oxides, able to absorb, scatter and reflect the light depending on the size of the particles, constitute the inorganic filters, also known as physical sunscreens. They present some advantages over organic filters, such as photostability, non-irritability and broad spectrum protection. These peculiar properties make the inorganic filters as suitable active ingredients also for children or people with sensitive skin.[17] Detailed discussions about the inorganic filters will be reported in 1.5.

1.4.3 The Sun Protection Factor

The Sun Protection Factor (SPF) is an indicator of the effectiveness of a sunscreen, and it is defined as the *ratio* between the Minimum Erythemal Dose (MED) of sunscreen-protected skin (MED_p) and the MED of unprotected skin (MED_u):[18]

$$SPF = \frac{MED_p}{MED_u}$$

Friedrich Ellinger proposed the first calculations of the protective efficacy of a sunscreen were in 1934, according to which the MED of the protected and unprotected skin was evaluated using both forearms and a mercury lamp.

In 1956 Rudolf Schulze introduced the so-called “Schulze factor”, defined as the *ratio* between the exposure time required for inducing erythema on sunscreen-protected skin (t_p) and unprotected skin (t_u):

$$Schulze\ factor = \frac{t_p}{t_u}$$

In 1974, Franz Greiter adapted earlier determinations developed by Ellinger and Schulze and he introduced the Sun Protection Factor. In 1978, the FDA proposed the first normatization to evaluate the SPF, in order to standardize the method and to have reliable values.[9b]

The SPF rating can be measured both *in vivo* and *in vitro*, even if *in vitro* methods do not yet fit with *in vivo* methods, tending to overestimate the SPF value for low protection sunscreens and underestimate it for medium and high protection sunscreens.[19]

- *SPF in vivo*[1]: a group of 10-20 volunteers with skin phototypes I-III is subjected to increasing doses of UVR emitted by a solar simulator,[2] irradiating unprotected and sunscreen-protected skin areas (usually on the back). The amount of sunscreen applied is 2 mg/cm^2. From 16 to 24 hours after exposure, in each area the reading of the MED is evaluated and the relative ratio calculated.[9b]

  Some controversies have arisen about this method:[9c] the SPF rating for the same sunscreen, measured in different laboratories, can vary up to 50%, especially among American and European labs, probably due to the difficulty of a homogeneous amount and application of the sunscreen. Moreover, the spectrum of the source can vary, because the specifications of the reference method about the source are not rigorous enough. Since erythema is mainly caused by UVB, an UVB-biased spectrum of the source will overestimate the SPF for an UVB sunscreen, compared to its performance in the real sunlight.

  In Europe, sunscreens are approved according to four different categories of protection: low (SPF 6-14), medium (15-29), high (30-50) and very high (50+).[9c]

- *SPF in vitro*: due to the disputes about the *in vivo* method, rather expensive and time-consuming, some *in vitro* approaches have been developed by the simulation of the interaction between the sunscreen and the human skin. The *in vitro* methods are based on the measure of the spectral transmittance of the sample in the wavelength range between 290 and 400 nm, as reported in the following formula:[20]

$$SPF = \frac{\int_{290\ nm}^{400\ nm} E_\lambda S_\lambda d\lambda}{\int_{290\ nm}^{400\ nm} E_\lambda S_\lambda T_\lambda d\lambda}$$

  where E_λ is the erythemal spectral effectiveness defined by the International Lighting Commission (CIE), S_λ is the solar spectrum irradiance, and T_λ is the spectral transmittance of the sample.

[1] The reference method wasd approved by the FDA in 1978 and an equivalent method was endorsed by the European Cosmetic, Toiletry and Fragrance Association (Comité de Liason des Associations et Européenes de Industrie et de la Parfumerie - COLIPA) in 2003.

[2] Xenon arc lamp.

Different methods to measure the transmittance can be used. For example, the sample can be dissolved with suitable solvents and placed into a 10 mm pathlength cuvette, made of quartz. A variant of this method, suitable only for non-viscous sunscreens, is to put the sunscreen between two quartz plates and compressed it into a capillary film. Another method is based on the use of a substrate, transparent in the UV range, and similar to human skin morphology. The most common substrates are the Transpore Tape®, a surgical tape with an adhesive side;[21] the Vitro-Skin™, a synthetic skin, but very expensive; and poly(vinyl chloride), an available and low cost material.

1.4.3 The UVA-Protection Factor

The SPF rating is based on erythema as an endpoint[3], that is induced mostly by UVB, and it does not take in consideration protection against UVA. For this reason other parameters, such as UVA ratio or critical wavelength (λ_c), were introduced to evaluate the UVA screening properties of a sunscreen.

The UVA-Protection Factor (UVA-PF) can be determined both with *in vitro* and *in vivo* methods.

- *UVA-PF in vitro*: The Diffey method consist in the *ratio* between UVB vs UVA absorbance[22] as reported in the following formula:

$$\frac{\alpha\ UVA}{\alpha\ UVB} = \frac{\int_{320\ nm}^{400\ nm} A_\lambda d\lambda}{\int_{290\ nm}^{320\ nm} A_\lambda d\lambda}$$

where A_λ is the value of absorbance at each wavelength.

According to the UK Boot's Star System,[23] at each UVA *ratio* value corresponds a description and a number of stars that indicates the level of UVA protection, as shown in Table 2.

[3] In a clinical research trial, a clinical endpoint generally refers to occurrence of a symptom or sign that constitutes one of the target outcomes of the trial.

Table 2 Level of UVA protection according to UK Boot's Star System

UVA ratio	Star	Level of UVA protection
0.0-0.2	-	Low
0.2-0.4	*	Moderate
0.4-0.6	**	Good
0.6-0.8	***	Superior
>0.8	****	Maximum

Another method to measure the UVA protection is the critical wavelength (λ_c), that is the first value where the *ratio* R is greater than or equal to 0.9.[20] R, calculated for each wavelength, is the *ratio* between the total absorption in incremental wavelength bands and the total UV absorption:

$$R = \frac{\int_{290\ nm}^{\lambda} A_\lambda d\lambda}{\int_{290\ nm}^{400\ nm} A_\lambda d\lambda}$$

According to the European Commission, a sunscreen, which has to provide good UVA protection, must have a λ_c>370 nm.

In order to evaluate the photostability of a sunscreen containing good UVA absorbers, the samples can be pre-irradiated by a solar simulator light source, then the spectral transmittance is measured.

- *UVA-PF in vivo*: the *in vivo* methods to determine UVA protection are limited to non-invasive endpoint measures, namely erythema and pigmentation changes, which differ in immediate and persistent ones. Some examples of methods based on different endpoints are: the sensitized-skin method,[24] the erythema endpoint method,[25] the immediate pigment darkening (IPD) endpoint,[26] and the persistent pigment darkening (PPD) endpoint.[27] A method that does not need a biological endpoint is the diffuse reflectance spectroscopy.[28]

1.5 Inorganic UV filters

Titanium dioxide and zinc oxide are the only compounds approved by the American Food and Drug Administration (FDA) and by European Commission.[29] They are used as nanometric particles to avoid the whitening effect when the sun care formulation is applied on the skin.[30] Nevertheless, since they are semiconductors, when these inorganic materials are exposed to UV light, they become harmful photocatalysts,[31] oxidizing and degrading the organic ingredients of the cosmetic formulation[32] and enhancing the ultraviolet damage to DNA and cells in *in vitro* systems.[33]

In the following paragraphs, an overview on the peculiar properties of these inorganic filters is reported. Since the research activity developed titanium dioxide-based UV filters, a greater attention is given on this material in the further discussion. Finally, the different strategies aimed to reduce the photocatalytic activity of titanium dioxide and zinc oxide and the new candidates, alternative to the traditional inorganic UV filters, proposed in the recent years[14d, 34] are discussed in a summary state of the art.

1.5.1 TiO_2

Overview

Titanium dioxide (TiO_2), also known as titania, is one of the top fifty chemicals produced worldwide with an annual production that exceeds 4 million tons:[35] It is widely used as white pigment and in many other applications, such as self-cleaning coating for windows,[36] biomaterial for orthopedic prosthesis,[37] bone substituent and reinforcing mechanical supports, tumor cells destructive agent,[38] bactericidal agent,[39] catalyst in selective reduction of NO_x to N_2,[35] photocatalyst in environmental decontamination[35] and for UV protection.

Titanium dioxide occurs in three polymorphs: anatase and rutile with a tetragonal crystal system and brookite with an orthorhombic crystal system. Their structure can be explained considering the TiO_6^{4-} octahedral. As shown in Figure 8, each crystalline form differs by the arrangements of TiO_6^{4-}. Anatase is built up from octahedra connected by their vertices, in the rutile form the octahedra are connected by their edges, while in brookite by vertices and edges.[35]

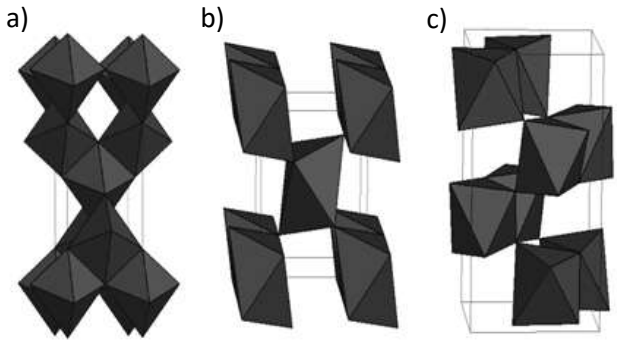

Figure 8 Crystal structures of anatase (a), rutile (b), brookite (c).

Synthesis processes

Titanium dioxide can be prepared as powder, crystals, or thin films. The sol-gel method is usually employed to synthesize powders and thin films due to its several advantages, such as stoichiometric control, flexibility in introducing dopants, purity, homogeneity, ease of processing and control over the composition. In particular, metal alkoxides such as $Ti(O\text{-}Et)_4$, $Ti(i\text{-}OPr)_4$ or $Ti(O\text{-}nBu)_4$ are widely used in the so call alkoxide route. This procedure involves the formation of TiO_2, by hydrolysis and subsequent condensation of titanium alkoxides, leading to polymeric species with -OH or -O- bridges. The titanium alkoxides are readily hydrolized by even traces of water, which initially coordinates to the metal, and then forms a hydrogen bond between one of its proton and an -OR group linked to the metal.[40] These reactions are followed by a thermal treatment (450-600 °C) to remove the organic fraction, with the consequent crystallization of the titanium dioxide. The initial crystalline phase formed with different synthesis methods is anatase, a kinetically stable product, since the octahedra are ordered in a less constrained molecular construction. When temperature reaches about 600°C, anatase begins to transform irreversibly to rutile, with an overall volume contraction of 8%. This transformation is reconstructive, involving not only the distortion of the structure, but also the breaking and reforming of bonds.

The double nature of TiO_2: UV filter vS photocatalist

Titanium dioxide is a semiconductor. When it is irradiated by light with an energy higher than its band gap, the electrons of the valence band can be excited to the conduction one and electron-hole pairs are formed. Its electronic structure makes TiO_2 a suitable material both as UV filter in cosmetic field and as photocatalyst, according to its crystal structure, particle size and surrounding materials.

As inorganic UV filter, titanium dioxide provides a broad spectrum protection, from UVA II to UVB. It can block the light by absorption, scattering and reflection processes, determined by the intrinsic refractive index (2.90), the size of the particles, the dispersion in the cosmetic emulsion and the film thickness when applied on the skin.[41]

The band gap energy depends on the crystal structure of titania: rutile has a band gap energy of 3.0 eV, corresponding to an onset of absorption of 400 nm, while anatase band gap energy is 3.2 eV, with an onset of absorption of 387 nm.

As photocatalyst, titanium dioxide is able to trigger several processes when an electron-hole pair is formed, as illustrated in Figure 9. Firstly, the electron is scavenged by the pre-adsorbed molecular oxygen to yield the superoxide radical anion $^{\cdot}O_2^-$. In acidic media, the $^{\cdot}O_2^-$ can be protonated to give the hydroperoxy radical $HO_2^{\cdot}$ and hydrogen peroxide. Therefore, holes oxidize the surface hydroxyl group to generate hydroxyl radicals $OH^{\cdot}$, which can combine with a radical termination step yielding hydrogen peroxide.[10]

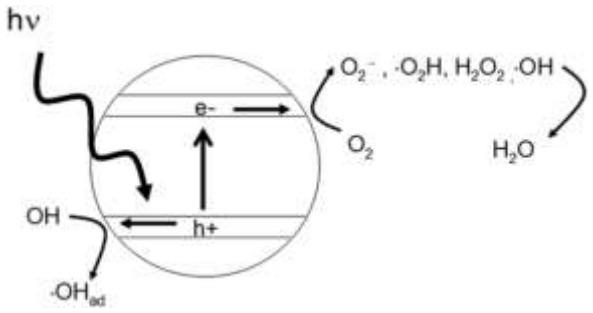

Figure 9 Schematic illustration of photophysical and photochemical events that occur when TiO_2 is photoactivated by the absorption of UV radiation.

From literature, it is well known that titanium dioxide is used as photocatalyst especially for the photodegradation of organic compounds and for environmental decontamination.[42] Both anatase and rutile are commonly used as photocatalyst, but the first one shows a greater efficiency, due to the higher density of localized states and lower rate of electron-hole recombination.[43]

In cosmetic field, the photocatalytic properties of titania represent a significant problem, since the photodegradation of the organic matrixes present into sunscreen formulations can occur. Ricci *et al*.[44] reported a study about the stability of some organic sunscreens in the presence or absence of titania under UVA irradiation: it was demonstrated that without TiO_2 all the organic filters were stable, while in the presence of TiO_2 a great degradation occurred. Serpone and co-workers[32] showed that, in the presence of TiO_2, the photodegradation of oxybenzone was accelerated with a decomposition of 70% after 20 minutes of UV exposure,

while in absence of titania, oxybenzone degraded of 50% after 260 minutes. Another interesting investigation was conducted by Ji *et al*.[45] about the photocatalytic degradation of the organic UV filter 2-phenylbenzimidazole-5-sulfonic acid (PBSA) in aqueous suspension of TiO_2. They obtained that the major responsible species for photocatalytic oxidation of PBSA was the hydroxyl radical $OH^{\cdot}$, but direct hole oxidation through electron transfer was also feasible.

From these studies, it clearly emerges that, when radical species are generated during sun exposure, detrimental and dangerous damages to the sunscreen formulation and consequently to human health can occur; then some strategies have to be adopted to solve this drawback.

Nanosized TiO_2

With the increasing use of nanotechnology, a wide range of cosmetic products contains nanosized particles.[4] In the case of sunscreens, many formulations containing TiO_2 as nanosized particles provide a better performance in UV blocking and avoid the white appearance on the skin when they are applied on the skin, as discussed below.[5] In 2006, the Therapeutic Good Association of Australia estimated that the 70% of TiO_2-based sunscreens contained nanoparticles.[46]

The behavior of TiO_2 nanoparticles as UV filters can be explained by Mie theory.[47] Under 100 nm, the UV attenuation properties change, then, while pigment-grade particles (120-150 nm) scatter 400-nm radiation very efficiently, giving the entire system a white appearance, nanoparticles do not scatter visible light, resulting transparent and avoiding the white effect. On the contrary, at shorter wavelengths, extinction coefficient[6] become higher for smaller

[4] The European Commission Recommendations define a nanomaterial when it meets at least one of the following criteria: (1) it consists of particles with one or more external dimensions in the size range 1-100 nm for 1% of their number size distribution; (2) it has internal or surface structures in one or more dimensions in the size range 1-100 nm; (3) it has a specific surface area higher than 60 m^2/cm^3, excluding materials consisting of particles with a size less than 1 nm.

Furthermore, the Regulation (EC) 1223/2009 of the European Parliament and of the Council established that "all ingredients presented in the form of nanomaterials shall be clearly indicated in the list of ingredients. The names of such ingredients shall be followed by the word 'nano' in brackets.". In 2000, the Scientific Committee on Cosmetic Products and Non-food Products (SC-CNFP) stated that, for the common use in cosmetic products, the maximum concentration of TiO_2 should be limited at 25_{wt}%.

[5] In 2000, the Scientific Committee on Cosmetic Products and Non-food Products (SC-CNFP) stated that, for the common use in cosmetic products, the maximum concentration of TiO_2 should be limited at 25_{wt}%.

[6] Egerton *et al.*[48] carried out a study on the extinction properties of titanium dioxide nanoparticles. According to them, extinction, or attenuation, of the light, is the sum of scattering and absorption, and it is represented by the following equation:

$$-\frac{dI}{I} = f * q_{ext} * dx$$

particles.[48] As the particle size reaches the dimension of about 1/10 of the radiation wavelength (15-50 nm), Rayleigh equation[7] must be used: the scattering power increases as wavelength decreases.[49] So, for 288-nm radiation, the most efficient attenuation is given by 60-nm particles, for 360-nm radiation by 100-nm particles and for 400-nm radiation by 120-130-nm particles.[50]

As the diameter of the crystallite approaches the excitation Bohr diameter (1.5 nm for a TiO_2 nanoparticle), an increase of the band gap value occurs,[8] due to the so-called "quantum size effect". The result of the size quantization is a blue shift of the absorption edge, which becomes a strong function of titania cluster size for diameter less than 10 nm.[51]

Blue shift in the absorption edge is observed in many works. For example, Pan *et al*. reported a blue shift of 0.15 eV for titania nanoparticles, compared to that of bulk anatase;[52] Madhusudan Reddy observed a band gap energy equal to 3.027 eV for 39-nm rutile particles, 3.145 eV for 6-nm particles, and 3.167 nm for 3-nm particles;[51c] Zhao and co-workers obtained a band gap energy shift from 2.96 to 3.05 eV for bulk particles for nanoparticles, respectively;[53] Hernàndez-Perez reported a band gap energy of 3.20 eV for bulk particles, shifted to 3.31 eV for 5-nm particles.[54]

---

where *-dI* is the attenuation of the light by a diluite suspension of particles, *I* is the incident beam, *f* is the volume fraction, *dx* is the distance crossed by the beam, and q_{ext} is the total extinction coefficient, corresponding to the sum of scattering coefficient (q_{sca}) and absorption coefficient (q_{abs}):

$$q_{ext} = q_{sca} + q_{abs} = \frac{C}{V}$$

with *C* the light extinction cross section and *V* the particle volume.

[7] According to Rayleigh equation, for particles smaller than 1/10 of the radiation wavelength λ, scattering coefficient is inversely proportional to λ^4, as described by the following equation:

$$q_{sca} \propto \frac{K}{\lambda^4}$$

where *K* is a constant depending on refractive index.

[8] The increase in the energy gap ΔE_g is related to the particle radius *R*:

$$\Delta E_g = \frac{h}{8R^2}\left\{\frac{1}{m_e} + \frac{1}{m_h}\right\}$$

where *h* is the Planck constant and m_e and m_h are the effective masses of electrons and holes.

1.5.2 ZnO

Zinc oxide (ZnO) represents another UV-absorbing compound, extensively used as agent to attenuate the UV radiation due to many desirable peculiarities, such as a long history of topical use, broad spectrum absorption, high photostability and low irritancy.[55]

Zinc oxide has a long history of safe use in cosmetic field: it is not irritating and compatible with sensitive skin, so that it is just used as skin protectant, anti-irritant, and substance to treat various forms of dermatitis or skin irritation, including diaper rash.[56]

As a single active ingredient, zinc oxide is the broadest range sunscreen, with a broad range of effectiveness, that covers UVB as well as UVA (both UVA I and UVA II).[57]

The main disadvantage of the zinc oxide-based sunscreens is the white residue, left when it is applied on skin. As previously discussed also for the titanium dioxide, the concentrations of UV filter required for a high degree of protection inevitably lead some whitish effect.[10] This problem has been exceeded by the use of zinc oxide nanoparticles that have different optical properties.

As explained for TiO_2, zinc oxide nanoparticles is able to promote the generation of free radicals and increase the risk of mutations.[58]

1.5.3 Strategies and new inorganic UV filters

Recently, as reported in literature, several strategies have been considered to solve the drawback about the photocatalytic activity of TiO_2 and ZnO.

Corazzari *et al.*[34b] tried to inactivate TiO_2 nanoparticles (Degussa, P25, Germany) *via* carbon-based surface modification, exploring the efficacy of several organic modifiers (*i.e.* ethanol, glycolic acid, citric acid and ethylene glycol). The findings indicate that the modification with the organic molecules that have oxygenated functionalities, such as hydroxyl or carboxyl groups, in a vicinal position inhibits both reductive and oxidative activity of the photocatalyst, while the generation of singlet oxygen is still noticed. The effect may be correlated to the presence of both carbonaceous residues, that probably act as scavengers of free radicals, and carboxylate/carbonate species adsorbed at the surface behaving as a protective coating. Among the different organic modifiers tested, ethylene glycol results to be the most promisining. However, the modified TiO_2 powders are still far from commercial use since adequate coatings are needed to make the powders compatible and suitable with the emulsions used in cosmetic preparations.

A different method was adopted by Ukmar *et al.* that coated the TiO_2 nanoparticles (Degussa, P25, Germany) with a silica layer, selecting lauric acid as model stabilizer.[34c] The functionalized TiO_2 nanoparticles exhibited significantly reduced agglomeration, both in dry and in dispersed oily media states. The reduced tendency towards agglomeration is consistent with the increased hydrophobicity of functionalized TiO_2 confirmed by contact angle measurements. Furthermore, the strong covalent bonding greatly improved the stability of the sample in suspensions. Finally, the UV shielding efficiency of functionalized samples was much improved when compared to non-functionalized or tho the samples functionalized with conventional stabilizers based on adsorption method.

Luo *et al.* modified the surface chemistry of ZnO powder (Micronisers Australasia Pty Ltd, Dandenong, Victoria, Australia) by PEGylation.[59] The authors demonstrated that the surface chemistry of nanoparticles have a significant role in citotoxicity response. PEGylated ZnO nanoparticles showed a reduced cytotoxicity, resulting from a decrease in cellular uptake. Determination of extra- and intracellular ZnO nanoparticles levels and the extent of their solubilization has enabled an approximate materials flow analysis for the added ZnO nanoparticles. No significant differences for the intracellular dissolution of modified ZnO nanoparticles were observed, suggesting that the cellular uptake of ZnO nanoparticles, possibly influenced by protein corona, is a much more determinant for ZnO cytotoxicity.

Recently, several studies about new materials, alternative to inorganic UV filters based on TiO_2 and ZnO, have been published. For example, Yabe *et al.*[60] proposed for the first time ultrafine particles of doped ceria *via* soft solution chemical routes at 40°C as possible new suitable system. In a previous study,[61] they showed that the photocatalytic properties of ceria could be successfully reduced by coating the particles with an amorphous silica layer. However, a worsening of the UV-shielding effect was also noticed. On the contrary, by doping CeO_2 with a metal ion (Mn^{+}=Mg^{2+}, Ca^{2+}, Sr^{2+}, Ba^{2+}, Y^{3+}, La^{3+}, Nd^{3+}, Sm^{3+}, Eu^{3+}, Tb^{3+}) with lower valence and/or larger ionic size than the size of Ce^{4+}, they kept unchanged the UV properties with a significant reduction of the photocatalytic activity.

Lima and co-workers[62] proposed a combination of TiO_2/CeO_2 or ZnO/CeO_2 nanoparticles to enhance the refractory properties. The ultrafine systems were prepared by a non-alkoxide sol-gel method, by the use of cerium nitrate and zinc acetate precursors and lactic acid as stabilizer. The results showed a low photocatalytic activity and an UV absorption up to 350 nm.

1.5 Mesoporous Silica Nanoparticles

All the system developed, during the research activity, are formed by mesoporous silica nanoparticles (MSN), chosen as the host matrix, loaded with nanosized inorganic UV filters.[9] Silica is an ingredient widely used in cosmetic products. It is added into the formulation as thickener or texturizing agent. It was used also in a novel cosmetic powder composition to give superior smoothness and adhesion to the skin.[63]

In 1968, Stöber and co-workers developed an effective method for the synthesis of monodispersed silica particles, which involves the hydrolysis and the consequently condensation of tetraalkyl silicates in a mixture of alcohol, water and ammonia as catalyst.[64] A good control over the growth and, then, over the size of the silica particles can be achieved by this method. The first attempt to synthesize a mesoporous silica material was conducted in 1971, with the synthesis of a low-bulk density silica obtained from the hydrolyzation and the condensation of tetraethoxysilane (TEOS) in the presence of a cationic surfactant.[65] Only in 1992 scientists in oil giant Mobil Corporation laboratories prepared a series of ordered mesoporous materials, labeled as MCM-41 (2D-hexagonal mesopore arrangement), MCM-48 (3D-cubic) and MCM-50 (lamellar), with pore size between 1.5 nm and 10 nm via a liquid-crystal templating (LCT) mechanism under basic aqueous solution (Figure 10).[66] In 1997 Grun and co-workers modified the Stöber method by the addition of a cationic surfactant to the reaction mixture and the result was the obtaining of submicrometer-scaled and spherical MCM-41 particles.[67] In 2001, Cai *et al.* first synthesized nano-sized mesoporous silicas,[68] and then Lin and co-authors popularized the term “MSN” to indicate mesoporous silica nanoparticles.[69]

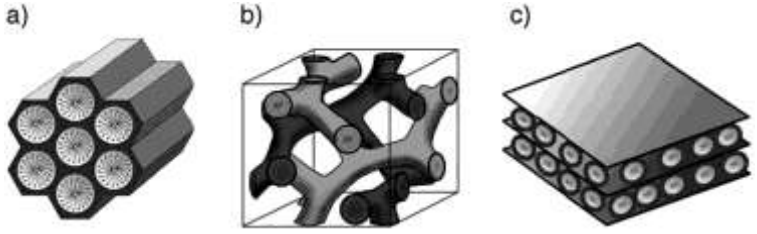

Figure 10 Different structures of MCM-41(a), MCM-48 (b) and MCM-50 (c).

The synthesis of MSN with control over their morphology, particle size distribution, pore diameter, uniformity and dispersion is of great importance in the field of materials science, for

[9] According to IUPAC definition, a mesoporous materials can have pores size between 2 and 50 nm.

their use in catalyst, adsorption, polymer filler, optical devices, bio-imaging, drug-delivery and biomedical application.[70] The numerous patents and literature publications demonstrate the importance of MSN in such applications.

Recently, MSN has shown promise as an inorganic matrix also in cosmetic field because it is suitable to host, inside the pores, several substance such as organic molecules of different sizes, which can interact with the internal silanol groups freely accessible.[14d, 71] For example, Ambrogi *et al.*[14e] used the MCM-41 properties to adsorb and to influence the photostability and the release of three organic UV filters: namely benzophenone-3, benzophenone-2 and p-aminobenzoic acid. MCM-41 microcrystals have been loaded with the UV absorbents obtaining a good loading w/w percentage. Photochemical studies demonstrated that the UV-shielding properties of benzophenone-2 were preserved whereas in the other two cases a small reduction of sunscreen protection range occurred. Benzophenone-3 and benzophenone-2 *in vitro* release from loaded MCM-41 were investigated and compared to formulations containing free UV ray absorbent; no remarkable differences were observed in the release profiles.

As widely reported in literature, the templating method has been extensively applied to synthesize MSN with high surface areas, tunable pore size, large pore volumes and rich morphology. The control of the experimental conditions (*i.e.* temperature, pH, surfactant concentration and silica sources) allows to obtain MSN with several mesostructures (for example disordered, wormhole-like, hexagonal, cubic or lamellar), with various morphologies (for example spheres, hollow spheres, fibers, tubules, gyroids), and with different dimensions.[70]

Among the huge variety of strategies and methods for the preparation of MSN, we adopted the procedure described by Ma *et al.*[72], with slight modification. One of the main advantages of the MSN, used as matrix, concerns the possibility to obtain a good compromise between the efficiency of the UV shielding properties explicated by the inorganic nanosized UV filter and the possibility of reducing its photocatalytic properties.

The chemistry of the synthesis involves the use of a cationic surfactant, the cetyltrimethylammonium bromide (CTABr), as templating agent. CTABr is included into the silica network during the polycondensation reaction of nanoparticles and its further decomposition during the calcination produces the formation of mesopores. This synthesis can be considered as a co-operation between a classic sol-gel process (hydrolysis and condensation of TEOS) and a sort of autoassembly phenomenon of the silicate species with CTABr, as shown in Figure 11. If the critical micellar concentration (CMC) inside the starting reaction mixture is achieved, the surfactant molecules in the polar solution tend to organize into direct micelles. In this way, the hydrophobic tails are oriented towards the inner part while the hydrophilic heads remain outwards and face the interphase. Hence, these direct micelles have a positive surface charge,

due to the hydrophilic heads and therefore the anionic silicate species are attracted and tend to concentrate all around them. In order to expand the pore size of MSN, n-hexane as swelling agent is added to the reaction gel: its solubilization inside the hydrophobic regions of micelles leads to an increase in micellar diameter, and then in the pore size. With the hydrolysis and condensation reactions of silicon alcoxide and the growth of silica nuclei, the micelles are "trapped" inside the silica matrix and during the subsequent thermal treatment the organic fraction is burned away, leaving room to the mesoporous structure of silica nanoparticles, which are thus suitable for being impregnated and to host the inorganic UV filter.

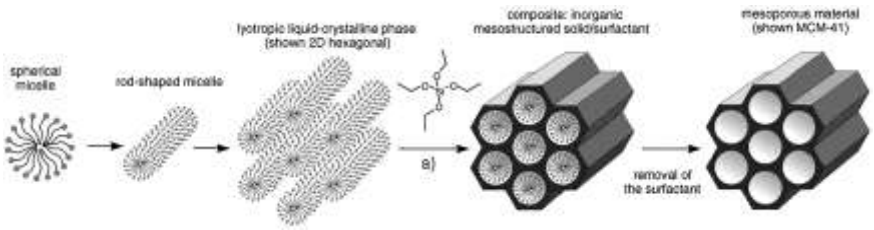

Figure 11 Schematic illustration of the synthesis process of MCM-41.

References

[1] J. Orazio, S. Jarrett, A. Amaro-Ortiz, T. Scott, *International Journal of Molecular Sciences* **2013**, *14*, 12222.

[2] aE. Proksch, J. M. Brandner, J.-M. Jensen, *Experimental Dermatology* **2008**, *17*, 1063-1072; bP. M. Elias, *Current allergy and asthma reports* **2008**, *8*, 299-305.

[3] E. Fuchs, *The Journal of Cell Biology* **1990**, *111*, 2807-2814.

[4] J. A. McGrath, R. A. J. Eady, F. M. Pope, in *Rook's Textbook of Dermatology*, Blackwell Publishing, Inc., **2008**, pp. 45-128.

[5] aM. Cichorek, M. Wachulska, A. Stasiewicz, A. Tymińska, *Advances in Dermatology and Allergology/Postępy Dermatologii I Alergologii* **2013**, *30*, 30-41; bG.-E. Costin, V. J. Hearing, *The FASEB Journal* **2007**, *21*, 976-994.

[6] S. Sachdeva, R. Sachdeva, S. Nanda, *Indian Journal of Dermatology, Venereology, and Leprology* **2009**, *75*, 93-96.

[7] D. E. Godar, *Photochemistry and Photobiology* **2005**, *81*, 736-749.

[8] T. L. Diepgen, M. Fartasch, H. Drexler, J. Schmitt, *British Journal of Dermatology* **2012**, *167*, 76-84.

[9] aU. Osterwalder, M. Sohn, B. Herzog, *Photodermatology, Photoimmunology & Photomedicine* **2014**, *30*, 62-80; bS. Schalka, V. M. S. d. Reis, *Anais Brasileiros de Dermatologia* **2011**, *86*, 507-515; cU. Osterwalder, B. Herzog, *British Journal of Dermatology* **2009**, *161*, 13-24.

[10] N. Serpone, D. Dondi, A. Albini, *Inorganica Chimica Acta* **2007**, *360*, 794-802.

[11] P. R. Tanner, *Dermatologic Clinics* **2006**, *24*, 53-62.

[12] U. Osterwalder, B. Herzog, *Photochemical & Photobiological Sciences* **2010**, *9*, 470-481.

[13] L. R. Gaspar, J. Tharmann, P. M. B. G. Maia Campos, M. Liebsch, *Toxicology in Vitro* **2013**, *27*, 418-425.

[14] aL. Perioli, V. Ambrogi, C. Rossi, L. Latterini, M. Nocchetti, U. Costantino, *Journal of Physics and Chemistry of Solids* **2006**, *67*, 1079-1083; bS. Galindo-Rodriguez, E. Allémann, H. Fessi, E. Doelker, *Pharmaceutical Research*, *21*, 1428-1439; cS. A. Wissing, R. H. Müller, *Journal of Controlled Release* **2002**, *81*, 225-233; dY. W. Chen-Yang, Y. T. Chen, C. C. Li, H. C. Yu, Y. C. Chuang, J. H. Su, Y. T. Lin, *Materials Letters* **2011**, *65*, 1060-1062; eV. Ambrogi, L. Perioli, F. Marmottini, L. Latterini, C. Rossi, U. Costantino, *Journal of Physics and Chemistry of Solids* **2007**, *68*, 1173-1177; fL. Shi, J. Shan, Y. Ju, P. Aikens, R. K. Prud'homme, *Colloids and Surfaces A: Physicochemical and Engineering Aspects* **2012**, *396*, 122-129.

[15] A. J. Waters, D. R. Sandhu, G. Lowe, J. Ferguson, *Contact Dermatitis* **2009**, *60*, 172-173.

[16] I. Karlsson, L. Hillerström, A.-L. Stenfeldt, J. Mårtensson, A. Börje, *Chemical Research in Toxicology* **2009**, *22*, 1881-1892.

[17] T. S. Balogh, M. V. r. R. Velasco, C. A. Pedriali, T. M. Kaneko, A. R. Baby, *Anais Brasileiros de Dermatologia* **2011**, *86*, 732-742.

[18] S. Seité, A. Fourtanier, D. Moyal, A. R. Young, *British Journal of Dermatology* **2010**, *163*, 903-914.

[19] H. Bendovà, J. Akrman, A. Krejčí, L. Kubáč, D. Jírová, K. Kejlová , H. Kolářová , M. Brabec, M. Malý, *Toxicology in Vitro* **2007**, *21*, 1268-1275.

[20] A. Springsteen, R. Yurek, M. Frazier, K. F. Carr, *Analytica Chimica Acta* **1999**, *380*, 155-164.

[21] B. L. Diffey, J. Robson, *Journal of Cosmetic Science* **1989**, *40*, 127-133.

[22] B. L. Diffey, *International Journal of Cosmetic Science* **1994**, *16*, 47-52.

[23] *The Boots Co PLC, Nottingham, England* **1991**.

[24] aR. W. Gange, A. Soparkar, E. Matzinger, S. H. Dromgoole, J. Sefton, R. DeGryse, *Journal of the American Academy of Dermatology* **1986**, *15*, 494-499; bC. Cole, *Photodermatology, Photoimmunology & Photomedicine* **2001**, *17*, 2-10.

[25] aJ. W. Stanfield, P. A. Feldt, E. S. Csortan, L. Krochmal, *Journal of the American Academy of Dermatology* **1989**, *20*, 744-748; bC. Cole, R. VanFossen, *Journal of the American Academy of Dermatology* **1992**, *26*, 178-184.

[26] K. H. Kaidbey, A. Barnes, *Journal of the American Academy of Dermatology* **1991**, *25*, 262-266.

[27] A. Chardon, D. Moyal, C. Hourseau, *Lowe N, Shaath N, Pathak M, eds. Sunscreens: development, evaluation and regulatory aspects. New York: Marcel Dekker* **1997**, 559-582.

[28] R. Gillies, N. Kollias, *Lowe N, Shaath N, Pathak M, eds. Sunscreens: development, evaluation and regulatory aspects. New York: Marcel Dekker* **1997**, 601-608.

[29] A. Fourtanier, D. Moyal, S. Seite, *Photochemical & Photobiological Sciences* **2012**, *11*, 81-89.

[30] E. B. Manaia, R. C. K. Kaminski, M. A. Corrêa, L. A. Chiavacci, *Brazilian Journal of Pharmaceutical Sciences* **2013**, *49*, 201-209.

[31] P. Falcaro, G. Zaccariello, V. Stoyanova, A. Benedetti, S. Costacurta, *Science of Advanced Materials* **2014**, *6*, 1330-1337.

[32] N. Serpone, A. Salinaro, A. V. Emeline, S. Horikoshi, H. Hidaka, J. Zhao, *Photochemical & Photobiological Sciences* **2002**, *1*, 970-981.

[33] aD. Dondi, A. Albini, N. Serpone, *Photochemical & Photobiological Sciences* **2006**, *5*, 835-843; bI. Fenoglio, J. Ponti, E. Alloa, M. Ghiazza, I. Corazzari, R. Capomaccio, D. Rembges, S.

Oliaro-Bosso, F. Rossi, *Nanoscale* **2013**, *5*, 6567-6576; cA. Jaeger, D. G. Weiss, L. Jonas, R. Kriehuber, *Toxicology* **2012**, *296*, 27-36.

[34] aF. Rancan, B. Nazemi, S. Rautenberg, M. Ryll, S. Hadam, Q. Gao, S. Hackbarth, S. F. Haag, C. Graf, E. Rühl, U. Blume-Peytavi, J. Lademann, A. Vogt, M. C. Meinke, *Skin Research and Technology* **2014**, *20*, 182-193; bI. Corazzari, S. Livraghi, S. Ferrero, E. Giamello, B. Fubini, I. Fenoglio, *Journal of Materials Chemistry* **2012**, *22*, 19105-19112; cT. Ukmar, A. Godec, U. Maver, O. Planinsek, M. Bele, J. Jamnik, M. Gaberscek, *Journal of Materials Chemistry* **2009**, *19*, 8176-8183; dG. J. Clydesdale, G. W. Dandie, H. K. Muller, *Immunol Cell Biol* **2001**, *79*, 547-568.

[35] O. Carp, C. L. Huisman, A. Reller, *Progress in Solid State Chemistry* **2004**, *32*, 33-177.

[36] C. M. Sayes, R. Wahi, P. A. Kurian, Y. Liu, J. L. West, K. D. Ausman, D. B. Warheit, V. L. Colvin, *Toxicological Sciences* **2006**, *92*, 174-185.

[37] B. Kiss, T. Bíró, G. Czifra, B. I. Tóth, Z. Kertész, Z. Szikszai, Á. Z. Kiss, I. Juhász, C. C. Zouboulis, J. Hunyadi, *Experimental Dermatology* **2008**, *17*, 659-667.

[38] J. Jacobs, I. van de Poel, P. Osseweijer, *Nanoethics* **2010**, *4*, 103-113.

[39] O. N. Mileyeva-Biebesheimer, A. Zaky, C. L. Gruden, *Environmental Engineering Science* **2010**, *27*, 329-335.

[40] F. A. Cotton, G. Wilkinson, *Advanced Inorganic Chemistry* **1972**, *third edition*, 810-813.

[41] E. s. B. Manaia, R. C. K. Kaminski, M. A. Correa, L. A. Chiavacci, *Brazilian Journal of Pharmaceutical Sciences* **2013**, *49*, 201-209.

[42] aR. Daghrir, P. Drogui, D. Robert, *Industrial & Engineering Chemistry Research* **2013**, *52*, 3581-3599; bC. W. Lai, J. C. Juan, W. B. Ko, S. Bee Abd Hamid, *International Journal of Photoenergy* **2014**, *2014*, 14; cM. Pelaez, N. T. Nolan, S. C. Pillai, M. K. Seery, P. Falaras, A. G. Kontos, P. S. M. Dunlop, J. W. J. Hamilton, J. A. Byrne, K. O'Shea, M. H. Entezari, D. D. Dionysiou, *Applied Catalysis B: Environmental* **2012**, *125*, 331-349.

[43] D. H. Hanaor, C. Sorrell, *J Mater Sci* **2011**, *46*, 855-874.

[44] A. Ricci, M. N. Chretien, L. Maretti, J. C. Scaiano, *Photochemical & Photobiological Sciences* **2003**, *2*, 487-492.

[45] Y. Ji, L. Zhou, C. Ferronato, A. Salvador, X. Yang, J.-M. Chovelon, *Applied Catalysis B: Environmental* **2013**, *140,Äì141*, 457-467.

[46] D. T. Tran, R. Salmon, *Australasian Journal of Dermatology* **2011**, *52*, 1-6.

[47] G. Mie, *Annalen der Physik* **1908**, *25*, 377-445.

[48] T. A. Egerton, I. R. Tooley, *International Journal of Cosmetic Science* **2012**, *34*, 117-122.

[49] N. S. Allen, M. Edge, A. Ortega, C. M. Liauw, J. Stratton, R. B. McIntyre, *Polymer Degradation and Stability* **2002**, *78*, 467-478.

[50] A. P. Popov, *Moscow University Physics Bulletin* **2009**, *64*, 513-518.

[51] aA. P. Popov, *Journal of Biomedical Nanotechnology* **2010**, *6*, 432-451; bY. Li, T. J. White, *Journal of Solid State Chemistry* **2004**, *177*, 1372-1381; cK. Madhusudan Reddy, C. V. Gopal Reddy, S. V. Manorama, *Journal of Solid State Chemistry* **2001**, *158*, 180-186.

[52] D. Pan, N. Zhao, Q. Wang, S. Jiang, X. Ji, L. An, *Advanced Materials* **2005**, *17*, 1991-1995.

[53] L. Zhao, J. Yu, *Journal of Colloid and Interface Science* **2006**, *304*, 84-91.

[54] I. Hernàndez Perez, A. M. Maubert, *International Journal of Electrochemical Science* **2012**, *7*, 8832-8847.

[55] C.-L. Kuo, C.-L. Wang, H.-H. Ko, W.-S. Hwang, K.-m. Chang, W.-L. Li, H.-H. Huang, Y.-H. Chang, M.-C. Wang, *Ceramics International* **2010**, *36*, 693-698.

[56] E. C. Siegfried, P. Y. Shah, *J Perinatol* **1999**, *19*, 31-39.

[57] aG. P. Dransfield, *Radiation Protection Dosimetry* **2000**, *91*, 271-273; bH.-H. Ko, H.-T. Chen, F.-L. Yen, W.-C. Lu, C.-W. Kuo, M.-C. Wang, *International Journal of Molecular Sciences* **2012**, *13*, 1658-1669.

[58] G. Bandekar, N. S. Rajurkar, I. S. Mulla, U. P. Mulik, D. P. Amalnerkar, P. V. Adhyapak, *Applied Nanoscience* **2013**, *4*, 199-208.

[59] M. Luo, C. Shen, B. N. Feltis, L. L. Martin, A. E. Hughes, P. F. A. Wright, T. W. Turney, *Nanoscale* **2014**, *6*, 5791-5798.

[60] S. Yabe, T. Sato, *Journal of Solid State Chemistry* **2003**, *171*, 7-11.

[61] K. Hirai, S. Momose, S. N. I. C. Shinnumadate, S. Yabe, S. N. I. C. Yoshida, Google Patents, **1998**.

[62] aJ. F. d. Lima, R. F. Martins, C. R. Neri, O. A. Serra, *Applied Surface Science* **2009**, *255*, 9006-9009; bL. Truffault, M.-T. Ta, T. Devers, K. Konstantinov, V. Harel, C. Simmonard, C. Andreazza, I. P. Nevirkovets, A. Pineau, O. Veron, J.-P. Blondeau, *Materials Research Bulletin* **2010**, *45*, 527-535; cF. Caputo, M. De Nicola, A. Sienkiewicz, A. Giovanetti, I. Bejarano, S. Licoccia, E. Traversa, L. Ghibelli, *Nanoscale* **2015**, *7*, 15643-15656.

[63] R. A. Macchio, I. Brown, M. Tietjen, Google Patents, **1989**.

[64] W. Stober, A. Fink, E. Bohn, *Journal of Colloid and Interface Science* **1968**, *26*, 62-69.

[65] V. Chiola, J. E. Ritsko, C. D. Vanderpool, *US Patent 3,556,725 (Sylvania Electric Products Inc.)* **1971**.

[66] C. T. Kresge, M. E. Leonowicz, W. J. Roth, J. C. Vartuli, J. S. Beck, *Nature* **1992**, *359*, 710.

[67] M. Grun, I. Lauer, K. K. Unger, *Advanced Materials* **1997**, *9*, 254-256.

[68] Q. Cai, Z. S. Luo, W. Q. Pang, Y. W. Fan, X. H. Chen, F. Z. Cui, *Chemistry of Materials* **2001**, *13*, 258-263.

[69] C. Y. Lai, B. G. Trewyn, D. M. Jeftinija, K. Jeftinija, S. Xu, S. Jeftinija, V. S. Y. Lin, *Journal of American Chemical Society* **2003**, *125*, 4451-4459.

[70] S.-H. Wu, C.-Y. Mou, H.-P. Lin, *Chemical Society Reviews* **2013**, *42*, 3862-3875.

[71] C. C. Li, Y. T. Chen, Y. T. Lin, S. F. Sie, Y. W. Chen-Yang, *Colloids and Surfaces B: Biointerfaces* **2014**, *115*, 191-196.

[72] S. Ma, Y. Wang, Y. Zhu, *Journal of Porous Materials* **2010**, *18*, 233-239.

2 MATERIALS AND METHODS

2.1 Materials used for the synthetic procedures

3,7-bis (dimethylamino) phenazathionium chloride (Methylene Blue, MB, Sigma-Aldrich)

4-[4-(dimethylamino)phenylazo]benzenesulfonic acid, sodium salt) (Methyl orange, MO, Sigma-Aldrich)

Ammonia (NH_3, Sigma-Aldrich, 30%)

Bismuth(III) nitrate pentahydrate (($Bi(NO_3)_3 \cdot 5H_2O$), Sigma-Aldrich, 99.9%)

Cetyltrimethylammonium bromide (CTABr, Sigma-Aldrich)

Distilled water

Ethanol (EtOH, Sigma-Aldrich, 99.8%)

Methanol (MeOH, Sigma-Aldrich, 99.6%)

N-(4-idrossifenil) acetammide ($C_8H_9NO_2$, Paracetamol, Sigma-Aldrich)

N-hexane (Sigma-Aldrich, 99.6%)

Nitric acid (HNO_3, 65%)

Sodium hydroxide (NaOH, Sigma-Aldrich)

Tetraethoxysilane (TEOS, Sigma-Aldrich, 98%)

Titanium(IV) isopropoxide (TTIP, Sigma-Aldrich, 97%)

2.2. Chemical-physical characterization methods

Structural characterization

The nitrogen adsorption-desorption isotherms were obtained at the liquid nitrogen temperature (77 K) using a Micromeritics ASAP 2010 volumetric adsorption analyzer. From the

adsorption data, the Brunauer-Emmett-Teller (BET) equation was used to calculate the specific surface area, while from the adsorption branches of the isotherms, the Barrett-Joyner-Halenda (BJH) model was used to estimate the pore size distribution.

X-ray powder diffraction (XRPD) spectra were recorded with a Philips X'Pert powder diffractometer (Bragg-Brentano parafocusing geometry) with a voltage of 40kV. A nickel-filtered CuKα1 radiation (λ = 0.15406 nm) and a step-by-step technique (step of 0.05° 2 h) with collection times of 10s/step were employed. From the XRPD patterns, the quantitative analysis and size distribution of the samples were carried out by means the Rietveld refinement.[1]

Morphological and dimensional information were probed through a Zeiss ∑igma Field Emission-Scanning Electron Microscopy (FE-SEM), equipped with the Gemini column with a resolution of 1.5 nm and provided with several detectors: in-lens detector for high resolution with secondary electrons (SE), annular segment detector (AsB) for analysis with backscattered electrons (compositional contrast), variable pressure secondary electron (VPSE) detector for morphology at variable pressure, Bruker-Quantax energy dispersive X-ray spectroscopy (EDS) detector with resolution of 127 eV at Mn Kα and active area of 30 mm^2 for microanalysis. For the morphological observations, the powdered sample was suspended in isopropyl alcohol and the mixture was sonicated, finally 5 µL of this suspension were deposited on a silicium substrate. For EDS analysis, the specimens were prepared depositing the powdered sample on a conductive tape.

Size and morphology of the nanoparticles were also probed through a JEOL JEM 3010 transmission electron microscope (TEM) operating at 300 kV. The copper grids were allowed to dry in air. The energy dispersive X-ray spectroscopy (EDX) measurements were carried out with a Oxford Instruments Isis System Series 300. The powder specimens were suspended in isopropyl alcohol and an aliquote of 5 µL was taken and then deposited on a copper grid (300 mesh) coated with holey carbon film. The copper grids were allowed to dry in air.

Optical characterization

The diffusive reflective UV-vis (DRUV-vis) measurements were collected with a JASCO V-570 UV-vis spectrophotometer equipped with an integrating sphere accessory. Barium sulfate was used as reference. The powder samples were placed between two quartz slides and the spectra were recorded in 200-800 nm wavelength range. To estimate the band gap energy, plots of $(K\text{-}M \cdot h\nu)^{1/2}$ versus photon energy (hv) are reported: the band gap energy was

evaluated by extrapolating the straight line, tangent to $(K\text{-}M\cdot h\nu)^{1/2}$, to the axis intercept. The measurements were conducted in collaboration with Prof.R.Amadelli at University of Ferrara.

Chemical-physical characterization

X-ray photoelectron spectroscopy (XPS) was conducted on *x*TiO_2@MSN systems described in Chapter 3 using a Physical Electronics PHI 5700 spectrometer with non monochromatic Mg Kα radiation (300 W, 15 kV, 1253.6 eV) for the analysis of the core level signals of C 1s, O 1s, Ti 2p and Si 2p and with a multi-channel detector. The spectrometer was calibrated using the signal Au $4f_{7/2}$ = 83.9 eV. Binding energy values were referenced to the C 1s peak (284.8 eV) from the adventitious contamination layer. The PHI ACCESS ESCA-V6.0 F software package and *Multipak v8.2b* were used for acquisition and data analysis, respectively. A Shirley-type background was subtracted from the signals. Recorded spectra were always fitted using Gauss–Lorentz curves, in order to determine the binding energy of the different element core levels more accurately. The error in BE (binding energy) was estimated to be ca. 0.1 eV. The measurements were conducted in collaboration with Prof. E. Rodríguez-Castellón at Universidad de Málaga.

X-ray photoelectron spectroscopy (XPS) surface analyses were performed on *x*Bi/Ti@MSN_*y* as reported in Chapter 5 using a Perkin-Elmer Φ 5600ci spectrometer with non-monochromatic Al Kα radiation (1486.6 eV) in the 10^{-7} Pa pressure range. All the binding energy (BE) values are referred to the Fermi level. The correct calibration of the BE scale was verified during the analysis by checking the position of both Au$4f_{7/2}$ and Cu$2p_{3/2}$ bands (from pure metal targets), falling at 84.0 eV and 932.6 eV, respectively.[2] After a Shirley-type background subtraction, the raw spectra were fitted using a non-linear least-square fitting program adopting Gaussian-Lorentzian peak shapes for all the peaks. Owing to surface charging, samples presented a shift of the bands towards higher BE's: the charging effect was corrected by using an internal reference, namely after identification of SiO_2 presence by means of the silicon "alpha parameter" (binding energy of Si2p band + kinetic energy of SiKLL band). In all samples, the Si alpha parameter lay in between 1712.0-1712.3 eV, confirming the presence of silicon dioxide.[2-3] The surface charging, of about 4-5 eV, was then corrected by considering the Si2p centered at 103.3 eV: as a consequence, the O1s band related to SiO_2 fell around 532.7 eV, in agreement with the presence of stoichiometric silica.[2] The uncertainty of all the determined BE's was lower than 0.2 eV. The atomic composition was evaluated using sensitivity factors as provided by Θ V5.4A software. The uncertainties of the calculated atomic

fraction of the different elements are lower than 5-10%. The reported atomic fraction data were calculated excluding “adventitious” carbon (originated by environment contamination). The measurements were conducted in collaboration with Prof. E.Cataruzza and Prof. A.Glisenti at Università di Padova.

Analytic characterization

Titanium and silicium concentrations were determined by nuclear activation analysis (NAA) in collaboration with Prof. E. Sabbioni, S. Manenti and F.Groppi at LASA (Laboratorio Acceleratori e Superconduttività Applicata, University of Milan), INFN (Istituto Nazionale di Fisica Nucleare, Milano), and LENA (Laboratory of Applied Nuclear Energy, University of Pavia). The radioactivity produced at the end of the neutron irradiation of a stable isotope of a sample measured at the time t_d after the end of irradiation ,is expressed by the activation equation:

(1)

$$A = \emptyset\sigma \frac{N\, W_x \Theta}{M} (1 - e^{-\lambda t_{irr}}) e^{t_d}$$

where:

A= radioactivity of the nuclide

$\emptyset$= neutron flux

σ= cross section

W_x= weight of the element to be determined with atomic weight M

Θ = isotopic abundance of the stable nuclide concerned the reaction)

N = Avogadro constant ($6{,}022 \times 10^{23}$)

λ= decay constant

t_{irr}= irradiation time

t_d = decay time

From (1) it is possible to calculate the weight of the element W_x present in the sample. The equation (1) indicates also that in principle, NAA is an absolute method of analysis, the concentration of the element in the sample W_x being determined directly from the measured radioactivity A, and the knowledge of the nuclear constants and the experimental conditions.

However, σ is not known with sufficient accuracy and $\emptyset$ cannot be determined accurately. Consequently, in practice a comparative method is commonly used. In this method a known amount of the element to be determined (compartor, Wc) is irradiated, processed and counted exactly in the same way as the sample being analyzed and the radioactivity measured under the same conditions at the same time. Thus, the concentration of a certain element W_x in a sample can be simply calculated in accordance with the following equation:

$$\frac{W_{x\ sample}}{W_{c\ comparator}} = \frac{A_{s\ sample}}{A_{c\ comparator}}$$

where:

W_x= concentration of the element in the sample;

A_s= radioactivity induced by neutron activation of the element to be determined in the sample;

A_c= radioactivity induced by neutron activation of the element to be determined in the sample;

W_c= radioactivity induced by neutron activation of the element to be determined in the comparator.

The analysis were of non destructive type (Instrumental NAA, INAA) which involved: (i) the preparation of the samples and standards; (ii) the neutron irradiation in the nuclear reactor; (iii) the direct radioactive counting of the induced ^{51}Ti and ^{31}Si by gamma ray spectrometry. 10-15 mg of each solid sample or standard were weighted in appropriate cylindrical-shaped plastic sample vials made from lab-grade low density polyethylene (Kartell, Italia). The attached caps of the vials were sealed by heat before neutron irradiation. The vials were introduced in a polythene container to be send in the core of the nuclear reactor for the neutron bombardment.

Titanium is composed by five natural stable isotope, while silicon by three stable isotopes with different isotopic abundance. For our analysis, taking into account the experimental conditions available we selected the following nuclear reactions:

$$^{50}\text{Ti}\ (n, \gamma)^{51}\text{Ti} \quad \text{and} \quad ^{29}\text{Si}(n, p)^{29}\text{Al}$$

The induced ^{51}Ti, formed by neutron capture and gamma prompt emission, has an half life of 5.76 min. ^{29}Al, formed by neutron capture and proton emission, has an half life of 6.56 min. Both radioisotopes can be determined by the measurement of their emitted gamma rays. Neutron irradiations were carried out in the Triga Mark II reactor (LENA Laboratory, University of Pavia). In particular, due to the short half life of ^{51}Ti and ^{29}Al the irradiations of the plastic container were carried out in the special rabbit channel (fast pneumatic tube) directly connected with the radiochemical laboratory of the reactor for the recovery of the irradiated samples to be immediately submitted to gamma ray spectrometry. In this irradiation position the flux of neutrons to which samples were submitted was of $7x10^{12}$ neutrons cm^{-2} s^{-1}.[4] After 30 sec of irradiation the plastic container were re-extracted from the core of the reactor, immediately opened and the irradiated vials containing the radioactivated samples were counted by gamma ray spectrometry.

The irradiated samples were counted by computer-based high resolution gamma ray spectrometry using a Ge detector (EG&G – ORTEC (USA) previously calibrated with a certified Eu-152 (half-life 13.52 y) radioactive source. The software used for the acquisition and processing of data and analysis was GammaVision for Windows Model A66-B32, Version 6.07 (EG&G-ORTEC). In order to avoid corrections due to the fast decay time of ^{51}Ti and to decay interfering radioisotopes with half-lives of seconds which could cause an high radioactive background during the measurements the countings of samples and standards started exactly 3 min after the end of irradiation. In addition, all countings were carried out in the same counting geometry. ^{51}Ti radioactivity was measured using the characteristic line photon emission of 320.1 KeV while the detection of ^{29}Al was carried out using the photopeak at 1273 KeV, as reported in Figure 1.

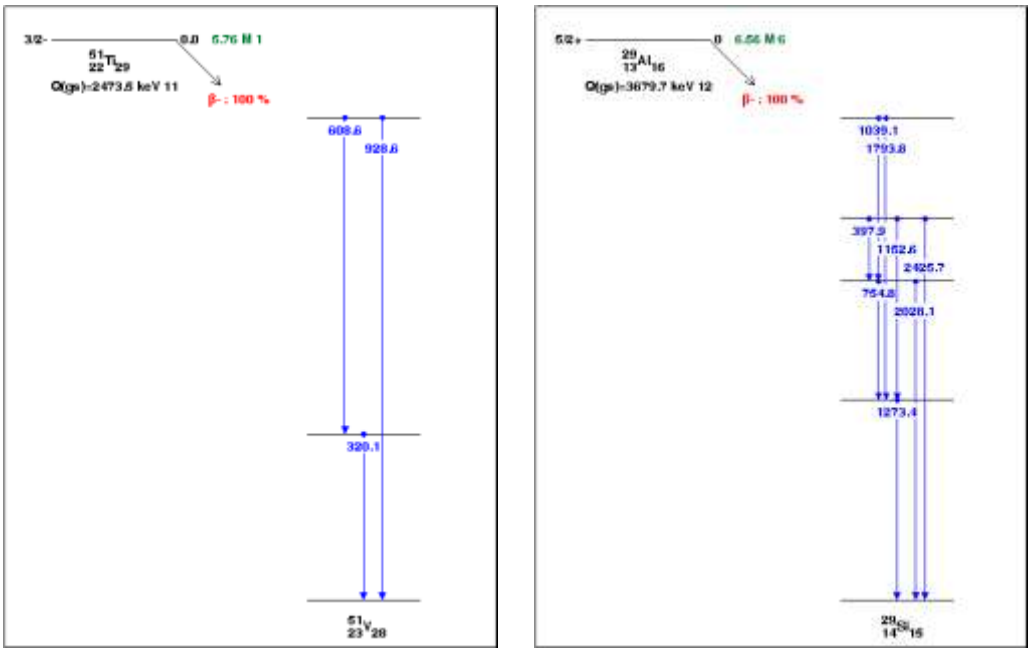

Figure 1 Characteristic line photon emission of ^{51}Ti and ^{29}Al.

Figure 2 shows a good linearity between the induced ^{51}Ti radioactivity as function of the titanium concentration. Although in this work titanium was determined at level of percent, the absolute sensitivity of the here developed NAA is excellent, being of the order of 20 ng of Ti.

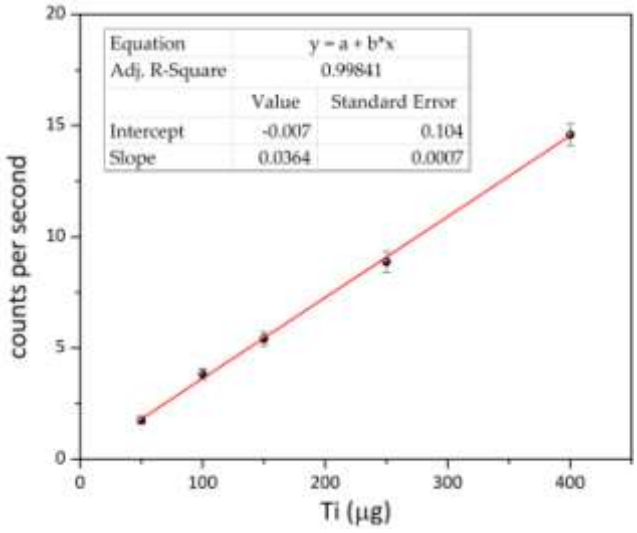

Figure 2 ^{51}Ti radioactivity as function of the titanium concentration.

Titanium and bismuth concentrations were determined by sector field inductively coupled plasma mass spectroscopy (SF-ICP-MS, ThermoFischer, Bremen, Germany) technique. The

instrument was equipped with sampler and skimmer cones in Ni, a Meinhard nebulizer, a water cooled spray chamber (Scott-type) and a guard electrode device. For ^{209}Bi quantification, the low resolution mode (LR = m/Δm 300) was used as the Bi potential oxides interferences, such as IrO and OsO, were resulting negligible, due to the lack of Ir and Os in the samples under study. To detect ^{47}Ti, the high resolution mode (HR = m/Δm 10.000) was applied; other masses as ^{46}Ti, ^{48}Ti ^{49}Ti and ^{50}Ti were heavily interfered by isobaric interferences (*i.e*. ^{46}Ca on ^{46}Ti, ^{48}Ca on ^{48}Ti, ^{50}Cr and 50V on 50Ti), while ^{49}Ti was less abundant (5.5%) than ^{47}Ti (7.3%). Using the HR for ^{47}Ti determination, the signal was separated from interferences such as ^{31}P^{16}O, ^{11}B^{36}Ar and ^{7}Li^{40}Ar. The internal standardization by ^{103}Rh at a concentration of 1 ng/mL in the analytical solutions and the matrix-matched calibration approach provided effective way to minimize the instrumental drifts and matrix effects. The method limits of detection (LoDs) and quantification (LoQs) were calculated by replicated measurements of a pool of samples. Because of lack of an appropriate matrix-matched CRM, a lyophilized human urine CRM sample (Seronorm Level 2, Sero AS, Billingstast, Norway) was used for trueness study. Moreover, as Ti was not certified in the CRM, recovery test was performed at the fortification level of 20 µg/g (*i.e.* 20 ng/mL in the analytical solutions) by spiking the matrix before digestion procedure. Precision in terms of repeatability was calculated by replicated measurements on the CRM for Bi and on the spiked sample for Ti. For the analysis, a mixture of 2 mL of ultrapure HNO3 Normatom®, 0.25 mL of suprapure HF and 1 mL of suprapure H_2O_2 was added to aliquotes of samples (10-20 mg). The samples were digested at 80±3°C on a hotplate (ModBlock CPI International, California, USA) for 3 hours and then transferred into clean polypropylene plastic tubes and filled up to a final volume of 50 mL with high-purity deionized water (Barnstead EASY-Pure II, Dubuque, IA, USA), and adequately diluited before the instrumental determination.

Photocatalytic Tests

The photocatalytic activity of the synthesized materials was determined by the degradation of two representative dyes (methylene blue and methyl orange) and of paracetamol under UV-vis irradiation. Experiments were performed at 293 K using a 100 mL Pyrex photochemical reactor with a 125 W medium pressure mercury lamp (Model UV13F,Helios Italquartz, Italy). The initial concentration of the target molecule was 6.0 x 10^{-5} M for MB, 7.5 x 10^{-5} for MO and 1.3 x 10^{-4} M for paracetamol and the amount of the photocatalyst was fixed at 1.25 g L^{-1}. The photon flux was measured by using a DeltaOHM radiometer HD2302.0 leaned against the external wall of the photoreactor containing only pure water. The irradiation power was 29

mW cm^{-2} in the UV-A range (310-400 nm) and 100 mW cm^{-2} in the visible/near IR range (400-1050nm). In order to reach the adsorption equilibrium prior the UV-irradiation, the sample was stirred in the dark for 30 min.[5] After switching on the UV-vis lamp, at each time step, an aliquot of 2 mL of the aqueous suspension was recovered from the reactor and filtered through a 0.45 µm PTFE Millipore disc to remove the catalyst powder.

Dye degradation process was monitored by a Shimadzu UV-2450 UV/Vis spectrometer (for *x*TiO_2@MSN systems) and by an Agilent 8453 UV-vis spectrometer (for *x*Bi/Ti@MSN_*y* samples) following the absorbance at the maximum of the UV-vis spectrum of the target molecules (660 nm for MO; 465 nm for MO and 243 nm for paracetamol). The dyes concentration was estimated using a standard calibration curves. The normalized intensity of the absorption band at 465 nm was plotted as a function of time of irradiation. Since the degradation pathways for the selected dye are known with high reliability,[6] the eventual formation of by-products was checked monitoring the overall UV-vis spectrum of the solutions recovered at different times during the degradation experiments. The mineralization of the target molecules and the production of intermediate inorganic species have been checked by ionic chromatography, using a Metrohm 883 instrument equipped with a conductometric detector. The inorganic anions were analyzed using a Metrosep A Supp5 250/4.0 column using a $NaHCO_3$ 1 mM/Na_2CO_3 3.2 mM solution as mobile phase while the cations were analysed using a Metrosep C4 250/4.0 with HNO_3 4.0 mM as mobile phase. For *x*TiO_2@MSN systems (see Chapter 3), for each target molecule, the material that demonstrated the best photocatalytic performance has been chosen to assess the reusability of the present nanocomposites. After switching off the lamp at the end of the first degradation experiment, a certain amount of the target molecule and of the photocatalyst was added into the reactor of the photocatalyst in order to restore the initial concentrations. After equilibration in the dark for 30 min, the lamp was switched on and samples of the solution (2 mL) were collected during time for UV-vis analysis. Four cycles have been performed for each target molecule. The photocatalytic tests were conducted in collaboration with Prof. P.Fornasiero, Dr. T.Montini and Dr. V.Gombac at Università di Trieste.

2.2. *In vitro* tests on culture of Human PBMCs

Preliminary *in vitro* tests on culture of human peripheral blood mononuclear cells (PBMCs) were conducted in order to evaluate the metabolic activity and the allergenic responses of the

cells exposed to the synthesized UV filters. The analysis were performed in collaboration with Prof. Mario di Gioacchino and Dr. Claudia Petrarca at Università degli Studi "Gabriele D'Annunzio" (Chieti, Italy). The *in vitro* tests were conducted on MSN, 10TiO_2@MSN, TiO_2 and on *x*Bi/Ti@MSN_800 series. In order to understand the behavior of only the active phase, a commercial TiO_2 (Degussa, P25, Germany) was used as reference and tested.

Cells

Human peripheral blood mononuclear cells (PBMCs) were isolated by density gradient centrifugation of freshly withdrawn blood from a healthy donor (using Lymphoprep™ protocol and reagents, Stemcell technologies) and seeded in a 96-well plate at 200,000 cells per well in 200 µl complete culture medium (RPMI, 10% FCS), supplemented or not, after 16 hours, with the polyclonal activator Phytohaemoagglutinin (PHA, 5 mg/ml), exposed to 0, 25, 50, 100 µg/ml of the synthetized UV filters. Cells were exposed to the vehicle alone after particles removal by filtration trough 22 µm nylon mesh (Millipore). Cells were analysed as described below after 6, 24, 48 and 72 hours of incubation at 37°C, 5% CO_2.

Citotoxicity tests

The citotoxicity was evaluated with an indirect method by means of a colorimetric assay that detects the metabolic activity of the cells. Experiments were performed incubating the cells in medium conditioned with the samples at the concentrations listed above. The vitality of the MTT-based assay is a colorimetric test which exploits the enzymatic activity of the mitochondrial oxide-reductase of viable cells to transform the yellow tetrazolium compound MTT (3-(4, 5-dimethylthiazol-2)-2, 5 diphenyl tetrazolium bromide) in insoluble violet colored formazan salts. The greater the number of live cells, the greater the intensity of the developed color. Analysis were performed according to the manufacturer instructions. Briefly, 20 µl of MTT (Sigma, 5 mg/mL in PBS), was added to each well. The plates were incubated for 3 hours at 37°C, 5% CO_2, for reduction of MTT by metabolically active cells. The medium was then carefully removed and to allow the solubilization of formazan crystals, 200 µl DMSO were added to each well. The plates were placed on a shaker for 15 minutes until complete solubilization of crystals and, then, the optical density (OD) of each supernates (not containing particulate matter) was determined. The quantity of formazan product was measured by the amount of 540 nm absorbance, which is directly proportional to the number of living cells in culture.

Apoptosis evaluation

Apoptotic cells were detected and discriminated from viable cells by fluorochrome conjugated-Annexin V that can bind to phosphatildilserine residues exposed on the outer layer only on damaged cell membranes. Necrotic cells were identified as cells positively stained with the DNA-specific fluorescent dye propidium iodide. Lymphocytes (0.5x106) were washed with 1 ml of PBS and then resuspended in 70 µl binding buffer (10 mM Hepes, 140 mM NaCl, 2.5 mM $CaCl_2$, 0.1% BSA, pH 7.4) and stained with 5µl FITC-conjugated Annexin V (Valter Occhiena) and 0.5 µg/ml propidium iodide for 15 min, at room temperature, in the dark. As positive control, 1 mM H_2O_2 was added to unexposed cells and incubated for 3 h. Samples were analyzed immediately after staining by flow cytometry using the FASCanto cytofluorimeter and the acquired data (10,000 events within the viable cell gate, per sample) were analyzed with FacsDiva software. Annexin V-positive cells are considered early apoptotic, whereas Annexin V-PI double positive are considered as late apoptotic.

In order to confirm the different effect of 25 µg/ml TiO_2 and MSN on PHA-activated lymphocytes obtained by apoptosis after 48 h incubation, a staining of cell's nuclei was performed. The nuclear morphology in cells was examined using a confocal fluorescence microscope (Olympus IX71) by staining the cells with the fluorescent DNA-binding Hoechst dye. After incubation in media containing different concentrations of nanoparticles, the lymphocytes cultured were treated with 100 mg/ml of the fluorescent DNA-biding dye Hoechst and then observed.

Intracellular reactive oxygen species (ROS) measurement

The production of intracellular ROS was measured using the dye dichlorodihydrofluorescin diacetate (DCFH-DA). This compound is a non-fluorescent cell permeant substance. Once inside the cell, it is hydrolysed by endogenous esterases to dichlorofluorescin (DCFH, non-fluorescent) and cannot any longer pass out of the cell; then, DCFH can be oxidized to fluorescent dichlorofluorescin (DCF) by action of cellular reactive oxygen species (ROS). Briefly, 2×10^5 PBMCs per well were seeded in a 96-well cell culture plate and treated with or without nanoparticles. After 24 hours, cells were extensively washed with phosphate-buffered saline (PBS) and incubated with 10 µM DCFH-DA in PBS, for 30 minutes, at 37°C; as a positive control, 1 mM H_2O_2 was added to another duplicate of cultures. Finally, fluorescence of the oxidized form of DCFH-DA (DCF) was measured using a FacsCanto cytfluorimeter (excitation wavelength: 485 nm; emission wavelength: 530 nm). For each sample, 10,000 events within the viable cells gate were acquired. Each condition was tested in quadruplicate.

References

[1] P. Riello, P. Canton, G. Fagherazzi, *Journal of Applied Crystallography* **1998**, *31*, 78-82.

[2] A. V. Naumkin, A. Kraut-Vass, C. J. Powell, S. W. Gaarenstroom, *NIST X-ray Photoelectron Spectroscopy Database*, **2012**.

[3] E. Cattaruzza, R. Bertoncello, F. Trivillin, P. Mazzoldi, G. Battaglin, L. Mirenghi, P. Rotolo, *Journal of Materials Research* **1996**, *11*, 229-235.

[4] A. Borio di Tigliole, A. Cammi, D. Chiesa, M. Clemenza, S. Manera, M. Nastasi, L. Pattavina, R. Ponciroli, S. Pozzi, M. Prata, E. Previtali, A. Salvini, M. Sisti, *Progress in Nuclear Energy* **2014**, *70*, 249-255.

[5] H. Lachheb, E. Puzenat, A. Houas, M. Ksibi, E. Elaloui, C. Guillard, J.-M. Herrmann, *Applied Catalysis B: Environmental* **2002**, *39*, 75-90.

[6] aC. Baiocchi, M. C. Brussino, E. Pramauro, A. B. Prevot, L. Palmisano, G. Marcì, *International Journal of Mass Spectrometry* **2002**, *214*, 247-256; bA. Houas, H. Lachheb, M. Ksibi, E. Elaloui, C. Guillard, J.-M. Herrmann, *Applied Catalysis B: Environmental* **2001**, *31*, 145-157; cE. Moctezuma, E. Leyva, C. A. Aguilar, R. A. Luna, C. Montalvo, *Journal of Hazardous Materials* **2012**, *243*, 130-138; dL. Yang, L. E. Yu, M. B. Ray, *Environmental Science & Technology* **2009**, *43*, 460-465; eY. He, F. Grieser, M. Ashokkumar, *Ultrasonics Sonochemistry* **2011**, *18*, 974-980.

3 Titania-based nanosystems

3.1 Sample preparation

Synthesis of mesoporous silica nanoparticles (MSN)

Mesoporous silica nanoparticles were synthesized as described by Ma *et al*.[1] The swelling agent n-hexane (60 mL) was added to a clear solution of CTABr (0.8 g), NaOH 2M (3 mL) and H_2O (400 mL). The mixture was stirred for 15 min (400 rpm) and then stopped. When the separation between the polar and nonpolar phases occurred, TEOS (4 mL) was dropped slowly and the system was put under vigorous stirring for 5 h, during which the clear solution gradually turned into a white suspension. The molar ratio of the reagents of the synthesis was 1TEOS : 0.12CTABr : 1268H_2O : 0.32NaOH : 25.1n-hexane. The obtained suspension was filtered and the recovered solid product was washed several times with MeOH and dried at 60°C overnight. In order to remove the surfactant, the product was calcined at 550°C, 2°C min-1 for 5 h. The obtained sample is referred as MSN.

Synthesis of MSN loaded with TiO_2 nanoparticles (xTiO_2@MSN)

The *x*TiO_2@MSN series was prepared with different nominal weight fractions of TiO_2 by incipient wet impregnation of MSN. Taking into account the pore volume availability, four samples were prepared by varying the amount of TTIP precursor in the impregnating dispersions.

The samples are referred as *x*TiO_2@MSN, where *x* represents the nominal weight percentage (10, 20, 30 and 40%wt) of TiO_2 expected to form after the thermal treatment. For the growth of TiO_2 into the pores of MSN was adapted the procedure reported by Lihitkar *et al*. with slight modifications.[2] The titanium tetraisopropoxide was dissolved in EtOH (25 mL) and successively the dispersion was added to the calcined silica (0.2 g) under magnetic stirring for 24 h and under nitrogen flow. Then, the solvent was removed by means a rotary evaporator and the recovered solids were annealed at 550°C, 2 °C min^{-1} rate, for 5 h.

3.2 Results and discussion

Mesoporous Silica Nanoparticles (MSN)

The TG analysis was used to establish the ideal post-synthesis thermal treatment, for the complete removal of the organic template from the bare silica matrix. Figure 1 shows that the most of the weight loss occurs at temperatures below 400°C. Firstly, the removal of residual solvent causes an initial weight loss of 5%; then, the removal of the organic fraction including CTABr is related to the second minimum at 250°C of the DTG. The surfactant CTABr has a melting point of 237°C and decomposes at around 243°C. The slight difference with the obtained values could be due to its encapsulation in the pores and to an interaction between the template molecules and the internal walls of the MSN. In the 250 and 550°C range, the combustion of unreacted ethoxy groups arising from TEOS, as well as the decomposition of residual organic molecules and the condensation of neighbouring silanol groups are promoted. Above 550°C, the thermal dehydroxylation of internal surface silanol groups, that forms siloxane bridges, determines a further loss of about 2%. At higher temperature (*i.e.* 800 or 1000°C), the complete removal of the template and a detrimental synterization process take place, with the consequent decrease of the mesoporosity by pore shrinkage. After the analysis of this preliminary study, a calcination at 550°C was considered as a good compromise between a significant decomposition of the organic template and a limited sinterization.

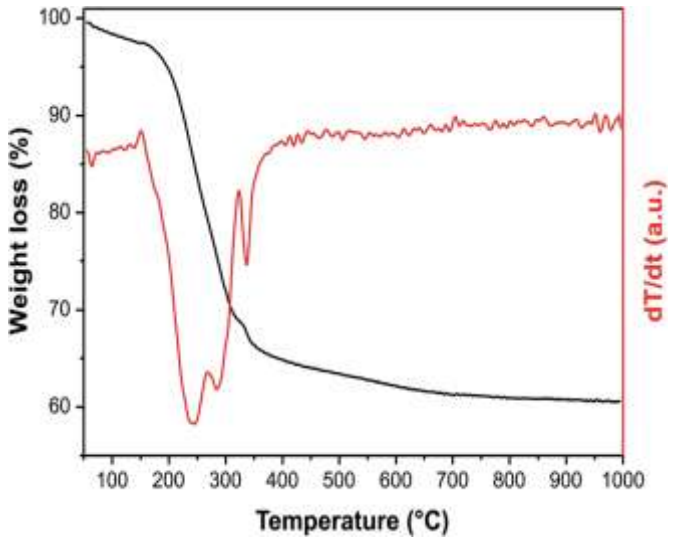

Figure 1 Thermogravimetric curve of bare MSN. The red curve is the first derivative of the weight loss (DTG).

The XRPD pattern of the calcined MSN exhibits two well-resolved diffraction peaks at 2θ = 1.60 ± 0.05° and 2.60 ± 0.05° indexed respectively as (100) and (110) and associated to an ordered hexagonal mesoporous structure (Figure 2). The calculated lattice constant (a_0) is 6.6 ± 0.3 nm, while the pore wall thickness (w_p) is 2.3 ± 0.4 nm. Since MSN is not crystalline at the atomic level, no reflections at higher angles are observed.

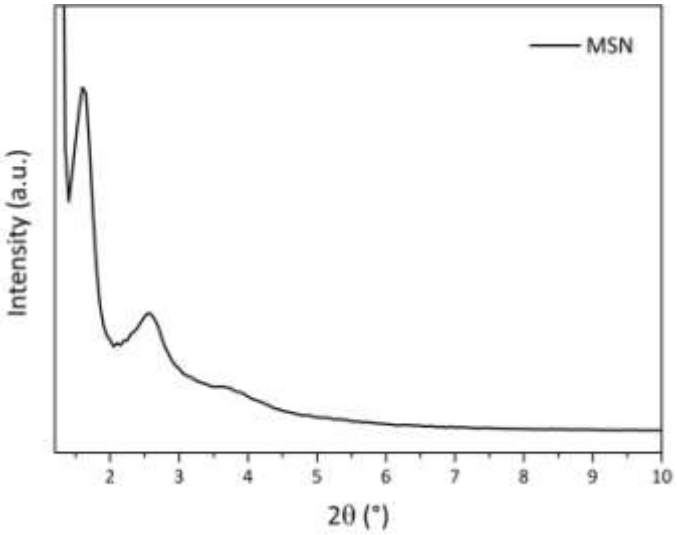

Figure 2 XRPD pattern of MSN in low-angle region.

According to the IUPAC classification, the N_2 adsorption-desorption isothermal curves at the liquid nitrogen temperature of the MSN (Figure 3a) features the typical shape of a mesoporous system with two-dimensional cylindrical channels, displaying the type IV profile with H2 hysteresis loop. Furthermore, the size and the distribution of the pores characterize the inflection points and the sharpness of the isotherms.[13] The bare silica shows a high specific surface area (900 m^2g^{-1}), which corresponds to a significant level of mesoporosity. The pore size distribution is very narrow and centered at 4.3 nm (Figure 3b). The total pore volume of the MSN, equal to around 0.90 cm^3g^{-1}, confirms the very high mesoporosity and the extensive availability of accessible internal surface area for potential embedding of various nanoparticles via wet impregnation method.

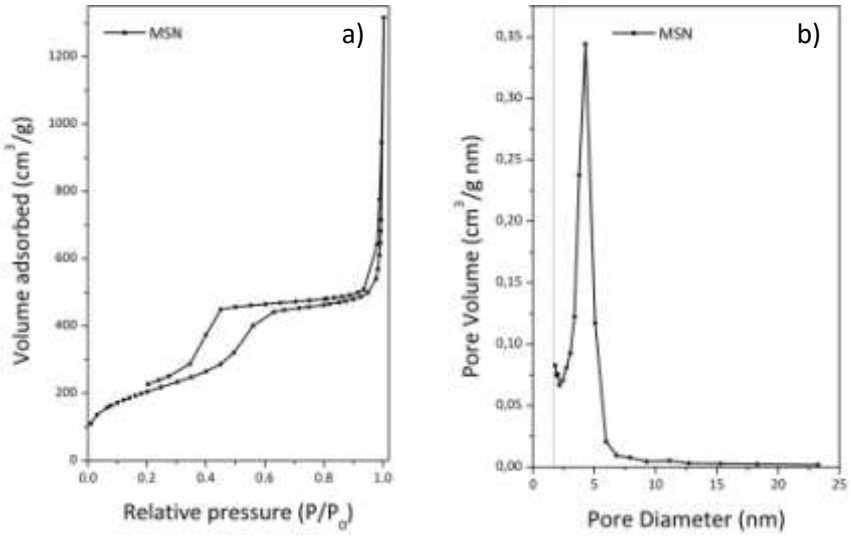

Figure 3 N_2 adsorption-desorption isotherms (a) and BJH pore size distribution (b) estimated on the adsorption branch of MSN.

TEM micrographs of the calcined silica indicate the presence of both isolated and aggregated nanoparticles with spheroidal shape and relative diameters between 100 and 200 nm (Figure 4a). In agreement with the BJH distribution, ordered two-dimensional hexagonal mesoporous structure with pore diameter of about 5 nm is observed (Figure 4b).

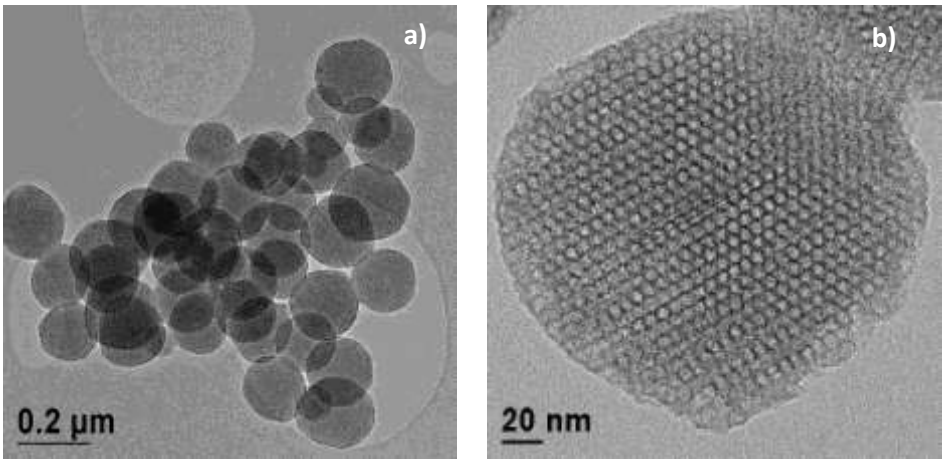

Figure 4 Representative TEM micrographs of MSN.

$xTiO_2$@MSN series

In order to have the lower loss of titanium, the best method to remove the solvent used for the impregnation of TiO_2 precursor was evaluated. In particular, the removal by rotary evaporator was compared to the removal by centrifugation. With this aim, titanium concentrations were determined by NAA before the calcination treatment and the results are reported in Table 1. Figure 5 displays the gamma ray spectra of neutron irradiated standards of titanium and silicium. The spectra show the ^{51}Ti and ^{29}Al 320.1 KeV and 1273 KeV photopeaks used for the determination of total titanium and silicium in the samples. Other peaks of radionuclides such as ^{24}Na, ^{28}Al and ^{56}Mn reflect metal impurities of Na, Al and Mn in samples.

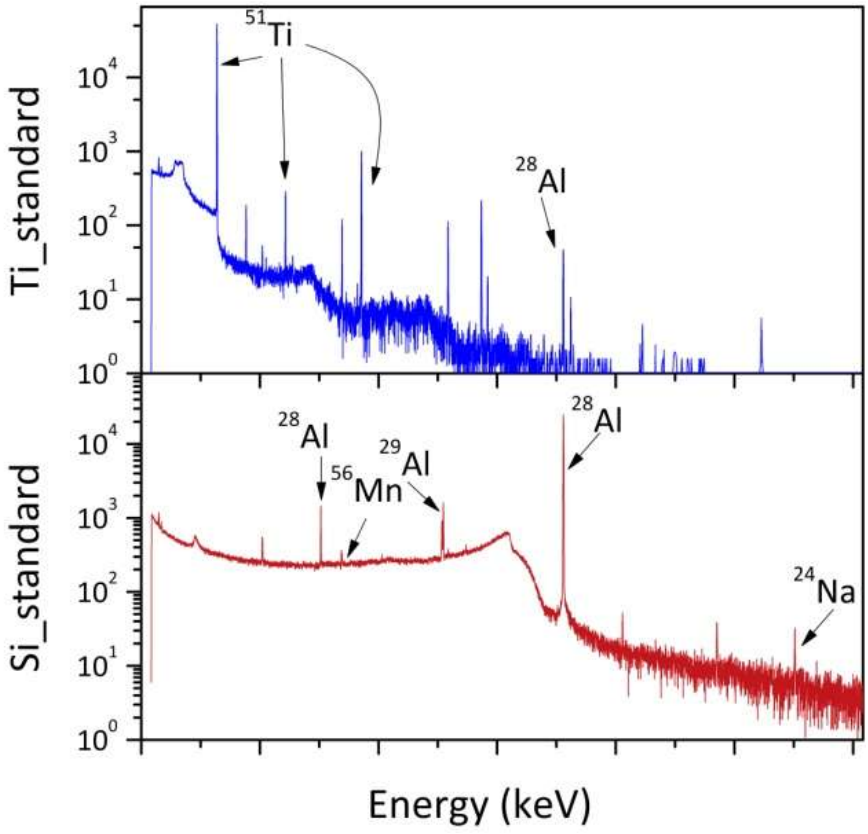

Figure 5 Gamma ray spectra of neutron irradiated standards of titanium and silicium.

As it is clearly evident in Table 1, the different preparation of the samples lead to strong differences. In particular, the centrifugation method (xTiO$_2$_cen samples) results to be the worst one, since a great loss of the precursor occurs, while the rotary evaporator (xTiO$_2$_rot samples) favors the impregnation into MSN. After this preliminary analysis, the removal of the solvent by rotary evaporator was considered as the best method and carried out for all the

samples. The quantitative analysis were performed also on the samples heat treated, confirming the good results. The values evidence that the titanium contents are greater than the expected amount determined by theoretical calculation, except for the sample with the lowest concentration (10 wt%).

Table 1 Theoretical TiO_2 concentration and titania concentration determined by NAA. SD[a] = standard deviation (mean of three determinations).

Sample	Theoretical TiO_2 concentration (%)	NAA TiO_2 concentration (%)	NAA SD[a]
10TiO_2_cen	10	2.7	±0.4
20TiO_2_cen	20	3.4	±0.5
30TiO_2_cen	30	3.5	±0.5
10TiO_2_rot	10	9	±1
20TiO_2_rot	20	31	±4.6
30TiO_2_rot	30	38.8	±5.3
40TiO_2_rot	40	52.3	±7.8
10TiO_2@MSN	10	10	±1.3
20TiO_2@MSN	20	26.6	±3.4
30TiO_2@MSN	30	32.6	±4.3
40TiO_2@MSN	40	66.8	±9.7

The efficiency of the wet impregnation method was evaluated on all the samples *x*TiO_2@MSN after the thermal treatment at 550°C by XRPD analysis.

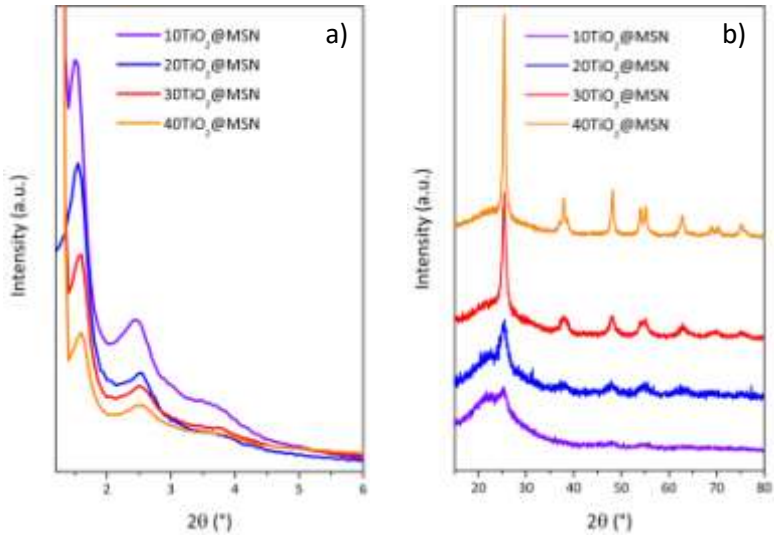

Figure 6 XRPD patterns in low (a) and wide (b) angle region of *x*TiO_2@MSN samples.

Figure 6 reports the structural investigation of the nanocomposite materials together with a comparison with the amorphous MSN. The low angle region between 1.2 and 10° (Figure 6a) show very similar patterns to the MSN one, indicating for the *x*TiO_2@MSN samples the same morphology and the hexagonal ordered structure of the silica. The loading of TiO_2 nanoparticles cause neither the collapse nor an evident modification of the silica framework. As expected, the decrease of the intensity of the peaks is ascribed to a reduction of the scattering due to the filling of the pores.[3] The 2θ values of the peaks in the wide region (15-80°), the correspond to the characteristic pattern of anatase, the only present crystalline phase of TiO_2 (PDF 21-1272). The crystallite sizes of the TiO_2 phase were determined by Line Broadening Analysis (LBA) of the peaks corrected for the instrumental broadening. The relative volume average crystal sizes of the samples are listed in Table 2.

Table 2 Physicochemical parameters derived from N_2 physisorption and from XRPD measurements of TiO_2 crystallite size. [a]Specific surface area (S.A.). [b]Mean pore size (D_p). [c]Total pore volume (V_p). [d]TiO_2 XRPD average crystallite size (D_c). The estimated error is ±10%.

Sample	S.A.[a] (m^2/g)	D_p[b] (nm)	V_p[c] (cm^3/g)	D_c[d] (nm)
MSN	900	4.3	0.9	-
10TiO_2@MSN	720	4.3	0.84	2.8
20TiO_2@MSN	665	4.2	0.76	2.6
30TiO_2@MSN	505	4.3	0.69	6.8
40TiO_2@MSN	411	4.3	0.57	13.7

In the same table the physisorption measurements evidence a decrease of specific area with the loading of titania nanoparticles. However, all the *x*TiO_2@MSN samples maintain a type IV isotherm profile and the capillary condensation occurs at relative pressures p/p_0 in the range of 0.4-0.6 (Figure 7a). This means that the very ordered mesoporous channels of the silica matrix are maintained also after the formation of TiO_2 nanoparticles (Figure 7b).

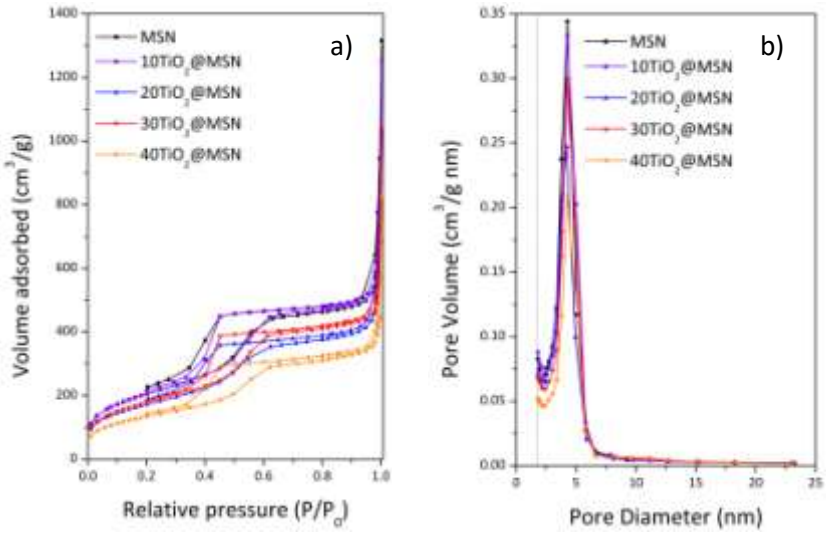

Figure 7 N_2 adsorption-desorption isotherms (a) and BJH pore size distribution estimated on the adsorption branch (b) of MSN and xTiO_2@MSN nanocomposite materials.

The comparison of the textural properties of the *x*TiO_2@MSN nanocomposites with the MSN listed in Table 2 evidence a maximum of the pore size distribution almost constant for all the nanocomposites, while the specific surface area and the total pore volume of the *x*TiO_2@MSN samples decrease with the increase of the titania content. This could suggest that TiO_2 nanoparticles are confined inside the pores of the silica matrix or block the pores aperture.

In order to evaluate the growth process of the TiO_2 nanoparticles on the bases of the different loaded %wt contents, TEM analysis was performed in all the samples. From the observations of the crystal lattice fringes, it emerged that the size of titania nanoparticles is in agreement with the silica pores dimension. Table 2 reports the statistical estimation of the particles size that are in good agreement with the average crystallite size determined by LBA. At least 300 particles have been considered for the statistics. As reported in Figure 8, for the 10TiO_2@MSN specimen the main size distribution of TiO_2 nanoparticles is in the range between 2 and 3 nm; whereas for the other samples it is around 3-4 nm.

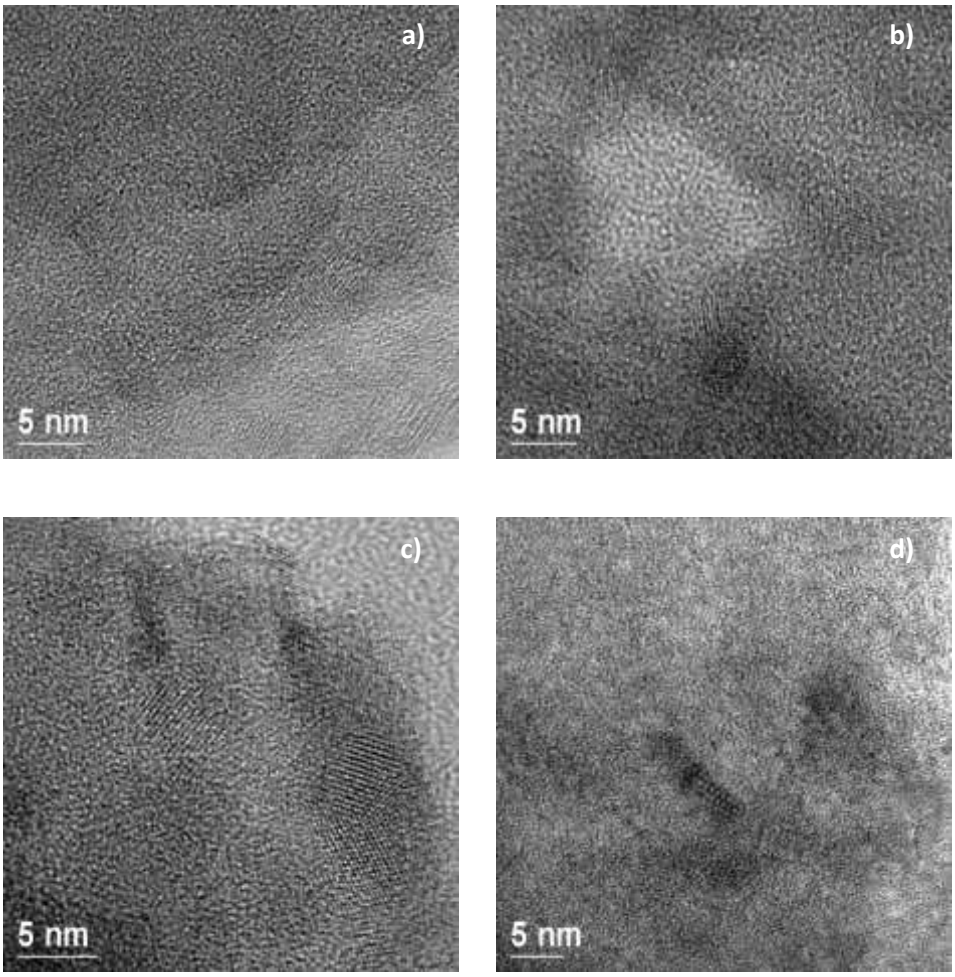

Figure 8 Representative TEM micrographs of 10TiO_2@MSN (a), 20TiO_2@MSN (b), 30TiO_2@MSN (c) and 40TiO_2@MSN (d).

Figure 9 reports the low magnification micrographs for all the samples. In the 10TiO_2@MSN and 20TiO_2@MSN specimens no TiO_2 particles are grown on the MSN surface (Figure 9a-b), while the 30TiO_2@MSN nanocomposite present a small fraction of titania nanoparticles decorating the surface of silica, with an average crystallite size slightly larger than the size of the silica channels (Figure 9c). The TEM images of 40TiO_2@MSN specimen (Figure 9d) clearly evidence not only the decoration of TiO_2 nanoparticles on the surface of MSN, but also a consistent formation of larger TiO_2 nanoparticles, outside the MSN, with sizes ranging from 7.5 to 12 nm. From these observations, it could be concluded that:

(i) for the lower titania contents (10TiO_2@MSN and 20TiO_2@MSN samples), the pores of the silica matrix are able to control the growth mechanism of TiO_2 nanoparticles, keeping their sizes within the pore diameters (*i.e.* lower than 5 nm);

(ii) for the higher TiO_2 contents (30TiO_2@MSN and 40TiO_2@MSN nanocomposites), TEM micrographs evidence the existence of two different size distributions of nanoparticles: the first with an average size smaller that the average diameter of

the silica channels, the second with an average size much larger than the average diameter of the silica channels.

The findings suggest that there is a threshold concentration: below a certain limit, the titania nanoparticles are able to grow inside the silica mesopores; when this limit is exceeded, the formation of TiO_2 takes place also on the external surface of the silica matrix, with the growth of large aggregates with sizes related to the TiO_2 content.

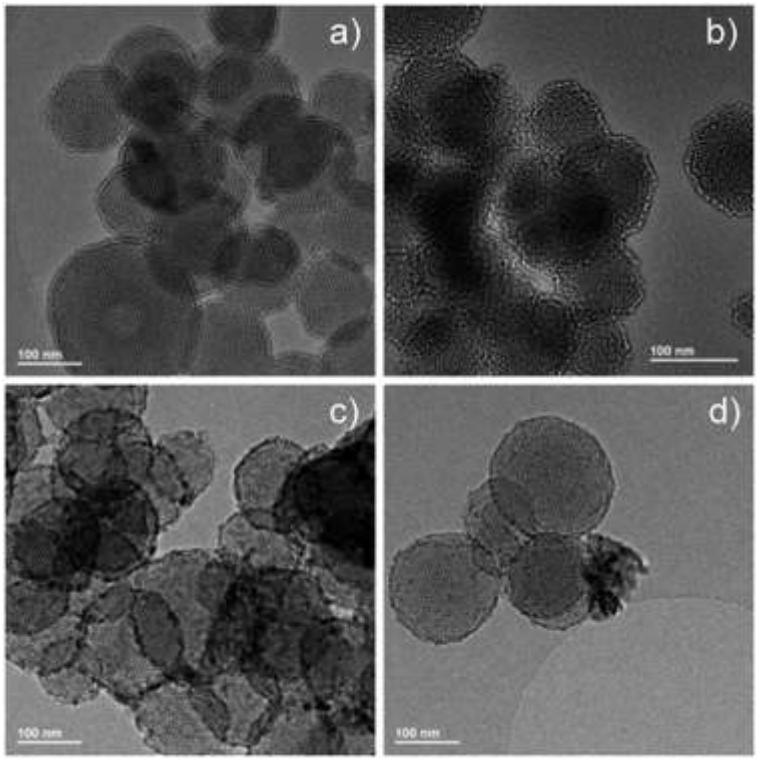

Figure 9 Representative TEM micrographs of $10TiO_2$@MSN (a), $20TiO_2$@MSN (b), 30Ti O_2@MSN (c) and $40TiO_2$@MSN (d).

In agreement with the results obtained by XRPD, the Selected Area Electron Diffraction (SAED) performed in the *x*TiO_2@MSN samples reveals a series of ring patterns indexed as the anatase phase of TiO_2. The EDX measurements show the presence of Ti, Si and O, confirming that the titania nanoparticles are well dispersed inside the silica matrix.

The surface chemical composition of the nanocomposites was confirmed by XPS analysis as shown in Figure 10. With the increasing loading of TiO_2, the binding energy value for Ti $2p_{3/2}$ shifts to lower values up to 458.3 eV for the $40TiO_2$@MSN sample. This result approaches to the values reported for pure TiO_2 nanospheres.[4] The binding energy of Si 2p (103.3-103.5 eV) are closed to the values found for SiO_2. Since the relative intensities of Si and Ti peaks show that the values of surface Si/Ti atomic ratios are lower than the theoretical ones (Table 3), it

can be concluded that titanium is mainly on the surface of the silica nanoparticles. In particular, with higher contents of titanium the observed difference is less pronounced: in the case of 40TiO_2@MSN sample the surface Si/Ti ratio is 1.24 while the theoretical one should be 2.00. This suggests that, with a high content of titanium, the fraction of titanium incorporated into the mesoporous channels is much higher.

Table 3 Comparison between the theoretical and surface Si/Ti atomic ratios determined by XPS.

Sample	Si/Ti theoretical	Si/Ti surface
10TiO_2@MSN	11.96	4.11
20TiO_2@MSN	5.32	3.34
30TiO_2@MSN	3.10	1.77
40TiO_2@MSN	2.00	1.24

Figure 10 reports the evolution of the O 1s core level signals relative to the TiO_2 content. These spectra can be decomposed in at least three contributions at 530.1, 531.1 and 532.8 eV, as shown in Figure 10b for 10TiO_2@MSN. The contribution at higher BE is assigned to oxygen of the MSN while the contribution at lower BE is attributed to oxygen from TiO_2.[5] The contribution at 531.1 eV has been attributed to Ti-O-Si.[6] The O 1s spectra presented in Figure 10 suggest significant differences among the samples depending on the TiO_2 content. The relative intensity of the contribution at 531.1 eV is appreciable for 10TiO_2@MSN and 20TiO_2@MSN, where a strong interaction between titania and silica occurs. This is in agreement with the formation of small anatase crystallites, as evidenced by XRPD analysis, in strong contact with MSN mainly within the channels. The contribution at 531.1 eV is very weak, while the relative intensity of the contributions due to titania at 530.1 eV shows a significant increase for the samples with higher titania contents, in agreement with the formation of TiO_2 nanoparticles on the external surface of MSN. These results, in combination with TEM observations, suggest that a critical threshold in the TiO_2 loading exists between 20 and 30 wt%. Below this threshold, a strong interaction between silica and TiO_2 takes place, resulting in highly dispersed Ti-species and/or small TiO_2 nanoparticles mainly inside the MSN channels. Above the critical threshold, the amount of TiO_2 is large enough to completely cover

the surface and the growth of TiO_2 nanoparticles takes place also on the external surface of the MSN, as revealed by TEM and XPS investigations. Moreover, the mean crystallite size of TiO_2 increases because their growth is not limited by the nanometric diameter of the pores of MSN.

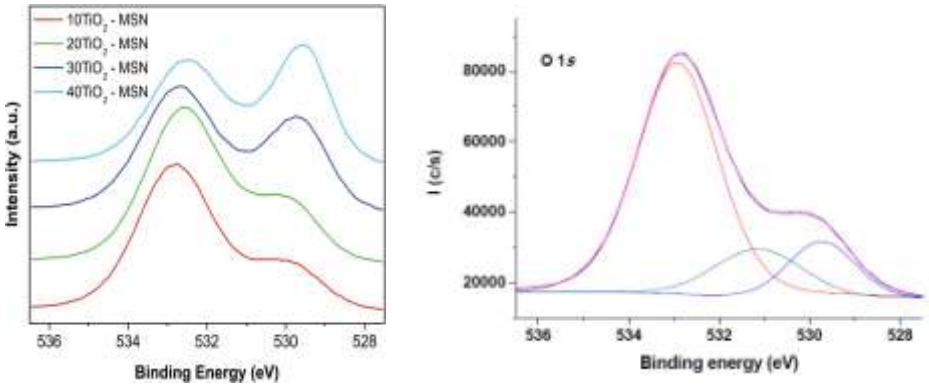

Figure 10 O1s core level XPS spectra for *x*TiO_2@MSN (a), contributions of O1s for 10TiO_2@MSN.

The diffuse reflectance UV-vis spectra for all the samples evidence a strong absorption of light below 400 nm (Figure 11a). Since, as it is known, in this range the contribution of pristine MSN is negligible, the spectra confirm that the UV-vis absorption of the samples is due to only to the presence of the titania nanoparticles, that act as UV filters. The content of titania influences the absorption edge, in fact, as depicted by the aforementioned figure, the decrease of titania fraction coincides with a shift of the UV absorption edge to shorter wavelengths. To estimate the band gap energy, the plots of $(K\text{-}M\cdot h\nu)^{1/2}$ versus photon energy ($h\nu$) are reported in Figure 11b. The same methodology have been previously adopted to determine the band gap of indirect bandgap semiconductors such as titania.

As shown in Table 3, the energy band gap values are in the range of 3.2 and 3.8 eV and they decrease with the increase of titania content. The slight blue shift and the correspondent increase in the E_g values could be reasonably associated to the well-known quantum size confinement resulting from the decrease in crystallite size of titania.[3, 7] From the literature, the blue shift in the absorption edge has been ascribed to the existence of Ti-O-Si chemical bonds.[8]

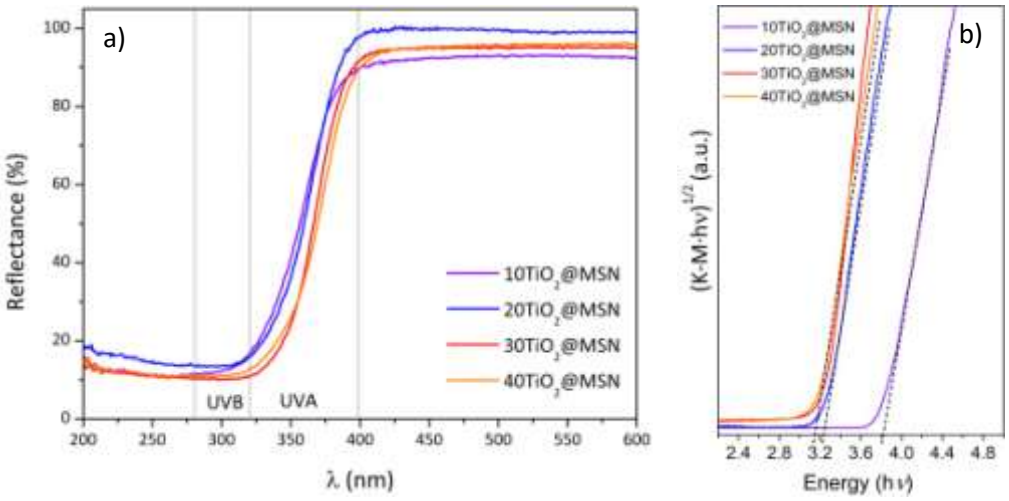

Figure 11 DR-UV spectra (a) and Kubelka-Munk function *vS* Energy (b) of *x*TiO_2@MSN samples.

In agreement with this findings, the largest blue shift is observed for the sample with the lower TiO_2 content, in which the Ti-O-Si contribution represents the most important Ti-related species as revealed by XPS analysis. This effect has been previously observed in the case of other titania-silica composites prepared by different techniques.[8-9]

Table 4 Band gap energy values *x*TiO_2@MSN samples.

Sample	Energy gap (eV)
10TiO_2@MSN	3.8
20TiO_2@MSN	3.2
30TiO_2@MSN	3.2
40TiO_2@MSN	3.2

Photocatalytic activity

As widely discussed in Chapter 1, titania-based materials are semiconductor and consequently powerful photocatalyst. As shown in Figure 9, from TEM analysis it is clearly evident that titania nanoparticles are available to the environment and they could be reached by organic molecules triggering radical reactions. In order to verify the photocatalytic properties of the samples, the degradation of dyes (methylene blue and methyl orange) and drugs (paracetamol) in aqueous suspension are tested after some preliminary tests. Trials, both without photocatalyst and only with bare MSN, were carried out, showing a negligible reduction of the organic compounds after 240 minutes. These experimental proofs show that the sacrificial molecules are stable under UV irradiation, and their eventual degradation is due solely to the photocatalyst. The photostability of MO is reported as example in Figure 12.

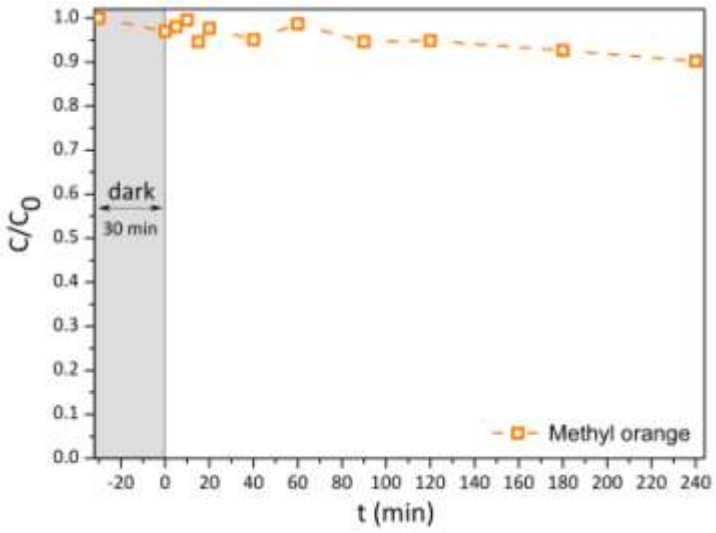

Figure 12 MO photostability under UV irradiation.

Methylene blue (MB) degradation. During the photocatalytic degradation of the cationic dye reported in Figure 13, a significant amount of dye is adsorbed on the surface of the samples after 30 min of equilibration in the dark. The adsorption decreases from 75% to 35%, passing from the 10TiO_2@MSN to the 40TiO_2@MSN samples, could be related to the decrease of the surface area values and to a potential selective adsorption of MB on the silica fraction of the *x*TiO_2@MSN composites.

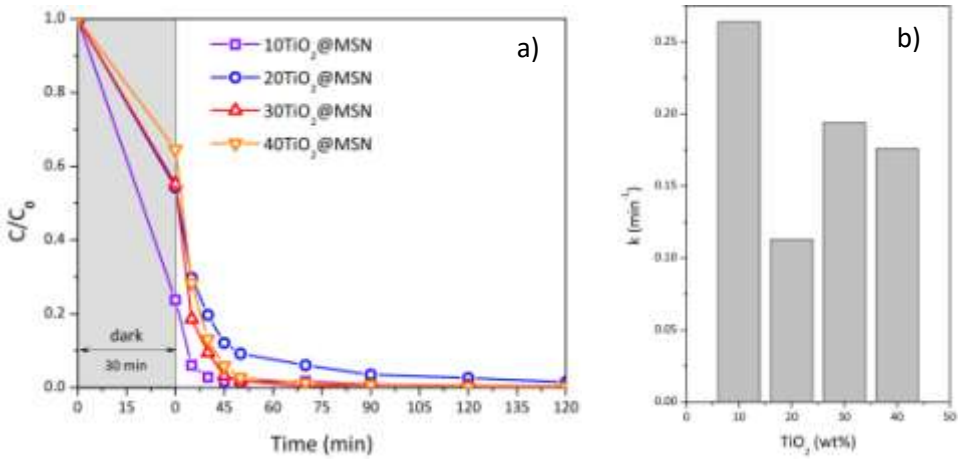

Figure 13 Performances of adsorption and MB photodegradation on *x*TiO_2@MSN catalysts before and under UV-vis irradiation (a), with the calculated kinetic constants (b).

In the case of a charged dye, the adsorption in the dark depends on both the surface area and the Point of Zero Charge (PZC) of the samples. Usually, in the case of materials based on titania loaded in MSN, the PZC values are lower than 4 pH unit.[10] Therefore, in our experimental conditions (slightly acidic pH) a deprotonation of the catalyst surface occurs, with a coverage of negatively charged moieties, able to adsorb the cationic dye on the MSN exposed surface. The adsorption of large amounts of MB on these materials was extensively reported in literature.[10]

After the UV-vis irradiation, the concentration of the dye decreases exponentially with the time for all the series. Pseudo-first order kinetic constants (*k*) are calculated plotting $\ln(C_0/C)$ *vS* time for the first part of the exponential decay curves and the kinetic constant *k* values are reported in Figure 13b. The sample with the lowest content of titania ($10TiO_2$@MSN) shows the highest value of *k* (0.264 min^{-1}). This result could be influenced by the very strong adsorption occurred during the dark (75%). For the other samples of the series, that show a comparable dye adsorption (35-45%), a trend in the values of *k* with a relative maximum for $30TiO_2$@MSN sample (0.194 min^{-1}) is observed.

In order to monitor the presence of organic by-products in solution after the UV-vis irradiation, UV-vis spectra in the 300-900 nm range of the solutions were collected at different reaction time. Figure 14 displays no new absorption bands detected, suggesting that the intermediate compounds are easily oxidized and decomposed to small fragments. The ICP analysis performed on the recovered solutions at the end of the photocatalytic experiments show the presence of chlorides and sulphates compounds with a stoichiometric ratio in agreement with the initial MB concentration. Moreover, traces of anions such as formiate, acetate, oxalate (intermediate products arising from the degradation of the organic skeleton) and nitrate, and of cations such as ammonium ions are revealed. Ammonium ions releasing

from N-containing functional groups are partially converted into nitrates compounds during the degradation experiments.[11] The obtained results indicate that MB is completely decomposed forming inorganic ions and only minor amounts of non-toxic compounds. The degradation sequence of MB by TiO_2-based materials has been studied in detail by Houas *et al*. by LC/MS and GC/MS analysis for the determination of the intermediate compounds.[12] Firstly, the degradation pathway starts with the oxidation of S, with the formation of a sulphonic group and the opening on the central aromatic ring and the formation of NH_2 group. The dissociation of the two benzenic rings, with the consequent formation of sulphonic acid and aniline substituted with dimethylamino groups occur after further oxidation by reaction with $OH^{\cdot}$ radicals. Subsequent reaction of these by-products with $OH^{\cdot}$ causes the formation of hydroxylated phenols, the opening of the aromatic ring and its mineralization through the formation of carboxylic acids. The degradation of the aromatic ring is accompanied by the release of sulphates and ammonium ions into the aqueous media.

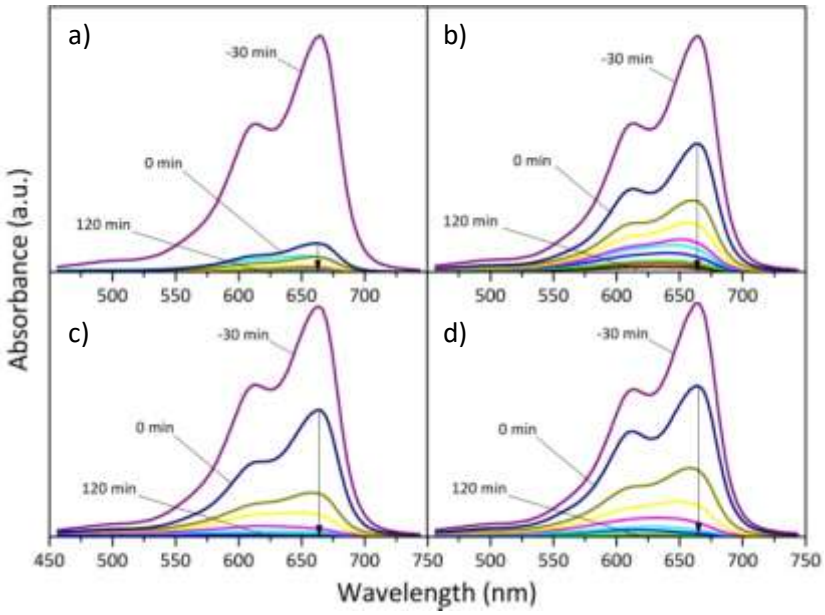

Figure 14 Degradation profiles of aqueous methylene blue (MB) under UV-vis illumination over $10TiO_2$@MSN (a), $20TiO_2$@MSN (b), $30TiO_2$@MSN (c) and $40TiO_2$@MSN (d).

The sample with the best photocatalytic performances ($30TiO_2$@MSN) was chosen for the reusability test. After the first degradation experiment, the dye was introduced in the reactor restoring the initial concentration. The degradation of MB was checked during four consecutive cycles, observing a slight minimal decrease of the photocatalytic performances as shown in Figure 15. Nevertheless, a complete destroy of MB molecules is always achieved

after 120 min of UV irradiation. The progressive deactivation could be related to the increasing accumulation of inorganic anions (*i.e.* chloride, sulphates and nitrates) in the solution.

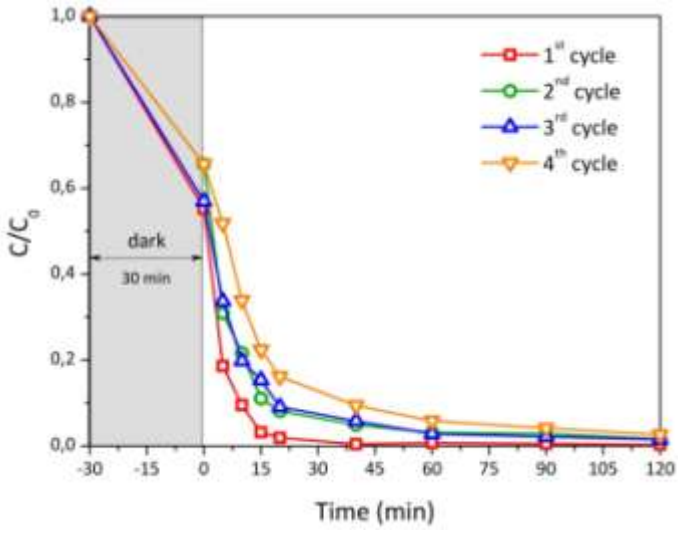

Figure 15 Degradation profiles of aqueous methylene blue (MB) under UV-vis illumination during four consecutive experiment over 30TiO_2@MSN.

The results from photocatalytic degradation suggest that the two components of the materials (TiO_2 and MSN) have a strong synergy in the photocatalytic performances in water remediation. The role of TiO_2 and the silica matrix is complementary: MSN adsorbs MB from the solution through electrostatic attraction of the surface Si-$O^{\delta-}$ groups, while the TiO_2 nanocrystals provide the photoactive sites producing the $OH^{\cdot}$ radicals required for the degradation of MB. In this context, the maximum in photoactivity demonstrated by 30TiO_2@MSN could be explained considering that this titania concentration is just above the critical threshold of its incorporation inside the channels of MSN: as shown by TEM analysis (see Figure 9) TiO_2 nanoparticles are mainly located inside the pores with a small fraction decorating the surface of MSN. This finding results in the closest interaction between the sites of adsorption of the dye and the sites for $OH^{\cdot}$ production inside the channels of the silica matrix. A cooperative effect between TiO_2 and MSN was previously found in the degradation of cationic dyes[10] for composites with higher TiO_2 contents (60-90%). In these studies, we can suggest that the inner surface of pores was pre-enriched by adsorption of the dye in MSN surface. The decomposition of MB was promoted by the photoactive titania moieties while the complete mineralization was due to the confinement of intermediate products inside the mesopores. Beyers *et al*. [13] demonstrated that the embedding of titania nanoparticles inside

the channels of MSN-based materials is essential to obtain a high photocatalytic performance in the degradation of cationic dyes.

Methyl orange (MO) degradation. The photocatalytic tests were also performed using the methyl orange, a negatively charged dye in a wide pH value range. Figure 16a shows that the amount of dye adsorbed on the materials after the equilibration in the dark (t = 0) is proportional to the TiO_2 fraction present in the nanocomposite, with an increase from 1.8% to 21.8% of the initial amount of MO as the titania concentration increases from 10 to 40%$_{wt}$. This result suggests that, differently from the case of MB, MO adsorption take place preferentially on the TiO_2 nanoparticles surface. The PZC of anatase is about 5.3-5.6 (depending on the working condition and measurement technique)[14], values close to the natural pH of the dye solution (slightly acidic pH). Therefore, the adsorption of an anionic dye, such as MO, is less favoured with respect to a cationic dye (MB) and, in any case, it should take place on the TiO_2 fraction, presenting a PZC value significantly higher than that of the SiO_2 content.

The photocatalytic activity in the decolourization of MO increased up to the TiO_2 content of 30 wt%. A further increase to 40 wt% resulted in a significant decrease of the performance. In agreement with this result, the kinetic constants, calculated from a first-order kinetic, show a maximum for the 30TiO_2@MSN material (0.0699 min^{-1}), as showed in Figure 16b.

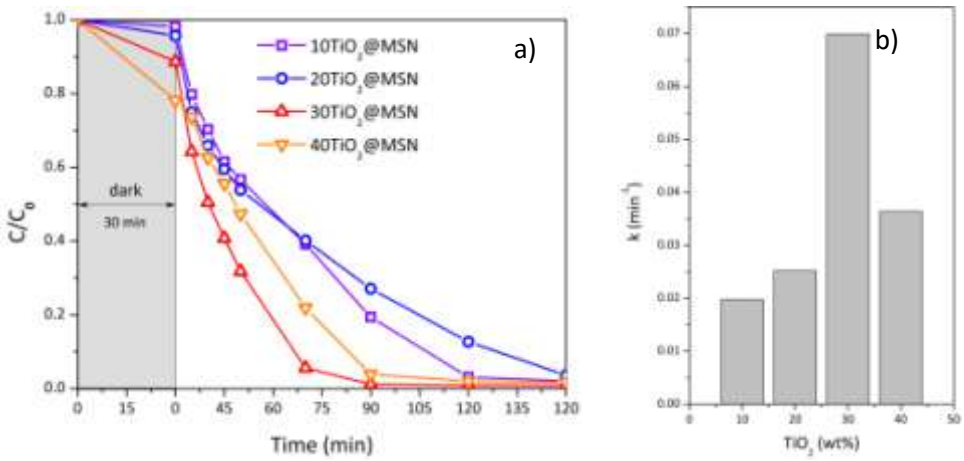

Figure 16 Performances of adsorption and MO photodegradation on xTiO$_2$@MSN catalysts before and under UV-vis irradiation (a), with the calculated kinetic constants (b).

The presence of organic intermediates has been checked analyzing the UV-vis spectra in the 300-900 nm range of the solutions collected at different reaction times. Also in this case,

the appearance of new absorption bands was not occur (Figure 17), indicating that degradation of MO and of its aromatic by-products were fast under the photocatalytic conditions adopted. The pathway of photocatalytic decomposition of MO in aqueous solution has been already studied by HPLC-MS by Baiocchi *et al*.[15] The reaction of MO with photo-generated $OH^{\cdot}$ leads to the demethylation of the dimethylamino group, hydroxylation of the aromatic rings and substitution of the sulphonic group with a OH group. Further oxidation and fragmentation of the molecule leads to the aniline and sulphonic acid, eventually hydroxylated on the aromatic ring and/or substituted with the azo group. Finally, further decomposition produces sulphates, N_2 and NH_4^+ and different carboxylic acids after oxidation and opening of the benzenic ring.

The ICP analysis of the recovered solutions after the photocatalytic experiments showed the presence of Na^+ in good stoichiometric ratio with respect to the initial MO concentration and traces of NH_4^+ deriving from the degradation of dimethylamino group. Also in this case, traces of anions (formiate, acetate, oxalate, sulfates and nitrate) have been detected, as by-products of the degradation of the organic skeleton and from the oxidation of NH_4^+.[11] Notably, the amount of SO^{4-} ions detected in solution is in good stoichiometric ratio with the initial amount of MO. These results indicate that skeleton of MO is completely degraded during the degradation experiments with the production of inorganic ions and only minor amounts of non-toxic compounds.

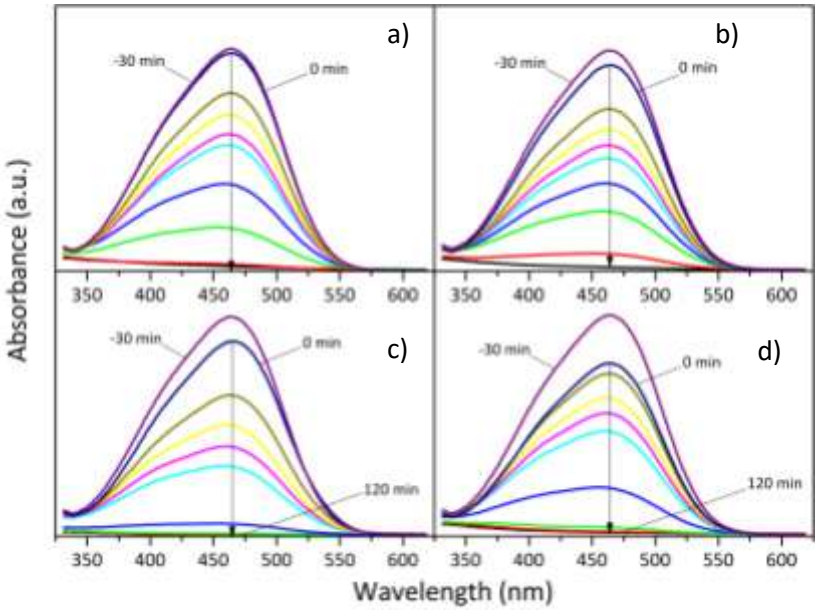

Figure 17 Degradation profiles of aqueous methyl orange (MO) under UV-vis illumination over $10TiO_2$@MSN (a), $20TiO_2$@MSN (b), $30TiO_2$@MSN (c) and $40TiO_2$@MSN (d).

The trend observed for MO decolourization on the *x*TiO_2@MSN samples (Figure 16) could be due to the combination of several factors. The adsorption of the dye takes place mainly on the surface of TiO_2 nanoparticles, with various important consequences:

(i) the TiO_2 surface is less available for the adsorption of water, reducing the formation of $OH^{\cdot}$ radicals responsible for the dye decolourization in solution;

(ii) considering the absorption spectrum of the dye, MO (both adsorbed and/or in solution) could act as a light filter, limiting the number of photons with the correct energy approaching the surface of the photocatalyst and therefore reducing the ability to produce the radical species responsible for dye degradation;

(iii) at the same time, adsorbed MO could act as a sensitizer, absorbing photons and transferring electrons from the excited state of the dye to the conduction band of TiO_2.[16]

The first two conditions lead to the suppression of the photocatalytic activity while the latter enhances the performances of the semiconductor photocatalysts. In the present case, 30TiO_2@MSN sample shows the highest photocatalytic activity as a result of the best compromise between the opposite effects induced by adsorbed MO. For this reason, the 30TiO_2@MSN nanocomposite has been selected for the reusability test. The results are presented in Figure 18. The performance of the photocatalysts slightly decreases during various cycles of reaction, even though the complete degradation of MO solution is always achieved within the 2 h of irradiation. Also in this case, this result can be related with the accumulation of the inorganic by-products (Na^+, NH_4^+, sulphates, nitrates) in the aqueous solution.

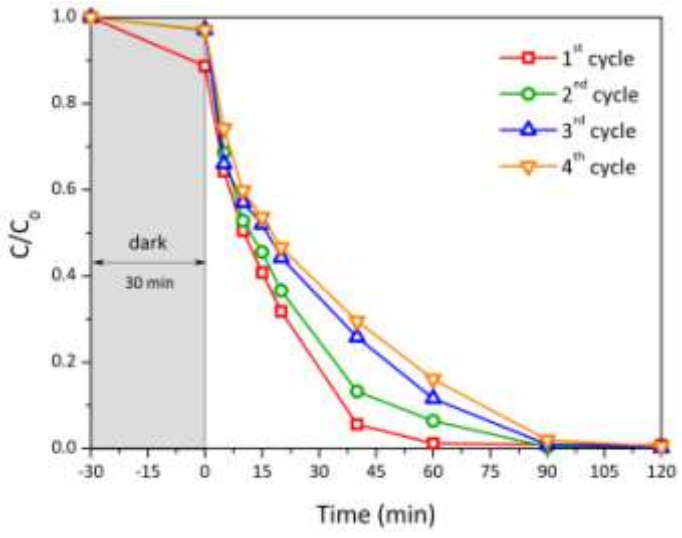

Figure 18 Degradation profiles of aqueous Methyl Orange (MO) under UV-vis illumination during four consecutive experiment over 30TiO_2@MSN.

Paracetamol degradation. The *x*TiO_2@MSN samples were tested also in the photocatalytic degradation of paracetamol, a neutral molecule that contains a phenolic ring, one of the most recalcitrant moiety to be degraded by decontamination techniques. Figure 19 shows the degradation of paracetamol as a function of irradiation time under UV-vis light. In this case, the amount of paracetamol adsorbed on the surface of the photocatalysts is always negligible (lower than 2%), due to the neutrality of the target molecule. During the UV irradiation, the behaviour of the samples depends on the amount of TiO_2. In the case of 10TiO_2@MSN and 20TiO_2@MSN, the concentration of paracetamol decreases monotonically.

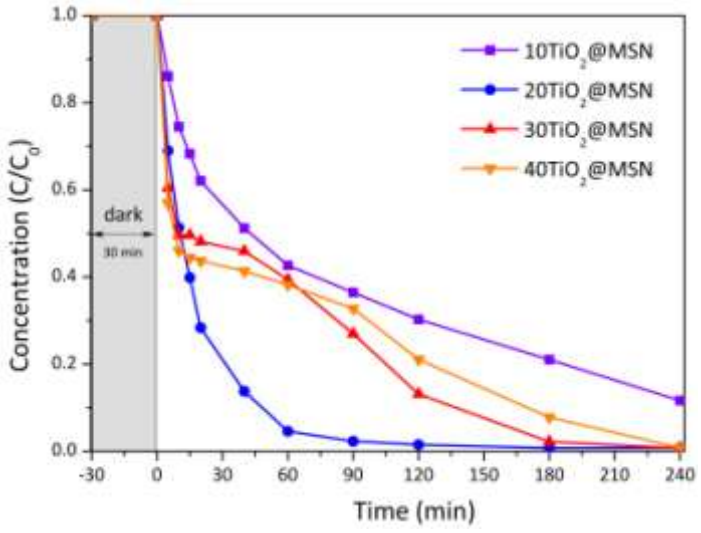

Figure 19 Performances of adsorption and paracetamol photodegradation on *x*TiO_2@MSN catalysts before and under UV-vis irradiation.

Figure 20 evidences the appearance of new bands in the UV-vis spectra of the recovered solution. These new bands are centred at 215 nm (present also after complete conversion of paracetamol) and at 320 nm (even with a low intensity and disappearing after 30-40 min of irradiation). Increasing the TiO_2 content (30 and 40%), the degradation of paracetamol is very fast in the first 20 minutes. After this interval, the paracetamol decomposes slowly and, after about 90 minutes of irradiation, the degradation rate increases again. In these last cases, the band at 215 nm is always less intense than the band observed in the case of the sample with a lower loading of TiO_2 and the intensity of the band at 320 nm is negligible (Figure 20).

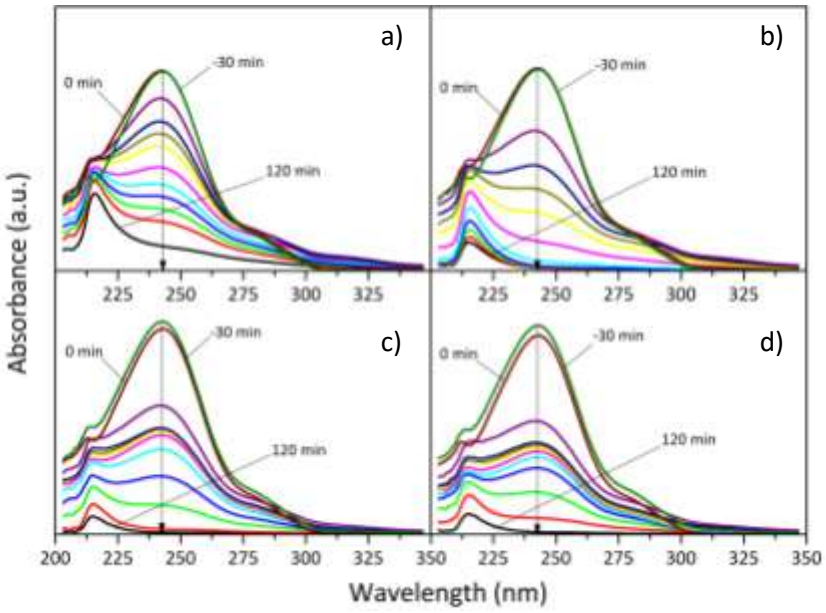

Figure 20 Degradation profiles of aqueous paracetamol under illumination over 10TiO_2@ MSN (a), 20TiO_2@MSN (b), 30TiO_2@MSN (c) and 40TiO_2@MSN (d).

The mechanism of paracetamol degradation under photocatalytic conditions have been previously studied.[17] Generally, the reaction involves the deacylation of the molecule and the hydroxylation of the aromatic ring, with the production of p-aminophenol, N-(3,4-dihydroxyphenyl)-acetamide, N-(2,4-dihydroxyphenyl)-acetamide and hydroquinone as by-products. Finally, the phenolic ring, broken by reaction with $OH^{\cdot}$ radicals, promotes the formation of dicarboxylic acids that will be further degraded until complete mineralization. The formation of p-aminophenol has been evidenced by the increase in the absorbance at 320 nm[17a] while absorption band at 215 nm can be associated with the production of the dicarboxylic acids. Moreover, the ICP analysis of the recovered solutions revealed the presence of NH_4^+, NO^{3-}, formiates, acetates and oxalates. NH_4^+ is the product of the mineralization of the amide group and produces nitrates by oxidation,[11] while the other intermediates represent the last steps in the degradation of the dicarboxylic acids produced by the opening of the phenolic ring.

The TiO_2 content and the consequent different morphology of the composites, observed by TEM, strongly influences the behaviour of *x*TiO_2@MSN samples. Titania nanoparticles grown mainly inside the channels of MSN matrix up to an amount of 20 wt% and the molecules in the solution must diffuse into the pores to reach the photocatalytic sites. Considering the diameter of the pores (~4.3 nm), the diffusion of paracetamol could be strongly hindered with respect the diffusion of water. Moreover, paracetamol is only weakly adsorbed on the surface of the materials as shown in Figure 19. Therefore, it is reasonable that the photoactive surface of TiO_2 can be reached mainly by water resulting, after activation by UV irradiation, in the

production of large quantities of $OH^{\cdot}$ radicals. The radicals can be released in the solution and can react with paracetamol to form, fist, p-aminophenol and then dicarboxylic acids, following the mechanisms previously proposed for the photocatalytic degradation of this molecule.[17b] Increasing the loading of titania, some TiO_2 nanoparticles grown also outside the MSN matrix. In this case, the outermost surface of the material is available for the photocatalytic reactions. Therefore, the initial rate of degradation of paracetamol is very high but the adsorption of intermediate compounds produced by the partial decomposition of paracetamol could hindered the surface to the degradation reactions. In particular, positively charged (NH_4^+) or basic compounds (p-aminophenol) are present among the by-products of paracetamol decomposition. The deactivation of the reaction, by adsorption of the intermediates on the surface, is suggested by the low intensities of the bands related to p-aminophenol and dicarboxylic acids in solution. The degradation rate of paracetamol remains low for a certain period (from 30 to 90-120 min of reaction). During this time, an equilibrium should take place between the degradation of the molecules adsorbed on the surface, the production of $OH^{\cdot}$ radicals on the free photocatalytic sites and the adsorption of the new intermediate. Once a certain amount of the intermediates is fully degraded and removed from the surface, the rate of paracetamol degradation increases again (after 90-120 min of irradiation) until the complete mineralization of the molecules is obtained.

Based on the photocatalytic results reported in Figure 19, the $20TiO_2$@MSN sample has been selected for the reusability experiment. The results of the four consecutive tests are shown in Figure 21.

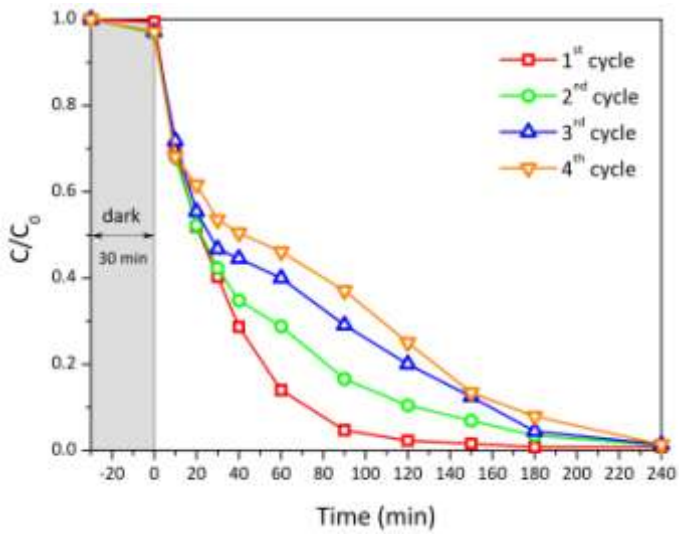

Figure 21 Degradation profiles of aqueous paracetamol under UV-vis illumination during four consecutive experiment over $20TiO_2$@MSN.

Even though paracetamol is always completely degraded after 4 h of irradiation, a progressive loss of performance was observed in the central interval of the experiments. In agreement with the considerations reported above, also in this case the decrease of the paracetamol degradation can be ascribed to the interference of the inorganic by-products produced during the previous experiment. In particular, the adsorption of by-products as nitrates could hinder the formation of OH· while the adsorption of ammonium ions or carboxylate molecules (formiates, acetates, oxalates) could be oxidized instead of paracetamol itself. Moreover, it must be underlined that the initial concentration of paracetamol is higher than that employed during degradation of MB and MO. Therefore, also the concentration of inorganic by-products is higher, finally leading to a deeper deactivation.

3.3 Conclusions

In summary, nanocomposite materials based on pure anatase TiO_2 nanoparticles confined inside the channels of ordered mesoporous silica nanospheres, with very high surface area and narrow pore size distribution centred at 4.3 nm, have been synthesized.

The *x*TiO_2@MSN composites, containing 10 wt%, 20 wt%, 30% and 40 wt% of TiO_2, were obtained by the reaction of MSNs and titanium isopropoxide as titanium source.

XPS results and TEM micrographs suggest that a critical threshold in the TiO_2 loading exist between 20 and 30 wt%. Below this threshold, the TiO_2 nanoparticles grow into the constricted space of the mesopores of MSNs, keeping their sizes in the range of the pore diameters; when amount of TiO_2 exceeds this threshold, the growth of TiO_2 occurs also on the external surface of the silica network.

For the samples with the lower TiO_2 content, a strong interaction between titania and silica occurs, as evidenced by XPS measurements.

TEM investigations evidence that titania nanoparticles are available to the external environment, suggesting that they could be reached by organic molecules triggering radical reaction.

To verify the photocatalytic properties of the samples, different organic sacrificial molecules were chosen. The results from photocatalytic degradation of pollutant compounds suggest that *x*TiO_2@MSN samples provide a good combination of potential adsorptive and photocatalytic properties.

The role of the two components (the photocatalyst TiO_2 and the silica matrix) seems to be complementary to obtain good performances in water remediation. In MB degradation, mesoporous silica nanospheres adsorb the cationic dye while the anatase TiO_2 nanocrystals

provide the photoactive sites for the dye degradation. In particular, the high activity demonstrated by 30TiO_2@MSN could be explained considering that this composition presents TiO_2 nanoparticles mainly located inside the MSN pores, with a small fraction decorating the surface of MSN. In MO and paracetamol degradation, the adsorption of the target molecules on TiO_2 inside the pores of the MSN support is limited by the diffusion. These features results in the protection of the photoactive material with respect to the adsorption of large amounts of organic compounds (target molecules or by-products of their partial degradation). Increasing the amount of TiO_2, the photoactive oxide is present also on the external surface of the mesoporous silica nanospheres and can be easily deactivated by adsorption of by-products. Finally, also considering the low amount of titania loaded, this type of nanocomposites could offer a simply way to tune the nanoarchitecture of a material, controlling the size and dispersion of the active phase present in the system, thus improving the catalytic behavior.

In the light of the results obtained, it is evident that *x*TiO_2@MSN systems can not used in the cosmetic field and a different strategy must be taken to reduce the photocatalytic activity of the synthesized UV filters.

References

[1] S. Ma, Y. Wang, Y. Zhu, *Journal of Porous Materials* **2010**, *18*, 233-239.

[2] N. B. Lihitkar, M. K. Abyaneh, V. Samuel, R. Pasricha, S. W. Gosavi, S. K. Kulkarni, *Journal of Colloid and Interface Science* **2007**, *314*, 310-316.

[3] L. Zhao, J. Yu, *Journal of Colloid and Interface Science* **2006**, *304*, 84-91.

[4] J. Zhang, X. Liu, S. Wang, S. Wu, B. Cao, S. Zheng, *Powder Technology* **2012**, *217*, 585-590.

[5] J. F. Moulder, J. Chastain, *Handbook of X-ray Photoelectron Spectroscopy: A Reference Book of Standard Spectra for Identification and Interpretation of XPS Data*, Physical Electronics Division, Perkin-Elmer Corporation, **1992**.

[6] N. Guo, Y. Liang, S. Lan, L. Liu, G. Ji, S. Gan, H. Zou, X. Xu, *Applied Surface Science* **2014**, *305*, 562-574.

[7] aJ. Yang, J. Zhang, L. Zhu, S. Chen, Y. Zhang, Y. Tang, Y. Zhu, Y. Li, *Journal of Hazardous Materials* **2006**, *137*, 952-958; bF. E. Osterloh, *Chemical Society Reviews* **2013**, *42*, 2294-2320.

[8] aT. Ohno, S. Tagawa, H. Itoh, H. Suzuki, T. Matsuda, *Materials Chemistry and Physics* **2009**, *113*, 119-123; bT. M. R. Viseu, B. Almeida, M. Stchakovsky, B. Drevillon, M. I. C. Ferreira, J. B. Sousa, *Thin Solid Films* **2001**, *401*, 216-224.

[9] aJ. Marugán, M.-J. López-Muñoz, R. van Grieken, J. Aguado, *Industrial & Engineering Chemistry Research* **2007**, *46*, 7605-7610; bK. Balachandran, R. Venckatesh, R. Sivaraj, P. Rajiv, *Spectrochimica Acta Part A: Molecular and Biomolecular Spectroscopy* **2014**, *128*, 468-474; cD. Arun Kumar, J. Alex Xavier, J. Merline Shyla, F. P. Xavier, *Journal of Materials Science* **2013**, *48*, 3700-3707.

[10] aW. Dong, Y. Sun, C. W. Lee, W. Hua, X. Lu, Y. Shi, S. Zhang, J. Chen, D. Zhao, *Journal of the American Chemical Society* **2007**, *129*, 13894-13904; bW. Dong, Y. Sun, Q. Ma, L. Zhu, W. Hua, X. Lu, G. Zhuang, S. Zhang, Z. Guo, D. Zhao, *Journal of Hazardous Materials* **2012**, *229–230*, 307-320.

[11] aG. K. C. Low, S. R. McEvoy, R. W. Matthews, *Environmental Science & Technology* **1991**, *25*, 460-467; bK. Nohara, H. Hidaka, E. Pelizzetti, N. Serpone, *Journal of Photochemistry and Photobiology A: Chemistry* **1997**, *102*, 265-272.

[12] A. Houas, H. Lachheb, M. Ksibi, E. Elaloui, C. Guillard, J.-M. Herrmann, *Applied Catalysis B: Environmental* **2001**, *31*, 145-157.

[13] E. Beyers, E. Biermans, S. Ribbens, K. De Witte, M. Mertens, V. Meynen, S. Bals, G. Van Tendeloo, E. F. Vansant, P. Cool, *Applied Catalysis B: Environmental* **2009**, *88*, 515-524.

[14] M. Kosmulski, *Advances in Colloid and Interface Science* **2009**, *152*, 14-25.

[15] C. Baiocchi, M. C. Brussino, E. Pramauro, A. B. Prevot, L. Palmisano, G. Marcì, *International Journal of Mass Spectrometry* **2002**, *214*, 247-256.

[16] M. Stylidi, D. I. Kondarides, X. E. Verykios, *Applied Catalysis B: Environmental* **2003**, *40*, 271-286.

[17] aE. Moctezuma, E. Leyva, C. A. Aguilar, R. A. Luna, C. Montalvo, *Journal of Hazardous Materials* **2012**, *243*, 130-138; bL. Yang, L. E. Yu, M. B. Ray, *Environmental Science & Technology* **2009**, *43*, 460-465.

4 Shelled titania-based UV filters

From the results reported in Chapter 3, it is evident that *x*TiO_2@MSN systems are not suitable for any application in the cosmetic field as UV filters. The photocatalytic active phase can interact directly with the organic molecules, causing their degradation under UV irradiation. As described in this chapter, in order to avoid the photocatalytic activity, the mesoporous silica loaded with titania nanoparticles were covered with a non porous silica shell, as a physical barrier between the inner photocatalyst and the surrounding environment. For this study, on the bases of the results discussed in Chapter 3, we have chosen the sample with the lowest titania content (10TiO_2@MSN).

4.1 State of the art

Core/shell type nanoparticles are defined as materials constituted by an inner part (core) and an outer layer (shell), with the aim to overcoming several physico-chemical limitations such as low stability, high chemical reactivity, non-desired aggregation processes.[1] The typical approach for the synthesis of core/shell nanoparticles is usually "bottom-up" type, through the exploitation of the chemical properties of the molecules to cause them to self-assemble into some useful structures. The most used bottom-up strategies include chemical synthesis, chemical-vapour deposition, laser-induced assembly, self-assembly, colloidal aggregation, film deposition and growth.[2]

In material science and in chemistry, silica shell structures has been frequently studied to enhance the stability of colloidal systems (*i.e.* nanoscale metals, semiconductors, magnetic or ceramic nanoparticles).[3] They can confer steric and electrostatic protection on different core structures and they can act as dispersing agent of electrostatic colloids in a wide range of solvents.[4] Silica is used as coating material for several reasons, such as high stability, especially in aqueous media, chemical inertness, easy regulation of coating process, controlled porosity, optical transparency, possibility of subsequent functionalization and biocompatibility.[5] Moreover, the shell thickness can be tuned from few nanometers to hundreds of nanometers by controlling the experimental parameters (*i.e.* coating time, concentration of reactants, catalyst and other precursors).[6]

The classical process to coat colloidal nanoparticles with silica is the Stöber method,[7] which comprises the hydrolysis and the subsequent condensation of tetraethoxysilane (TEOS),

in solution with ethanol, water and ammonia. The most difficult challenge with this type of synthesis is to obtain the complete coverage of the core nanoparticles, avoiding the formation of core-free silica particles. According to the Stöber method, a direct coating is possible only on the surface of the nanoparticles with a significant chemical or electrostatical affinity for silica, like clay minerals,[8] hematite,[9] zirconia,[10] and titania.[11] The critical step is related to the transfer of colloids - stable only in aqueous solution - to an ethanol solution, to further grow the silica shell with the Stöber process.

Many papers report the coating of gold colloids nanoparticles. Since gold metal has very little affinity for silica, the silane coupling agents and the sodium silicate water-glass methods are widely utilized. For instance, Liz-Marzán *et al.*[12] reported a method to grow silica shell on gold colloids using (3-aminopropyl)triethoxysilane (APTES) as surface primer, followed by water-glass method and the further grow of silica shell through the Stöber method. The disadvantages of this method are that the growth of the initial shell with sodium silicate is strongly pH dependent, and the reaction requires from 24 hours to several weeks before a sufficiently thick shell can be formed. Nooney *et al.*[13] used (3-mercaptopropyl)trimethoxysilane (MPS) as a silane coupling agent, and water-glass method, followed by the classical Stöber method to cover 60-nm gold colloids with a mesoporous silica shell, with a total diameter from 150 to 450 nm. Correa-Duarte *et al.*[14] used the same methods to coat CdS semiconductor nanoparticles with a silica shell in order to reduce the photoactivity of the semiconductor.

Another method to prepare silica shell involves the use of polymers, whose ability to form aggregates in aqueous solution and their tendency to adsorb on different surfaces and interfaces can be exploited to coat nanoparticles with no affinity for silica. The most successful process using a polymer monolayer relies on the use of the polymer poly(vinylpyrrolidone) (PVP), as proposed by Graf *et al.*.[15] A development of this strategy concerns coating with silica after layer-by-layer (LbL) polyelectrolyte wrapping, with the alternating adsorption of positively and negatively charged polyelectrolytes. In order to favor the silica coating, the outermost layer is positively charged. The advantages of LbL method are the diversifying of the chemical composition, the control of the degree of the core surface coverage and the tunability of the shell thickness. Yuan *et al*.[16] used the LbL technique to coat particles of a organic pigment, Yellow 109, using the positively charged poly-(diallyldimethylammonium chloride) (PDADMAC) and the negatively charged poly-(sodium 4-styrenesulfonate) (PSS). Guerrero-Martìnez *et al*.[17] coated micron-sized zeolite L crystals through consecutive poly(allylamine hydrochloride) (PAH) and PVP adsorption. Ren *et al*.[18] exploited the LbL

technique to fabricate TiO_2@void@SiO_2 nanoparticles. The void space between the TiO_2 core and the silica shell can ensure the high photocatalytic activity of titania, releasing its active sites, while silica shell can prevent the photocatalytic property of TiO_2 nanoparticles from damaging any organic support.

The silica coating in water-in-oil microemulsions is another approach used for the coating of nanoparticles that are unstable in ethanol solution.[19] The main advantage of the reverse microemulsion method is the higher control over silica nucleation, limited to the interior of the nanometer-sized droplets.[20] Several parameters plays important roles in the shell formation.[21],[22],[23]

In this study, 10TiO_2@MSN surface was coated with a non-porous silica shell via the Stöber method, following the procedure described by Qu *et al*. with slightly modification.[24] Qu and co-workers loaded the MSN with particles of a fluorescent conjugated polymer, poly(p-phenylenevinylene) (PPV). Then, the MSN were coated with a first layer of non-porous silica and a second layer of mesoporous silica. Finally, the particles were loaded into the final layer with ibuprofen. With this method, silica shell of about 40 nm were obtained. Figure 1 shows the scheme of the Qu's synthesis.

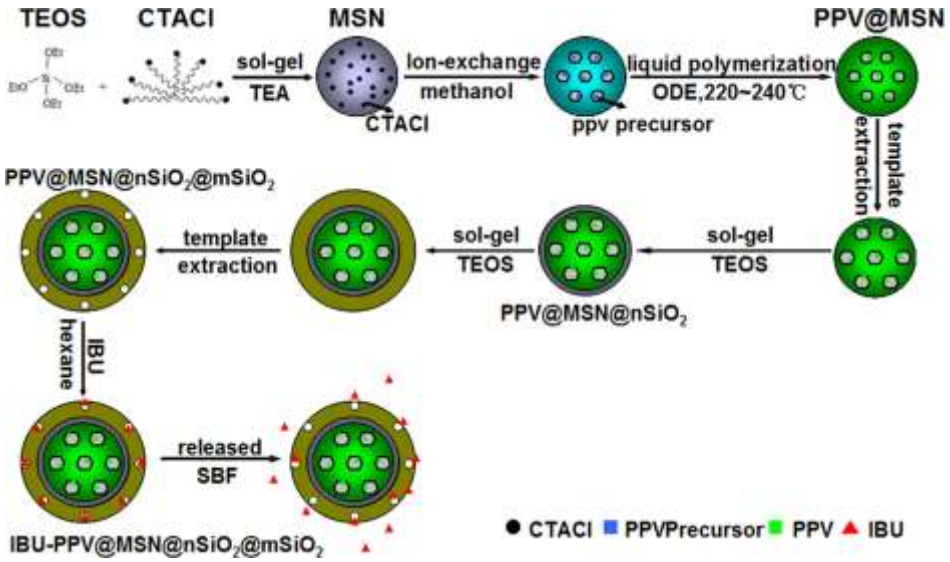

Figure 1 Synthetic procedure of silica coatings used by Qu and co-workers.

4.2 Samples preparation

Synthesis of shell on MSN loaded with TiO_2 nanoparticles ($10TiO_2$@MSN@S)

A non-porous silica shell is synthesized by Stöber method[24] on the surface of mesoporous silica nanoparticles loaded with $10\%_{wt}$ TiO_2 ($10TiO_2$@MSN, see paragraph 3.1).

In order to tune the shells thickness, the samples were prepared varying the reactant molar ratios and the reaction conditions, as summarized in Table 1.

$10TiO_2$@MSN sample was added to a solution of EtOH, H_2O and NH_3 and the mixture was sonicated for 10 minutes to promote a fine dispersion. Then, TEOS was added dropwise in the solution, keeping a vigorous stirring for 6 hours at room temperature. The solvents mixture was removed via centrifugation (6000 rpm/10 minutes). The recovered solid was purified by repeated centrifugation (three times), ethanol washing and sonication (15 min). Finally, the solid was dried at 60 °C overnight and labelled as $10TiO_2$@MSN@S*x*, where *x* represents the obtained shell thickness labelled with a letter.

Table 1 Reaction conditions of the $10TiO_2$@MSN@S*x* samples. The aliquots are referred to 100 mg of $10TiO_2$@MSN.

Sample	EtOH (mL)	H_2O (mL)	NH_3 (mL)	TEOS (g)	time (h)
$10TiO_2$@MSN@S*a*	80	20	1	0.100	6
$10TiO_2$@MSN@S*b*	80	20	2.5	0.250	6
$10TiO_2$@MSN@S*c*	80	20	10	1.000	6
$10TiO_2$@MSN@S*d*	800	20	10	1.000	1
$10TiO_2$@MSN@S*e*	800	200	10	1.000	6
$10TiO_2$@MSN@S*f*	400	100	5	0.500	6
$10TiO_2$@MSN@S*g*	200	50	2.5	0.250	6
$10TiO_2$@MSN@S*h*	400	100	10	1.000	6

4.3 Results and discussion

In order to verify the formation of the silica coating on the MSN surface and to evaluate the influence of the experimental conditions on thickness and homogeneity, a detailed TEM analysis was performed. From the observations of all the $10TiO_2$@MSN@S*x* samples, homogeneous shells that cover uniformly the MSN surface can be detected, while the presence of new non-porous silica particles are not revealed. This result shows that, with the adopted synthetic procedure, TEOS prefers to condense around the MSN, rather than form new silica particles. For the $10TiO_2$@MSN@S*a*/*b*/*c* samples, the $10TiO_2$@MSN concentration and the reaction time (6 hours) were kept constant and the TEOS concentration was varied. The shell thickness, ranged between 8±1 and 171±8 nm (Figure 2 and Figure 3), was measured from TEM observations.

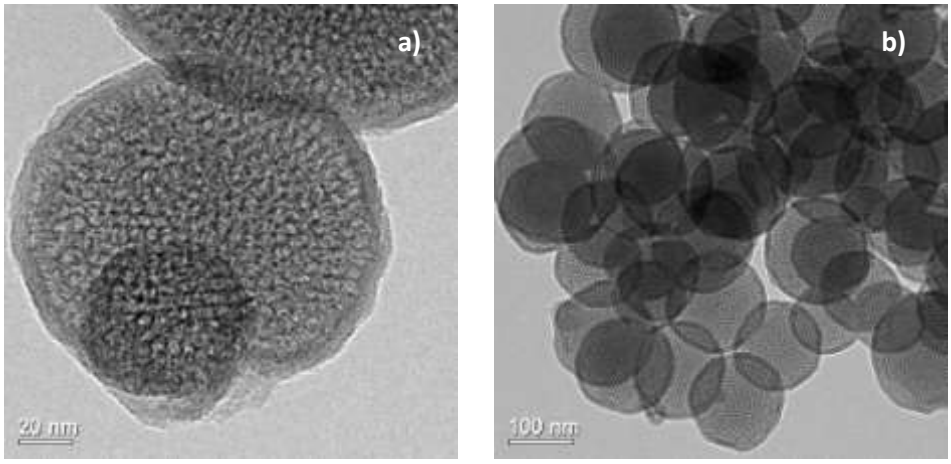

Figure 2 TEM micrographs of the TiO_2@MSN@S*a* specimen, shell thickness of ~8 nm.

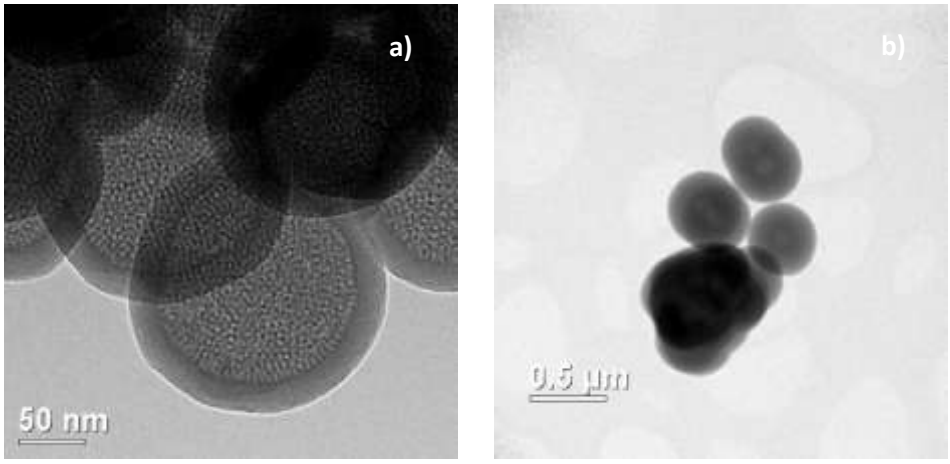

Figure 3 TEM micrographs of $10TiO_2$@MSN@S*b* with a shell thickness of ~23 nm (a) and $10TiO_2$@MSN@S*c* with a shell thickness of ~171 nm (b).

The influence of the reaction time on the shell formation was also tested, comparing the TiO_2@MSN@S*c* and 10TiO_2@MSN@S*d* samples. For these samples the synthesis was conducted for 1 and 6 hours, respectively. The TEM micrographs reported in Figure 4, evidence that the complete covering of MSN surface already after 1 hour, even if the shells are inhomogeneous. In fact, some particles result to be coated with thickness of about 190 nm – very close to the values obtained for TiO_2@MSN@S*c* sample- while other ones have a smaller thickness of about 20 nm.

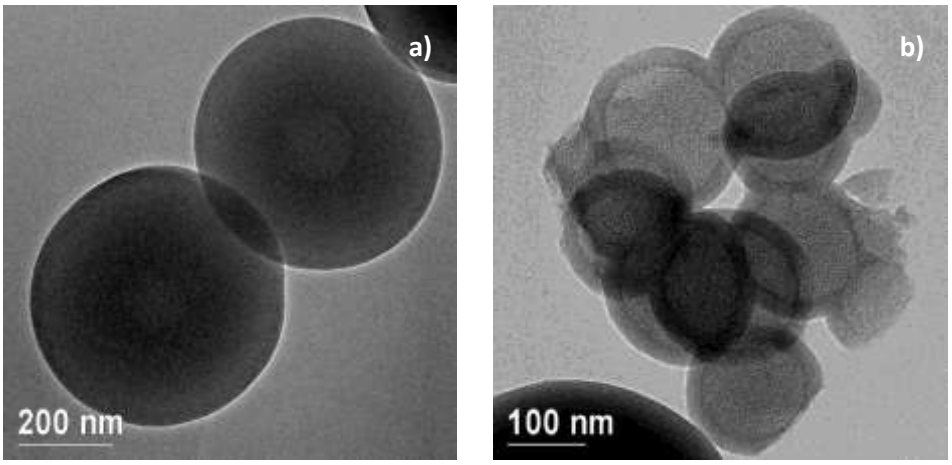

Figure 4 TEM micrographs of the 10TiO_2@MSN@S*d* (shell thickness of ~193 nm).

Furthermore, the influence of the 10TiO_2@MSN concentration on the shell thickness was checked, keeping constant TEOS concentration at 1 g/L. The TEM micrographs for the 10TiO_2@MSN@S*a*/S*e*/S*f* samples show that all the specimens have homogeneous shells, with a thickness ranging from 14±4 to 16±2 nm (Figure 5, Figure 6 and Figure 7).

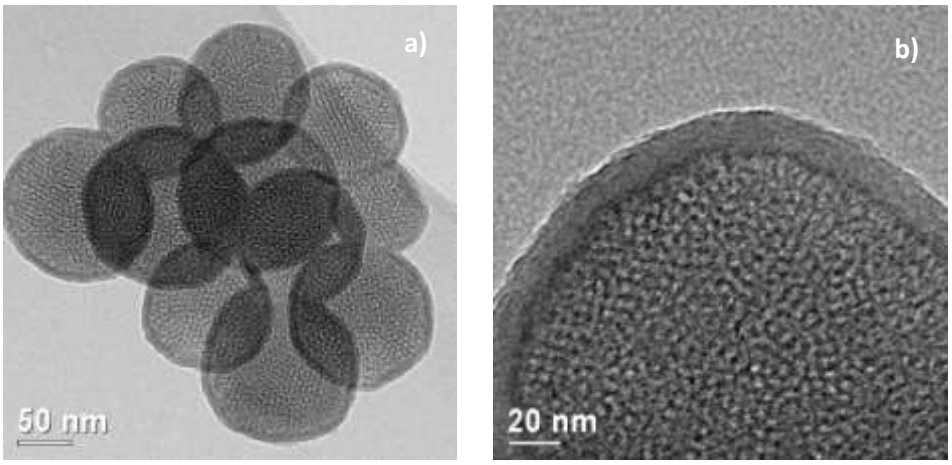

Figure 5 TEM micrographs of the 10TiO_2@MSN@S*e* (shell thickness of ~14 nm).

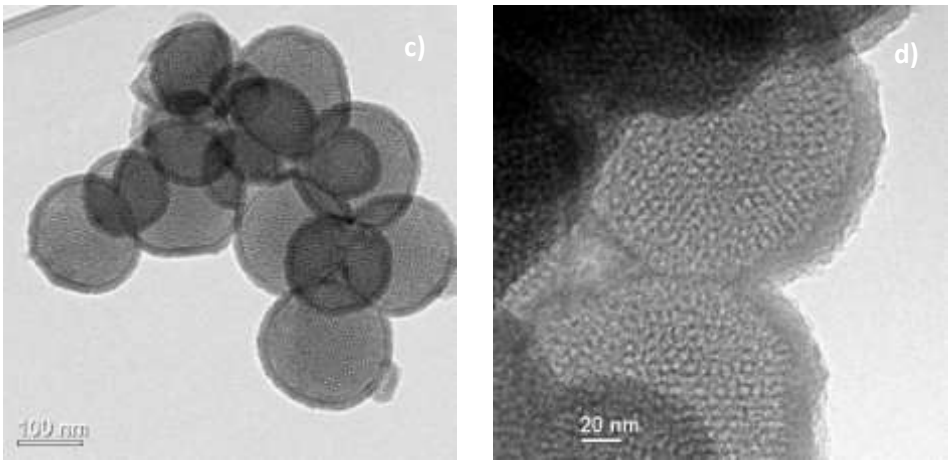

Figure 6 TEM micrographs of the 10TiO_2@MSN@S*f* specimen (shell thickness of ~15 nm).

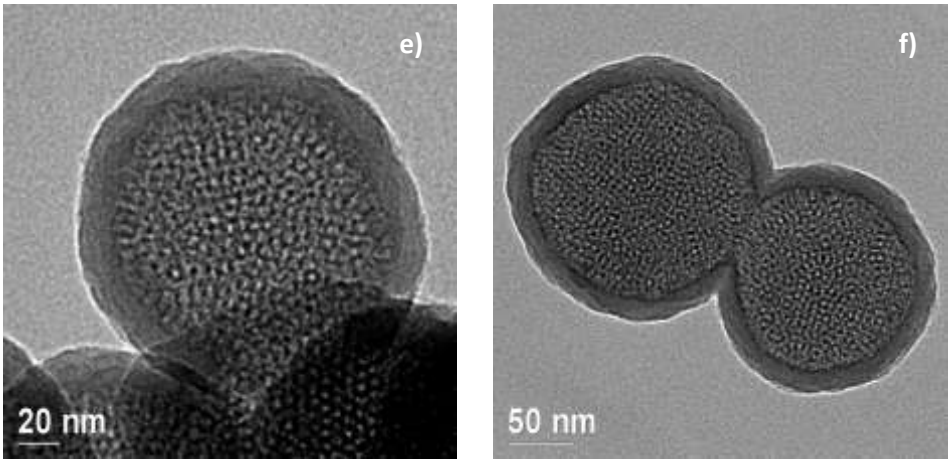

Figure 7 TEM micrographs of the 10TiO_2@MSN@S*g* specimen (shell thickness of ~16 nm).

Finally, the 10TiO_2@MSN@S*h* sample, prepared with a double concentration of TEOS (2 g/L) with respect to 10TiO_2@MSN@S*f*, show a shell of 60±2 nm (Figure 8).

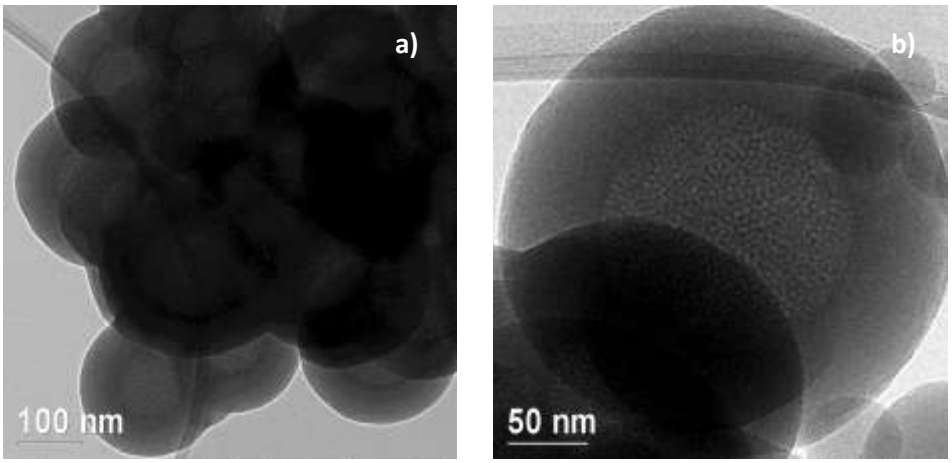

Figure 8 TEM micrographs of the $10TiO_2$@MSN@S*h* specimen (shell thickness of ~60 nm).

Table 2 summarizes the shell thickness measured from TEM micrographs, in function of $10TiO_2$@MSN, TEOS concentration and reaction time.

Table 2 $10TiO_2$@MSN concentration (g/L), TEOS concentration (g/L), reaction time (h) and shell thickness (nm) for $10TiO_2$@MSN@S*x* samples.

Sample	[$10TiO_2$@MSN] (g/L)	[TEOS] (g/L)	Reaction time (h)	Shell thickness (nm)
$10TiO_2$@MSN@S*a*	1	1	6	8±1
$10TiO_2$@MSN@S*b*	1	2.5	6	23±2
$10TiO_2$@MSN@S*c*	1	10	6	171±8
$10TiO_2$@MSN@S*d*	1	10	1	20±3 /193±10
$10TiO_2$@MSN@S*e*	0.1	1	6	14±4
$10TiO_2$@MSN@S*f*	0.2	1	6	15±2
$10TiO_2$@MSN@S*g*	0.4	1	6	16±2
$10TiO_2$@MSN@S*h*	0.2	2	6	60±2

From these results, in order to have a comprehensive knowledge of the role of the precursor, it is possible draw a plot of the shell thickness versus the TEOS concentration for the

10TiO_2@MSN@S*a*/S*b*/S*c* samples. Figure 9 displays a linear trend, according to which the higher the concentration the greater the thickness of the silica coating.

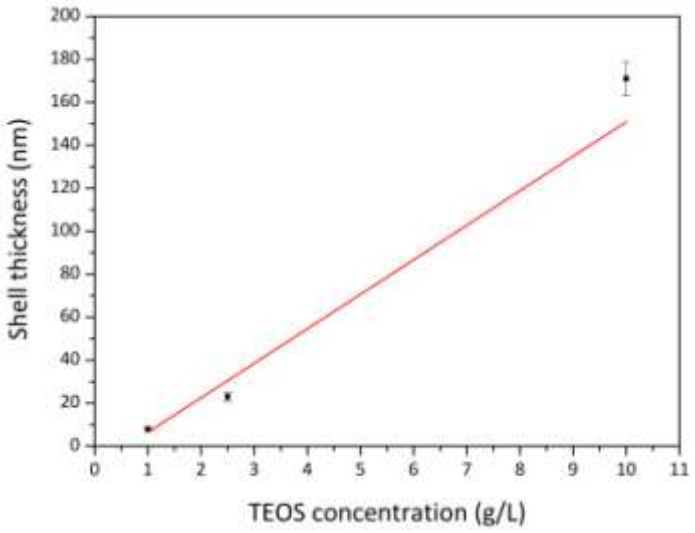

Figure 9 Shell thickness in function of TEOS concentration, with a constant 10TiO_2@MSN concentration of 1 g/L. The line is a guide to the eye.

Conversely, the 10TiO_2@MSN concentration does not influence the shell formation and a general trend can not be identified as display in Figure 10.

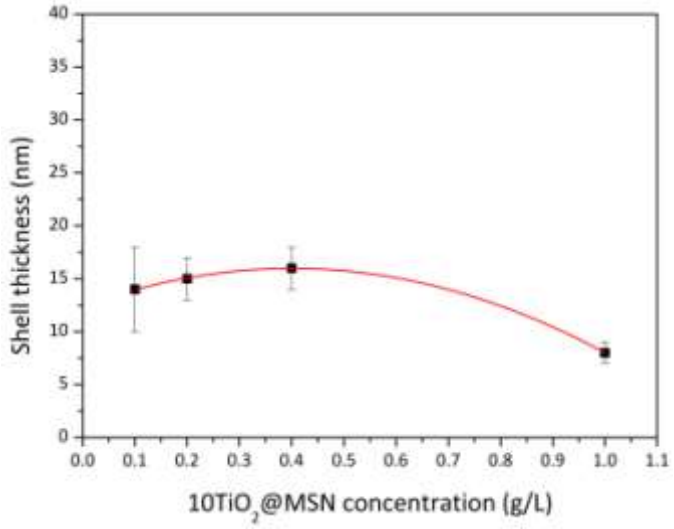

Figure 10 Shell thickness in function of 10TiO_2@MSN concentration, with a constant TEOS concentration of 1 g/L. The line is a guide to the eye.

To corroborate TEM analysis and in order to understand the effect and the behavior of the MSN coating, porosity analysis were performed through N_2 adsorption/desorption

measurements. The TiO_2@MSN@S*a*/S*b*/S*c* samples are compared with the 10TiO_2@MSN sample (Figure 11a). As previously discussed in paragraph 3.2, the N_2 adsorption/desorption isothermal curves of 10TiO_2@MSN featured the typical shape of a mesoporous material. When 10TiO_2@MSN composite is covered with the silica shell, this characteristic profile is progressively lost as the coating thickness increases. In fact, the greater the thickness, the lower the capacity of the nitrogen molecules to penetrate inside the mesoporous matrix. Consequently, the specific surface area decreases with the shell thickness increasing (see Table 3). Also the pore volume available, drastically decrease at the increasing of the shell thickness, as obtained from the BJH pore distribution (Figure 11b).

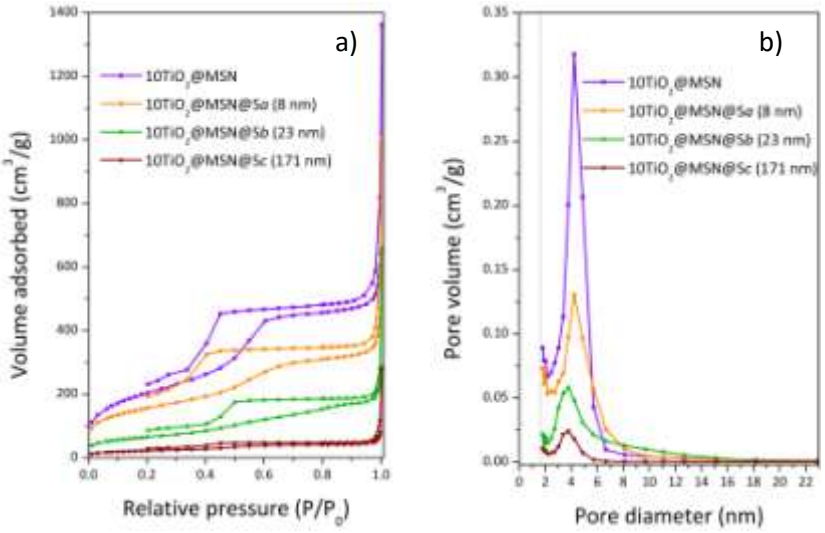

Figure 11 N_2 adsorption/desorption isotherm (a) and pore size distribution (b) of 10TiO_2@MSN, 10TiO_2@MSN@S*a*, 10TiO_2@MSN@S*b* and 10TiO_2@MSN@S*c* samples.

Figure 12 reports the N_2 adsorption/desorption isotherms for the 10TiO_2@MSN@S*a*/S*e*/S*f*/S*g* samples in which TEOS concentration (1g/L) and the reaction time (6 h) were kept constant, varying only the 10TiO_2@MSN concentration (from 0.1 to 1 g/L). Notwithstanding these nanocomposites present a similar shell thickness (see

Table 3), as revealed from TEM investigations, the relative isothermal curves display slight differences. Taking 10TiO_2@MSN sample as reference, the general trend show a decrease of the specific surface area values and of the pore volume, even if they do not occur in an expected sequence. This is probably due to some unrevealed inhomogeneity of the coating. The lowest values of specific surface area and pore volume correspond to the sample with the minor 10TiO_2@MSN concentration (10TiO_2@MSN@S*e*).

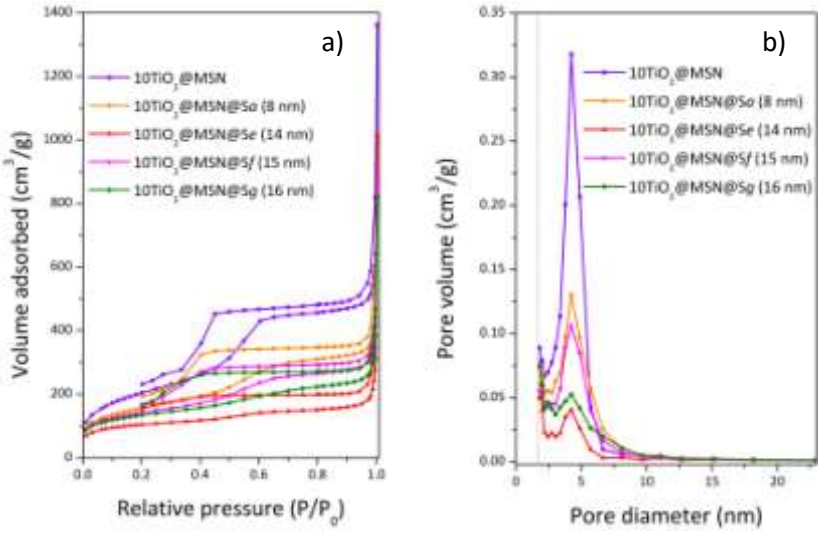

Figure 12 N_2 adsorption/desorption isotherm (a) and pore size distribution (b) of $10TiO_2$@MSN and TiO_2@MSN@S*e*/S*f*/S*g* samples.

Table 3 Physicochemical parameters derived from nitrogen physisorption of $10TiO_2$@MSN and $10TiO_2$@MSN@S*x* samples. [a] Specific surface area (S.A.). [b] Mean pore size (D_p). [c] Total pore volume (V_p).

Sample	S.A.[a] (m^2/g)	D_p[b] (nm)	V_p[c] (cm^3/g)
$10TiO_2$@MSN	737	0.8	4.2
$10TiO_2$@MSN@S*a*	541	0.6	4.2
$10TiO_2$@MSN@S*b*	230	0.3	3.8
$10TiO_2$@MSN@S*c*	76	0.1	3.8
$10TiO_2$@MSN@S*d*	157	0.1	4.2
$10TiO_2$@MSN@S*e*	342	0.3	4.2
$10TiO_2$@MSN@S*f*	498	0.5	4.2
$10TiO_2$@MSN@S*g*	467	0.4	4.2
$10TiO_2$@MSN@S*h*	316	0.2	3.8

After the studies about the tunability of the shell thickness, we can conclude that:

(i) the synthetic procedure allows to obtain a smooth and homogenous non-porous silica coating;

(ii) the TEOS concentration, ranging from 1 to 10 g/L, strongly influences the shell thickness, which varies from 8±1 to 171±8 nm;

(iii) the $10TiO_2$@MSN concentration, ranging from 0.1 to 1 g/L, does not seem to influence the shell thickness, comprised from 8 to 16 nm.

To determine the UV-vis properties and the photocatalytic activity, three shelled nanocomposites, $10TiO_2$@MSN@S*a*/S*b*/S*h*, were selected as representative samples with small (8 nm), medium (23 nm) and large (60 nm) shell thickness, respectively.

The diffusive reflectance UV-vis spectra of the samples were compared to $10TiO_2$@MSN sample as reference. The Kubelka-Munk functions and the band gap energy values with the correspondent absorption edges are reported in Figure 13 and in Table 4, respectively.

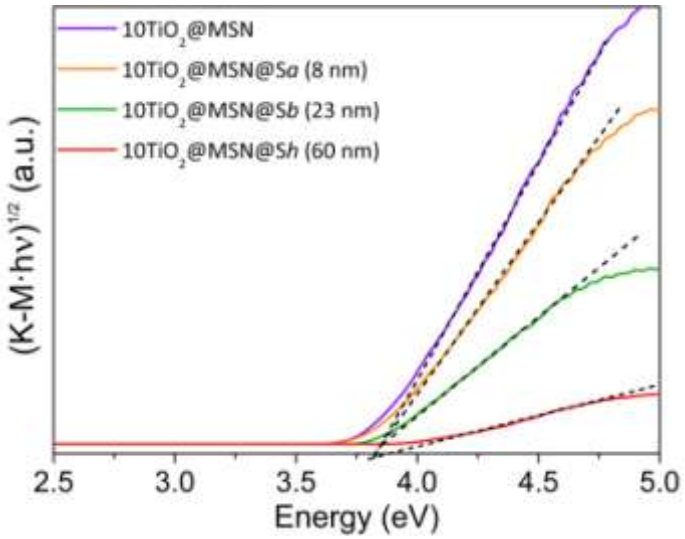

Figure 13 Kubelka-Munk function *vS* Energy of $10TiO_2$@MSN and $10TiO_2$@MSN@S*a*/S*b*/S*h* samples.

As shown in Table 4, the extrapolated E_g values of all the shelled samples ($10TiO_2$@MSN@S*a*; $10TiO_2$@MSN@S*b*; $10TiO_2$@MSN@S*h*) are equal to 3.8 eV, as found for the $10TiO_2$@MSN sample, with an adsorption edge of 322 nm. As expected, the obtained data lead to conclude that the silica coating does not affect the UV-vis properties of the nanocomposites.

Table 4 Band gap energy values of $10TiO_2$@MSN and $10TiO_2$@MSN@S*x* samples.

Sample	Energy gap (eV)	Absorption edge (nm)
$10TiO_2$@MSN	3.8	380
$10TiO_2$@MSN@S*a*	3.8	322
$30TiO_2$@MSN@S*b*	3.8	322
$40TiO_2$@MSN@S*h*	3.8	313

Photocatalytic activity

The photocatalytic activity of $10TiO_2$@MSN@S*a* (8 nm), $10TiO_2$@MSN@S*b* (23 nm) and $10TiO_2$@MSN@S*h* (60 nm) samples were tested monitoring the degradation of MO under UV-vis irradiation (Figure 14).

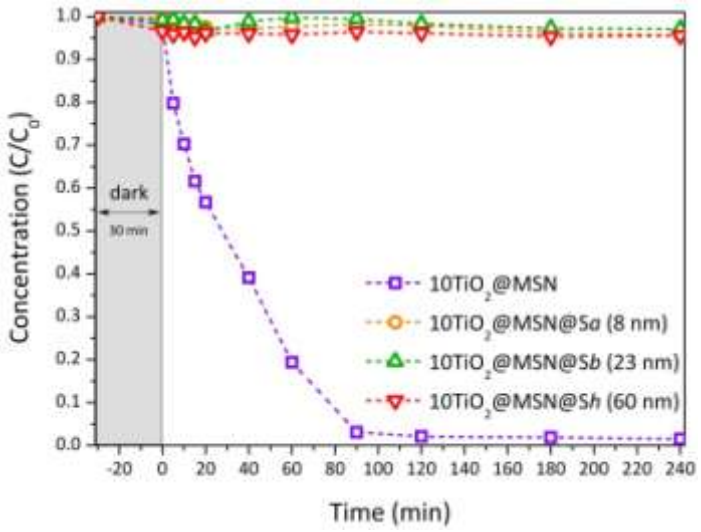

Figure 14 Performances of adsorption and MO photodegradation on $10TiO_2$@MSN and $10TiO_2$@MSN@S*a*/S*b*/S*h* samples under UV irradiation.

During the 30 min of equilibration in the dark, the adsorption of MO on the particle surface is negligible and, after 240 min of UV rays irradiation, the organic dye is not degraded. This confirms the results of the TEM analysis (Figure 2, Figure 3 and Figure 8): the coatings are

homogeneous and cover all the surface of the $10TiO_2$@MSN. The non-porous silica shells act as physical barriers between the external environment and the inner thus preventing the dye to penetrate into the MSN and to reach the photocatalyst placed inside. This is true already also for the sample with the most thin shell ($10TiO_2$@MSN@S*a* sample, 8 nm).

The appearance of new absorption bands is not observed, indicating that degradation of MO and of its aromatic by-products are fast during the photocatalytic irradiation.

4.3 Conclusions

In summary, shelled mesoporous silica nanospheres loaded with 10 wt% TiO_2 nanoparticles were synthesized. The $10TiO_2$@MSN surface was coated with a non-porous silica shell via the Stöber method, obtaining a series of samples. The coating on $10TiO_2$@MSN is direct, thanks to the obvious affinity between the same type of material, and the stability of the system in ethanolic solution. The samples were synthesized varying some experimental parameters (different reactant molar ratios and reaction conditions). TEM analysis reveals that the shell thickness range from 8±1 to 193±10 nm and it is correlated to TEOS concentration, while the homogeneity of the shell depends on the reaction time. From the photocatalytic tests, it is emerged that the non porous silica shell act as a physical barrier for the outer environment, avoiding the interaction between the photocatalyst and the external organic matrixes. Moreover, the silica shell does not influenced the UV properties of $10TiO_2$@MSN@S*x* composites.

References

[1] A. Guerrero-Martinez, J. Pérez-Juste, L. M. Liz-Marzán, *Advanced Materials* **2010**, *22*, 1182-1195.

[2] aO. Sneh, R. B. Clark-Phelps, A. R. Londergan, J. Winkler, T. E. Seidel, *Thin Solid Films* **2002**, *402*, 248-261; bY. Y. Wang, K. F. Cai, X. Yao, *Journal of Solid State Chemistry* **2009**, *182*, 3383-3386; cS.-H. Yoo, L. Liu, S. Park, *Journal of Colloid and Interface Science* **2009**, *339*, 183-186.

[3] aH. S. Nalwa, in *Handbook of Surfaces and Interfaces of Materials* (Ed.: H. S. Nalwa), Academic Press, Burlington, **2001**, pp. xxv-xxviii; bL. M. Liz-Marzán, P. Mulvaney, *The Journal of Physical Chemistry B* **2003**, *107*, 7312-7326.

[4] F. Kuspert, *Berichte* **1919**, *35*, 2815.

[5] D. Knopp, D. Tang, R. Niessner, *Analytica Chimica Acta* **2009**, *647*, 14-30.

[6] R. G. Chaudhuri, S. Paria, *Chemical Reviews* **2012**, *112*, 2373-2433.

[7] W. Stöber, A. Fink, E. Bohn, *Journal of Colloid and Interface Science* **1968**, *62*, 62.

[8] R. K. Iler, *U. S. Patent No. 2,885,366* **1959**.

[9] M. Ohmori, E. Matijević, *Journal of Colloid and Interface Science* **1992**, *150*, 594.

[10] J. N. Ryan, M. Elimelech, J. L. Baeseman, R. D. Magelky, *Environmental Science & Technology* **2000**, *34*, 2000.

[11] A. Jaroenworaluck, W. Sunsaneeyametha, N. Kosachan, R. Stevens, *Surface and Interface Analysis* **2006**, *38*, 473-477.

[12] L. M. Liz-Marzán, M. Giersig, P. Mulvaney, *Langmuir* **1996**, *12*, 4329-4335.

[13] R. I. Nooney, T. Dhanasekaran, Y. Chen, R. Josephs, A. E. Ostafin, *Advanced Materials* **2002**, *14*, 529-532.

[14] M. A. Correa-Duarte, M. Giersig, L. M. Liz-Marzán, *Chemical Physics Letters* **1998**, *286*, 497-501.

[15] C. Graf, D. L. J. Vossen, A. Imhof, A. Van Blaaderen, *Langmuir* **2003**, *19*, 6693-6700.

[16] J. Yuan, S. Zhou, B. You, L. Wu, *Chemistry of Materials* **2005**, *17*, 3587-3594.

[17] A. Guerrero-Martinez, S. Fibikar, I. Pastoriza-Santos, L. M. Liz-Marzán, L. De Cola, *Angewandte Chemie International Edition* **2009**, *48*, 1266-1270.

[18] Y. Ren, M. Chen, Y. Zhang, L. Wu, *Langmuir* **2010**, *26*, 11391-11396.

[19] aM. Li, H. Schnablegger, S. Mann, *Nature* **1999**, *402*, 393-395; bB. Jonsson, B. Lindman, K. Holmberg, B. Kronberg, *Surfactants and polymers in aqueous solution* **1998**.

[20] Y. Han, J. Jiang, S. S. Lee, J. Y. Ying, *Langmuir* **2008**, *24*, 5842-5848.

[21] C. Petit, P. Lixon, M. P. Pileni, *Journal of Physical Chemistry* **1993**, *97*, 12974.

[22] M. P. Pileni, *Langmuir* **1997**, *13*, 3266.

[23] I. Lisiecki, M. P. Pileni, *Journal of Physical Chemistry* **1995**, *99*, 5077.

[24] Y. Qu, L. Feng, C. Tong, B. Liu, C. Lü, *Microporous and Mesoporous Materials* **2013**, *182*, 155-164.

5 Bismuth titanate-based UV filters

As shown in Chapter 3, the *x*TiO_2@MSN systems can not be used as UV filters due to their high photocatalytic activity. To avoid the direct contact between TiO_2 and the surrounding environment, the 10TiO_2@MSN nanoparticles were coated with a nonporous silica to form the 10TiO_2@MSN@S*x* systems, as widely discussed in Chapter 4. These new samples show excellent results with an evident reduction of the photocatalytic properties and the presence of the silica layer does not shields the UV properties.

In order to synthesize an inorganic UV filter with a broader screening in the UV region a new strategy is described in this chapter. With this aim, the addition of a bismuth salt to the 10TiO_2@MSN system has been investigated to obtain the growth of bismuth titanate ($Bi_xTi_yO_z$) nanoparticles into MSN matrix. The role of the precursor content and of the annealing temperature are explored both on the UV properties and on the photocatalytic properties.

5.1 State of art

In the last decade, the chemical potential of bismuth and bismuth compounds has been actively explored. In particular, bismuth compounds have attracted great attention thanks to their suitable properties in a wide variety of applications like gas sensing,[1] photocatalysis,[2] solid oxide fuel cells (SOFS)[3] or in the field of medicine[4] and topological insulators.[5] Moreover, they are rather inexpensive and characterized by a low toxicity[6] attracting the interest of the scientific community as suitable reagents for large-scale synthesis, (*i.e.* as active pharmaceutical ingredients). Among the huge group of Bi-compounds, bismuth titanates family has been actively exploited in the field of microelectronics, electro-optics, dielectric, as well as in visible-light photocatalysis.[7] Theoretical and experimental studies were aimed to a deep comprehension of the structural[8] and photocatalytic[9] properties of the different $Bi_xTi_yO_z$ phases. For instance, the sillenite $Bi_4Ti_3O_{12}$ phase is a well-known candidate for high-temperature device applications due to its high dielectric constant, breakdown strength and anisotropy, and low dielectric dissipation factor.[10] The dielectric pyrochlore $Bi_2Ti_2O_7$ phase is used in photocatalysis, from the solar hydrogen production by water splitting[41] to the

degradation of organic compounds under sunlight irradiation.[11] Also its insulating properties, as oxide material in MOS (metal oxide semiconductor) devices, have been evaluated.[12]

When bismuth compounds are synthesized in presence of Si or SiO_2, bismuth silicate Bi_2SiO_5 can be formed.[13] Bismuth silicate has been reported as a promising material with relatively good dielectric properties and piezoelectric and nonlinear optical effects, as well as luminescent properties.[14] Moreover, its photocatalytic activity is well demonstrated in many works.[15]

In this chapter, we propose a new UV filter system based on bismuth titanates ($Bi_xTi_yO_z$), loaded into MSN, with high UV shielding properties and no photocatalytic activity. For the best of our knowledge, up to now, no literature about this system applied to cosmetic has been never reported.

5.2 Samples preparation

The role of the Bi content and of the annealing temperature both on the UV properties and on the photocatalytic properties have been evaluated.

The synthesis of $Bi_xTi_yO_z$ nanoparticles into the mesopores of silica matrix was conducted by incipient wetness impregnation at room temperature in two steps. In our typical synthetic procedure, the first step was carried out loading titanium dioxide nanoparticles into mesoporous silica ($10TiO_2$@MSN), as described in paragraph 3.1.[16] In the second step, $Bi(NO_3)_3 \cdot 5H_2O$ was dissolved in a $EtOH/HNO_3$ solution (5:1, 25 mL) and then added to the $10TiO_2$@MSN sample (0.3 g), keeping the dispersion under stirring for 1 h. The powders were recovered through the removal of the solvent by means of a rotary evaporator and calcined at 800°C, with a heating rate of 1°C min^{-1}, for 2 h.

For the study of the role of bismuth concentration, the calcination temperature was kept constant at 800°C and the samples are referred as *x*Bi/Ti@MSN_800, where x represents the different Bi/Ti molar ratio (*x* = 0.25, 0.50, 1.25 and 2.50).

For the study of the role of the thermal treatment, the Bi/Ti molar ratio was kept constant at 1.15 and the samples are labeled as 1.15Bi/Ti@MSN_*y*, where *y* represents the annealing temperature (*y* = 500, 600, 700, 750 and 800°C).

5.3 Study of the role of bismuth concentration

5.3.1 Results and discussion

The presence of chemical bonds involving Bi ions was checked by DRIFT IR spectroscopy analysis. (Figure 1). As detected by Ren et al.,[17] a peak at 861 cm^{-1} due to the vibration of Bi-O-Bi is revealed. Figure 1b show the presence of this characteristic peak only in the sample with the highest bismuth amount (2.50Bi/Ti@MSN_800). This finding could be related to the bismuth content, that, in the other samples of the *x*Bi/Ti@MSN_800 series, it is not enough to be revealed. As an example, Figure 1 reports the 1.15Bi/Ti@MSN_800 and 2.50Bi/Ti@MSN_800 spectra.

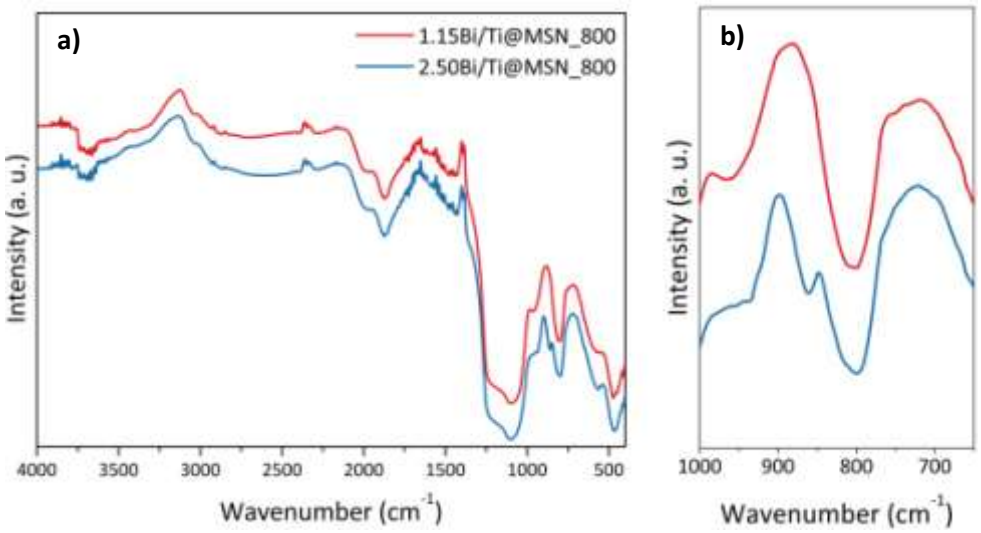

Figure 1 DRIFT-IR spectra of 1.15Bi/Ti@MSN_800 and 2.50Bi/Ti@MSN_800 samples: full spectrum (a) and magnification in the 1000 and 650 cm^{-1} range.

The role of Bi/Ti molar ratio on the formation of crystalline phases was checked by XRPD analysis (Figure 3).

The low angle region (Figure 2) of the xBi/Ti@MSN_800 samples show that, when the Bi/Ti molar ratio increases, the ordered hexagonal mesoporous structure of silica matrix is not more retained. In particular, a significant decrease of the order occurs already at the minimum bismuth content, up to the completely loss for higher concentrations. This behavior can be due to a high degree of disorder of the pores or to a complete collapse of the silica network, in

which bismuth ions play an active role. These findings are consistent also with the TEM analysis (see Figure 6, Figure 7 and Figure 8) discussed at pages 86 and 87.

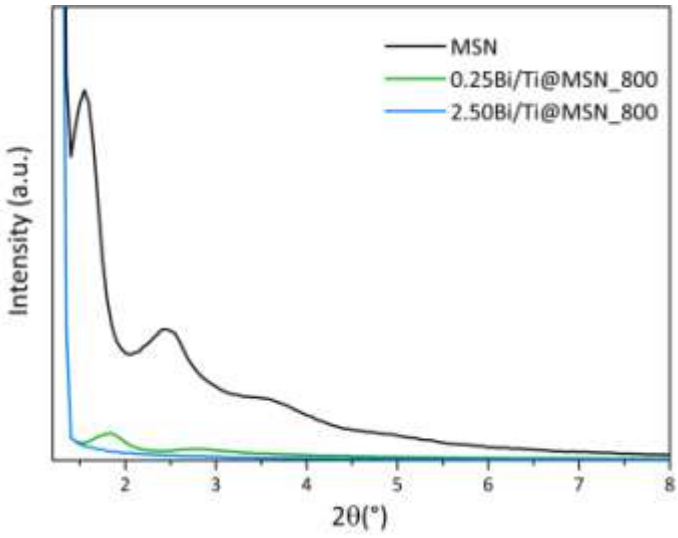

Figure 2 XRD spectra of MSN, 0.25Bi/Ti@MSN_800 and 2.50Bi/Ti@MSN_800 samples in the small-angle region.

In the range between 25° and 35°, reported in Figure 3b, it is evident that at the lowest Bi contents (0.25 and 0.50 Bi/Ti molar ratio), $Bi_2Ti_2O_7$ is the only crystalline phase formed. Increasing the bismuth concentration (1.15 Bi/Ti molar ratio), $Bi_2Ti_2O_7$ content is maximum and bismuth silicate Bi_2SiO_5 starts to grow. At the maximum amount of bismuth (2.50 molar/ratio), Bi_2SiO_5 crystalline phase grows at the expense of the $Bi_2Ti_2O_7$. Moreover, another crystalline phase of bismuth titanate forms, $Bi_4Ti_3O_{12}$, favored by the stoichiometric ratio.

From the XRD patterns of the *x*Bi/Ti@MSN_800 series it could be conclude that:

(i) at the lowest bismuth/titanium molar ratio (0.25 and 0.50), bismuth salt reacts with titanium, forming $Bi_2Ti_2O_7$;

(ii) when the bismuth content increases (1.15Bi/Ti@MSN_800), all the $Bi_2Ti_2O_7$ forms and the excess of bismuth starts to react with silica matrix with the formation of a small amount of Bi_2SiO_5;

(iii) at the maximum bismuth/titanium molar ratio (2.50), the bismuth excess reacts with silica and forms a consistent amount of bismuth silicate.

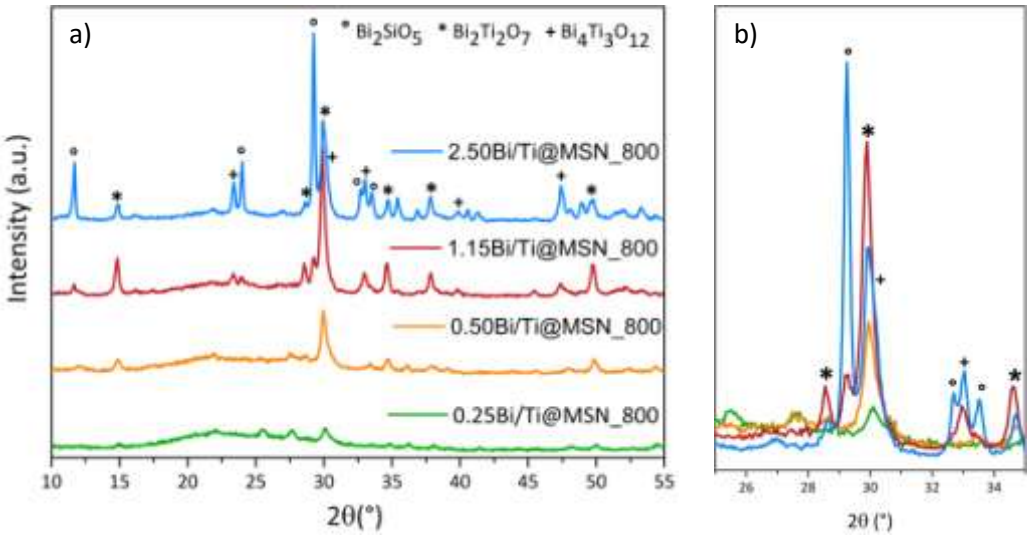

Figure 3 XRD spectra of the *x*Bi/Ti@MSN_800 series: full spectrum (a) and zoom between 25° and 35° (b).

The crystallites size of $Bi_2Ti_2O_7$, $Bi_4Ti_3O_{12}$ and Bi_2SiO_5 were determined by the Sherrer equation from the Rietveld refinements. The obtained values are referred only for the 1.15Bi/Ti@MSN_800 and 2.50Bi/Ti@MSN_800, since in the spectra of the other samples it was not possible to distinguish in a precise way the peaks of the different phases. In Figure 4 the Rietveld refinement of 2.50Bi/Ti@MSN_800 is reported as example.

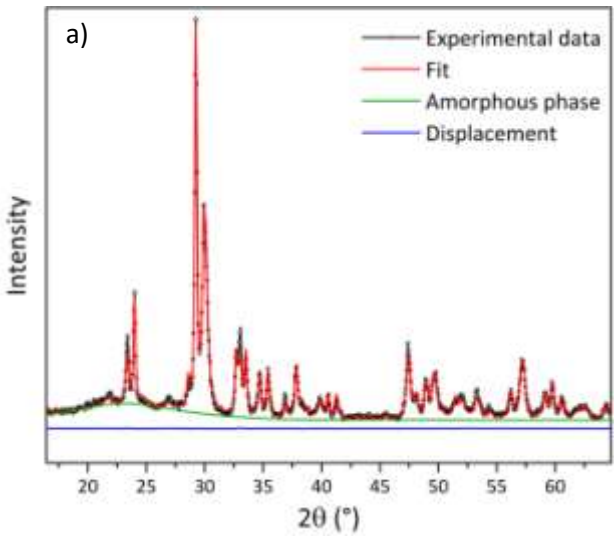

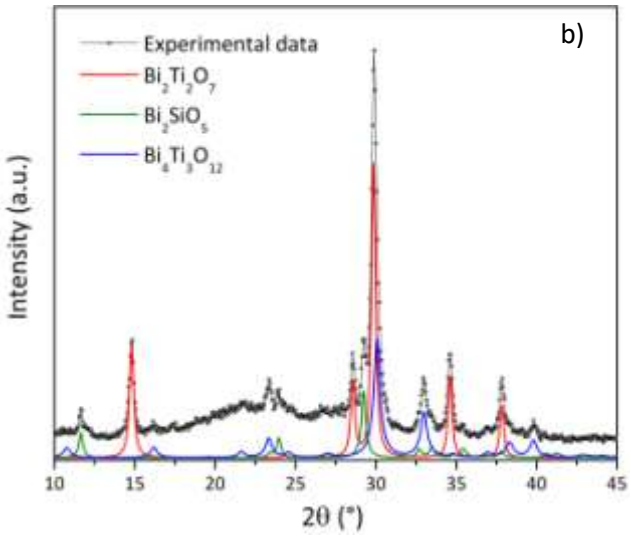

Figure 4 Rietveld refinement XRPD pattern (a) and phase contributions in XRPD pattern (b) of 2.50Bi/Ti@MSN_800 sample.

The volumetric average crystallites size both of 1.15Bi/Ti@MSN_800 and 2.50Bi/Ti@MSN_800 are reported in Table 1. From the results, it is evident that at the highest Bi/Ti molar ratio, the Bi_2SiO_5 crystallites grow significantly, as confirmed also by TEM analysis (see Figure 8).

Table 1 XRPD measurements of Bi_2SiO_5, $Bi_2Ti_2O_7$ and $Bi_4Ti_3O_{12}$ crystallite sizes obtained from Rietveld refinements for 1.15Bi/Ti@MSN_800 and 2.50Bi/Ti@MSN_800 samples

Sample	Crystalline phase (nm)		
	Bi_2SiO_5	$Bi_2Ti_2O_7$	$Bi_4Ti_3O_{12}$
1.15 Bi/Ti@MSN_800	29	21	15
2.50Bi/Ti@MSN_800	56	20	15

Quantitative determinations of Ti and Bi were conducted by SF-ICP-MS measurements. In Table 2, SF-ICP-MS data are reported considering the wt% crystalline phases SiO_2, TiO_2 and Bi_2O_3 and comparing them with the theoretical calculations and with XRPD determinations. The values evidence that the bismuth and titanium contents are less than the expected amount determines by theoretical calculation. As it will be discussed in detail at pag. 93 for the 1.15Bi/Ti@MSN_*y* series (see Table 6), the loss of bismuth is not affected by the thermal

treatment, as one might have assumed considering the volatility of bismuth at high temperature, but it probably occurs during the impregnation step. The same conclusion can be reached also in the case of titanium. SF-ICP-MS and XRPD values are not in good agreement for 2.50Bi/Ti@MSN_800 sample, probably because this sample is particularly heterogeneous, as revealed by TEM observations (see pag. 87).

Table 2 Quantitative determination (wt%) of SiO_2, Bi_2O_3 and TiO_2 phase contributions in *x*Bi/Ti@MSN_800.

Sample	Crystalline phase	Theoretical (%)	SF-ICP-MS (%)	XRPD (%)
0.25Bi/Ti@MSN_800	SiO_2	83.85	87.00	
	TiO_2	9.32	8.64	
	Bi_2O_3	6.83	4.36	
0.50Bi/Ti@MSN_800	SiO_2	79.41	83.06	
	TiO_2	8.82	8.40	
	Bi_2O_3	11.76	8.54	
1.15Bi/Ti@MSN_800	SiO_2	66.18	75.43	78.20
	TiO_2	7.35	6.53	4.80
	Bi_2O_3	26.47	18.00	17.00
2.50Bi/Ti@MSN_800	SiO_2	51.92	59.21	71.19
	TiO_2	5.77	4.04	4.81
	Bi_2O_3	42.31	36.75	24.00

In order to evaluate the influence of bismuth on the system, adsorption-desorption isotherms of N_2 were performed on *x*Bi/Ti@MSN_800 series. For clarity of exposition, in Figure 5, only MSN, 10TiO_2@MSN and 0.25Bi/Ti@MSN_800 samples are compared.

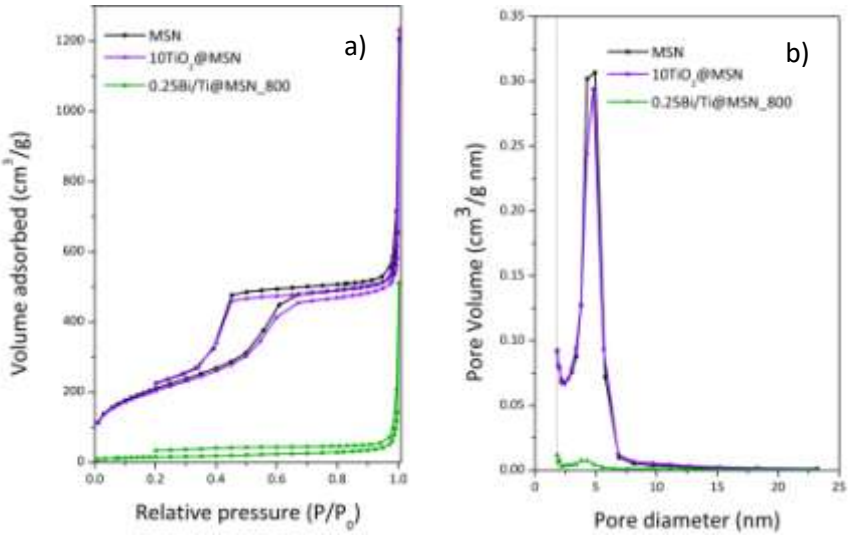

Figure 5 N_2 adsorption/desorption isotherm (a) and pore size distribution (b) of MSN, $10TiO_2$@MSN and 0.25Bi/Ti@MSN_800 samples.

Table 3 clearly shows that for all the samples of the *x*Bi/Ti@MSN_800 series, the surface area is very low. In addition, the pore volume decreases consistently for all *x*Bi/Ti@MSN_800 series, from 0.8 cm^3/g for $10TiO_2$@MSN to 0.1 cm^3/g for 2.50Bi/Ti@MSN_800. From these results we can conclude that even at small amount, the impregnation of the system with bismuth salt affects the silica structure, determining the closure of the pores. Bi^{3+} ion have a key role in the closure of the pores thanks to its low melting point.

Table 3 Surface area and pore volume of MSN, $10TiO_2$@MSN and *x*Bi/Ti@MSN_800 samples.

Sample	S.A.[a] (m^2/g)	D_p[b] (nm)
MSN	805	0.9
$10TiO_2$@MSN	737	0.8
0.25Bi/Ti@MSN_800	54	0.1
0.50Bi/Ti@MSN_800	23	0.1
1.15Bi/Ti@MSN_800	36	0.1
2.50Bi/Ti@MSN_800	14	0.4

In order to understand the role of bismuth ions, TEM analysis were conducted on *x*Bi/Ti@MSN_800 series.

As shown in Figure 6a, for the sample 0.25Bi/Ti@MSN_800, the mesoporous structure in the inner part is retained with a discrete organization of the channels, while in the surface of the particles it is completely lost. This means that already at the lowest concentration, bismuth ions are able to change the morphology of the preexisting structure, in according with XRPD analysis at the low angle region (see Figure 2) and the N_2 physisorption data previously discussed (see Figure 5). From the TEM micrographs it is also evident that bismuth ions induce a self-sealing process on the surface of the MSN. Figure 6 show the formation of small crystallites grown inside the silica pores, and EDX investigations confirm the presence of Bi, Ti, O and Si.

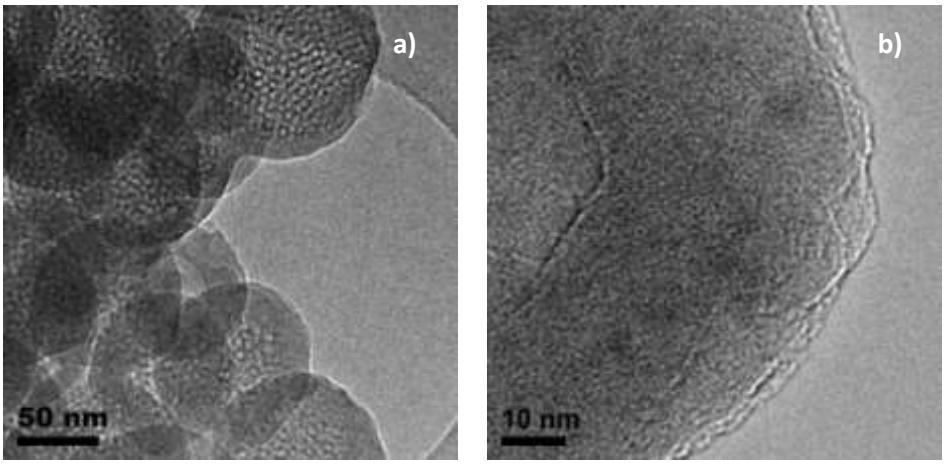

Figure 6 TEM micrographs of 0.25Bi/Ti@MSN_800 sample.

With the increasing of the bismuth content, as shown in Figure 7 for 0.50Bi/Ti@MSN_800 and 1.15Bi/Ti@MSN samples, the inner porosity is completely lost. The self-sealing process is even more evident and it occurs in a homogeneous manner, assuring the complete closure of the superficial pores. In 1.15Bi/Ti@MSN sample the nanoparticles tend to agglomerate (Figure 7). High resolution confirms also the presence of small crystallites grown inside the silica matrix and the EDX analysis evidences the presence of Bi, Ti, O and Si. At these concentrations, TEM micrographs show the presence also of larger $Bi_xTi_yO_z$ and Bi_2SiO_5 nanoparticles as already evidenced by the previous XRPD analysis. TEM investigations show that also the larger particles are embedded into the silica matrix.

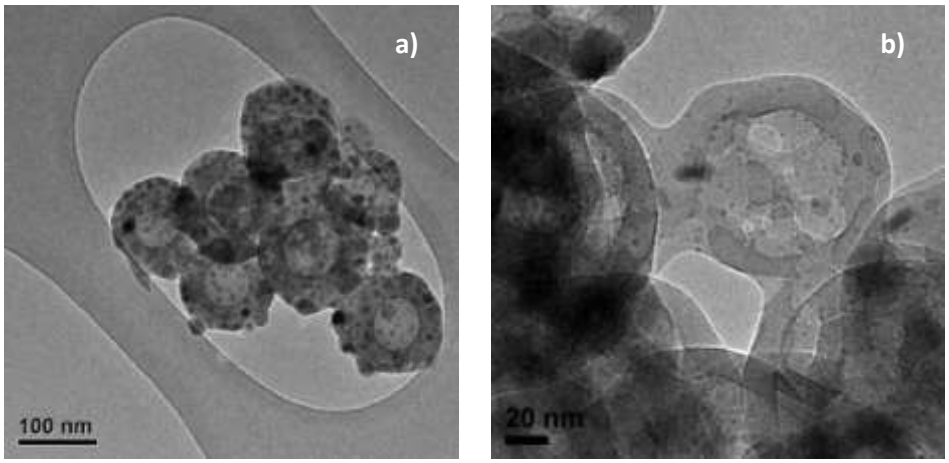

Figure 7 TEM micrographs of 0.50Bi/Ti@MSN_800 (a) and 1.15Bi/Ti@MSN_800 (b) samples.

At the maximum bismuth content (2.50 Bi/Ti@MSN_800 sample), in according with XRPD and EDX analysis, Bi_2SiO_5 nanoparticles, much larger in size, start to grow out of the silica matrix, as shown in Figure 8. High resolution investigations still reveals the presence of small crystallites formed inside the silica network (Figure 8b).

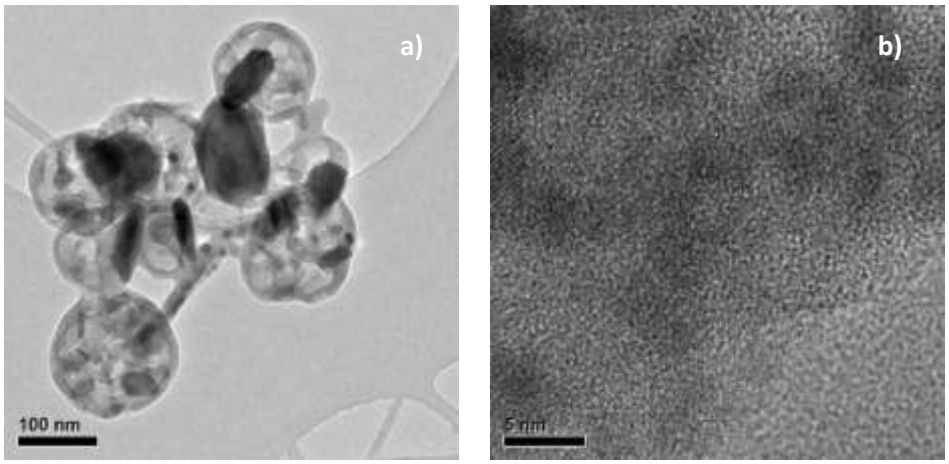

Figure 8 TEM micrographs of 2.50Bi/Ti@MSN_800.

Optical reflectivity measurements were performed on the powder samples to obtain absorption information and to evaluate the corresponding bandgap.

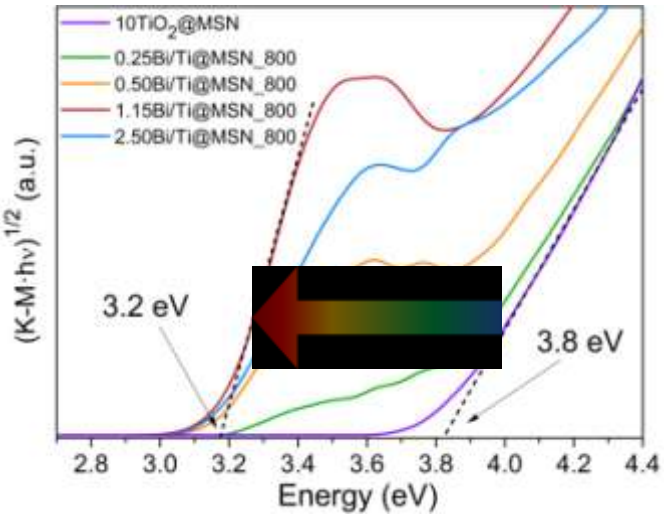

Figure 9 Kubelka-Munk function vs Energy of $10TiO_2$@MSN and *x*Bi/Ti@MSN_800 series and sample.

Since anatase phase and both $Bi_2Ti_2O_7$ and $Bi_4Ti_3O_{12}$ phases are indirect bandgap semiconductors,[8c] the bandgap energy of the systems was estimated from the Tauc plot[18] of the Kubelka-Munk absorption (K-M), plotting $(K\text{-}M \cdot h\nu)^{1/2}$ versus h*ν*, (Figure 9). Following this approach, the 0.25Bi/Ti@MSN_800 sample shows a band gap energy similar to the value found for the $10TiO_2$@MSN sample. This is certainly due to the low Bi content. As the Bi/Ti molar ratio increases, the band gap energy value is equal to 3.2 eV, corresponding to an absorption edge of 388 nm. Table 4 summarizes the band gap energies and the absorption edges of the *x*Bi/Ti@MSN_800 samples.

Table 4 Band gap energy and absorption edge of $10TiO_2$@MSN and *x*Bi/Ti@MSN_800 samples.

Sample	Theoretical Bi/Ti molar ratio	Measured Bi/Ti molar ratio*
$10TiO_2$@MSN	3.8	326
0.25Bi/Ti@MSN_800	3.7	335
0.50Bi/Ti@MSN_800	3.2	388
1.15 Bi/Ti@MSN_800	3.2	388
2.50Bi/Ti@MSN_800	3.2	388

Photocatalytic activity

To evaluate the photocatalytic behavior of *x*Bi/Ti@MSN_800 system, the decolorization of MO under irradiation was tested.

As shown in Figure 10, the photocatalytic activity of *x*Bi/Ti@MSN_800 after 240 minutes of UV irradiation is very low if compared to the photocatalytic activity of $10TiO_2$@MSN. Even though, as previously reported, $Bi_xTi_yO_z$ systems are well known photocatalysts, the introduction of bismuth ions into the TiO_2@MSN structure (*x*Bi/Ti@MSN_800 samples), induce a strong reduction on the photodegradation of the dye.

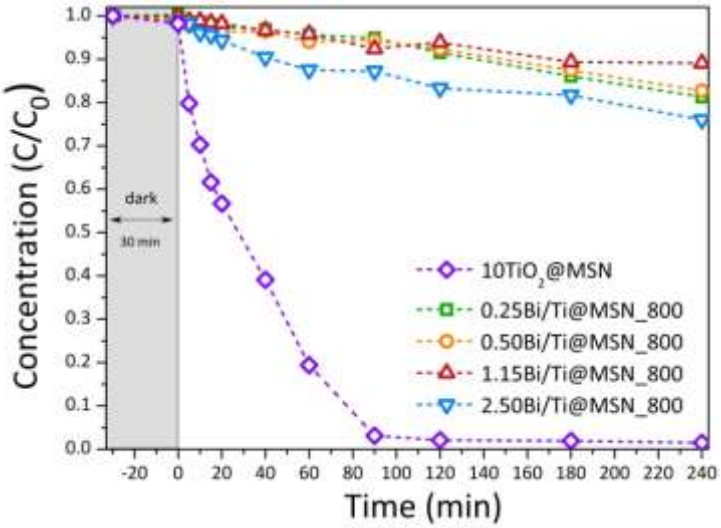

Figure 10 Performances of adsorption and MO photodegradation on *x*Bi/Ti@MSN_800 series under UV irradiation.

This general result is in agreement with what previously supposed and then confirmed by TEM analysis (see Figure 6, Figure 7 and Figure 8): bismuth ions act as low melting agent in a self-sealing process. The photocatalysts are trapped inside the silica and they are not reachable from the dye. Within the experimental errors, the samples with 0.25, 0.50 and 1.15 molar ratio are comparable. Concerning the sample with a 2.50 molar ratio, it shows a slightly higher photocatalytic activity. Since the XRPD and TEM analysis show respectively a consistent amount of bismuth silicate and that part of these nanoparticles grow outside the silica matrix (Figure 8), we can conclude that Bi_2SiO_5 nanoparticles are in direct contact with MO, determining the ability to slightly decolorize the dye.

5.4 Study of the role of the annealing temperature

5.4.1 Results and discussion

The role of the annealing temperature on the growth of the crystalline nanoparticles was investigated as function of thermal treatments between 500 and 800°C.

As reported in Figure 11, the analysis of the low angle region shows that as the calcination temperature increases, the ordered hexagonal mesoporous structure of silica matrix is not retained. In particular, an initial decrease of the order occurs already at 500°C, up to a complete loss of the mesoporous structure at 800°C. This loss can be due to either to a high degree of disorder of the pores or to a complete collapse of the silica network.

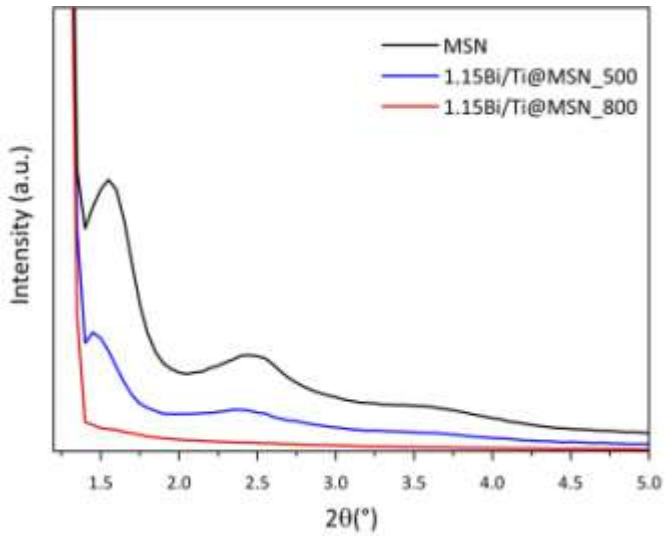

Figure 11 XRD spectra of MSN, 1.15Bi/Ti@MSN_500 and 1.15Bi/Ti@MSN_800 samples in the small-angle region.

In the wide angle region reported in Figure 12, it is evident that as the calcination temperature increases, the broad diffraction halo due to the amorphous silica decreases while the crystalline fraction increases. The pattern of the sample treated at 500°C, in addition to the amorphous silica matrix contribution, evidences the presence of weak peaks due to the tetragonal bismuth oxide Bi_2O_3 (β-type) phase (PDF 010-77-5341) and to the orthorhombic bismuth silicate Bi_2SiO_5 phase (PDF 01-075-1483). At the highest temperature (1.15Bi/Ti@MSN_800 sample), three crystalline phases can be clearly observed: the cubic $Bi_2Ti_2O_7$ (PDF 01-074-4250), the orthorhombic $Bi_4Ti_3O_{12}$ (PDF 010-77-9500), and a small amount of bismuth silicate Bi_2SiO_5 (Figure 13). In order to emphasize and clarify the structural

evolution of the Bi-compounds as function of the temperature, in Figure 12b, a magnification of the patterns in the range 25-35° is reported.

The diffraction patterns can be summarized as follows:

(i) at the lowest temperature, 500°C, the bismuth ions start to react with the silica matrix, forming bismuth silicate and showing a small amount of Bi_2O_3;

(ii) at 600°C, Bi_2SiO_5 still grows and a small amount of $Bi_2Ti_2O_7$ appears, suggesting an interaction of bismuth ions with TiO_2 nanoparticles;

(iii) finally, from 700°C to 800°C bismuth titanates ($Bi_2Ti_2O_7$ and $Bi_4Ti_3O_{12}$) grow progressively at the expense of bismuth silicate.

We can tentatively concluded that the bismuth silicate is the first crystalline phase to be stabilized, but bismuth titanates are thermodynamically favored at higher temperatures.

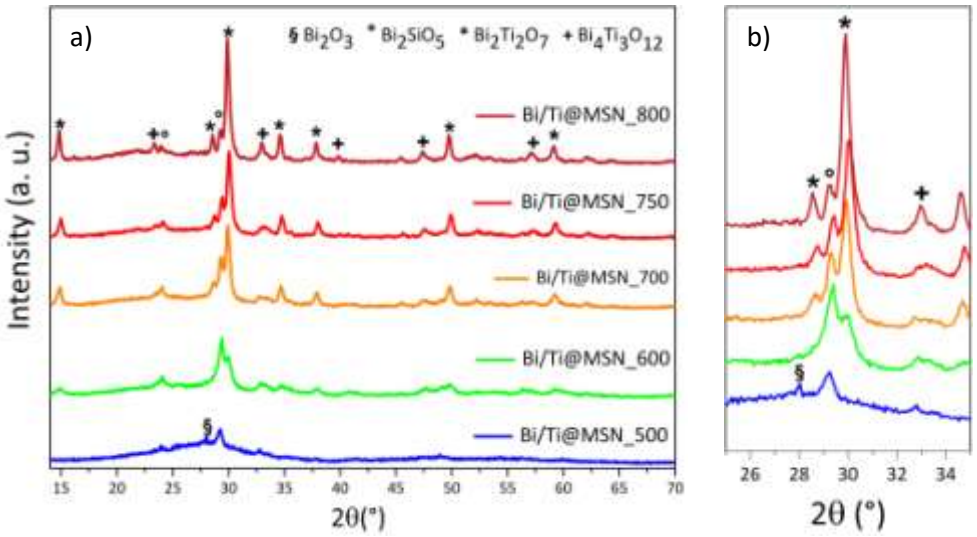

Figure 12 XRPD patterns of 1.15Bi/Ti@MSN_y samples in the wide-angle region from 15° to 70°(a) and magnification in the 25-35° range (b).

Scherrer equation applied to the Rietveld refinement outputs gave the crystallite sizes of $Bi_2Ti_2O_7$, $Bi_4Ti_3O_{12}$ and Bi_2SiO_5 for the samples treated at 750°C and 800°C (Table 5); for the samples calcined at lower temperatures it was not possible to distinguish the peaks belonging to different phases and, for this reason, XRPD size determination was not feasible (Figure 13).

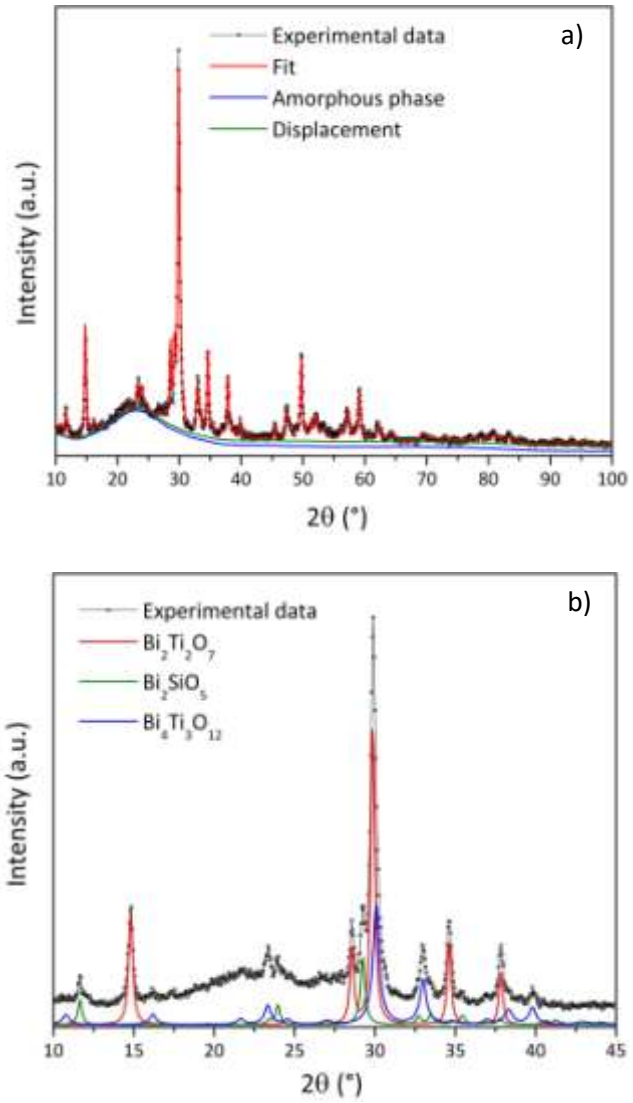

Figure 13 Rietveld refinement XRPD pattern (a) and phase contributions in XRPD pattern (b) of 1.15Bi/Ti@MSN_800 sample.

Table 5 XRPD measurements of Bi_2SiO_5, $Bi_2Ti_2O_7$ and $Bi_4Ti_3O_{12}$ crystallite sizes obtained from Rietveld refinements for 1.15Bi/Ti@MSN_750 and 1.15Bi/Ti@MSN_800 samples.

Sample	Crystalline phase (nm)		
	Bi_2SiO_5	$Bi_2Ti_2O_7$	$Bi_4Ti_3O_{12}$
1.15 Bi/Ti@MSN_750	19	21	19
1.15Bi/Ti@MSN_800	29	21	15

Quantitative determinations of Ti and Bi by SF-ICP-MS measurements were conducted on 1.15Bi/Ti@MSN (not calcined), 1.15Bi/Ti@MSN_500 and 1.15Bi/Ti@MSN_800 samples and the values are reported in Table 6. These values are compared with the ones obtained by the XRPD phase quantitative analysis on the semicrystalline samples.

Table 6 Quantitative determination (wt%) of SiO_2, Bi_2O_3 and TiO_2 phase contributions in 1.15Bi/Ti@MSN (not calcined), 1.15Bi/Ti@MSN_500 and 1.15Bi/Ti@MSN_800 samples.

Sample	Crystalline phase	Theoretical (%)	SF-ICP-MS (%)	XRPD (%)
1.15Bi/Ti@MSN (not calcined)	SiO_2	66.18	75.63	-
	TiO_2	7.35	6.56	-
	Bi_2O_3	26.47	17.81	-
1.15Bi/Ti@MSN_500	SiO_2	66.18	72.33	-
	TiO_2	7.35	6.41	-
	Bi_2O_3	26.47	21.26	-
1.15Bi/Ti@MSN_800	SiO_2	66.18	75.43	78.20
	TiO_2	7.35	6.53	4.80
	Bi_2O_3	26.47	18.00	17.00

The ICP and the XRDP results are in good agreement and they show that the Bi and Ti content is lower than the theoretical ones, for all the analyzed samples. This evidence suggests that the loss of bismuth is not affected by the thermal treatments, as one might have assumed considering the volatility of bismuth at high temperature, but it probably occurs during the impregnation step. The same conclusion can be drawn also in the case of titanium.

The modification of the pores structure, with the thermal treatment, is also confirmed by the nitrogen adsorption-desorption analysis. The isotherms and the corresponding pore size distribution plots are shown in Figure 14 a and b, respectively.

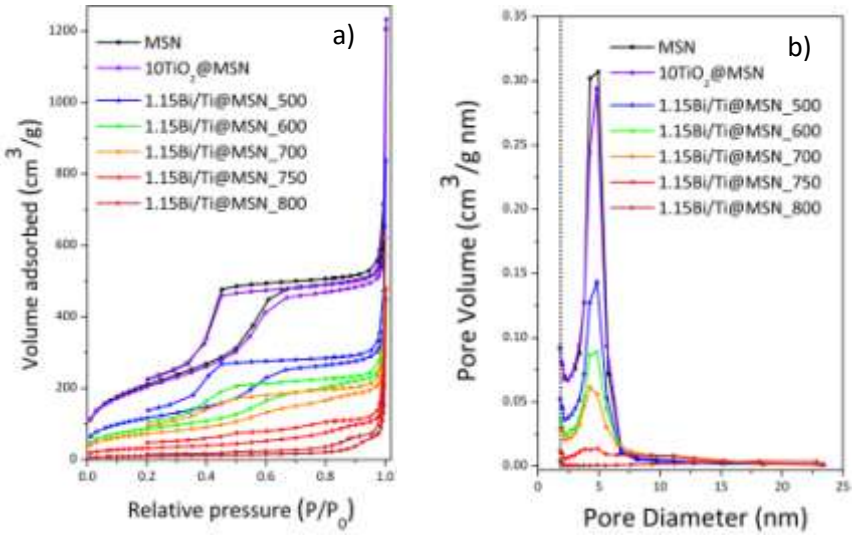

Figure 14 N_2 adsorption-desorption isotherms (a) and BJH pore size distribution (b) of MSN and 1.15Bi/Ti@MSN_*y* samples.

As previously discussed in paragraph 3.2., MSN sample exhibits the typical type IV profile with a H2 hysteresis loop (IUPAC classification) due to the capillary condensation steps at relative pressures p/p_0 in the range of 0.3-0.6, typical of ordered and mesoporous materials with two-dimensional cylindrical pores. The bare MSN displays a high BET specific surface area (805 $m^2\ g^{-1}$) and the distribution of the pore diameter is very narrow and centered at 4.2 nm. After the MSN impregnation with the TiO_2 precursor ($10TiO_2$@MSN sample), the amount of N_2 adsorption slightly decreases due to the formation of TiO_2 nanoparticles; nevertheless, the mesoporous silica structure is retained, maintaining a type IV isotherm profile.

After the addition of bismuth ions (1.15Bi/Ti@MSN_*y* series), the mesoporous structure is still kept for the sample treated at the lowest calcination temperature (1.15Bi/Ti@MSN_500). When the temperature raises, a progressive decrease of the specific surface area is observed: compared to $10TiO_2$@MSN, 1.15Bi/Ti@MSN_500 shows a significant reduction of the surface area (413 m^2/g), that drastically falls off at 36 m^2/g for 10Bi/Ti@MSN_800. Such a progressive decrease could be ascribed to both the formation of nanoparticles that block the silica channels and to the Bi^{3+} ions that could have a key role in the closing of the pores as the calcination temperature increases. This is also confirmed by the significant decrease of the pore volume which occurs already at the lowest temperature (0.5 cm^3/g), and drastically lessens for the sample treated at the highest temperature (0.2 cm^3/g). The textural properties of the samples (specific surface area, and specific pore volume) are summarized in Table 7.

Table 7 Comparison of textural properties of MSN, $10TiO_2$@MSN and 1.15Bi/Ti@MSN_*y* samples. [a] Obtained from BET equation; [b] Obtained from BJH desorption average pore volume; the estimated error is ±10%.

Sample	Surface Area [a] (m^2/g)	Pore Volume [b] (cm^3/g)
MSN	805	0.9
$10TiO_2$@MSN	737	0.8
1.15Bi/Ti@MSN_500	413	0.5
1.15Bi/Ti@MSN_600	304	0.4
1.15Bi/Ti@MSN_700	256	0.3
1.15Bi/Ti@MSN_750	112	0.2
1.15Bi/Ti@MSN_800	36	0.2

In order to verify the possible key role of the bismuth ions and their interactions with titanium and the silica network, the Ti-MSN sample was also calcined at 800°C. A slight decrease of both the specific surface area (568 m^2/g) and the pore volume (0.6 cm^3/g) is shown, however, the mesoporous structure is still maintained and it is not collapsed (not shown).

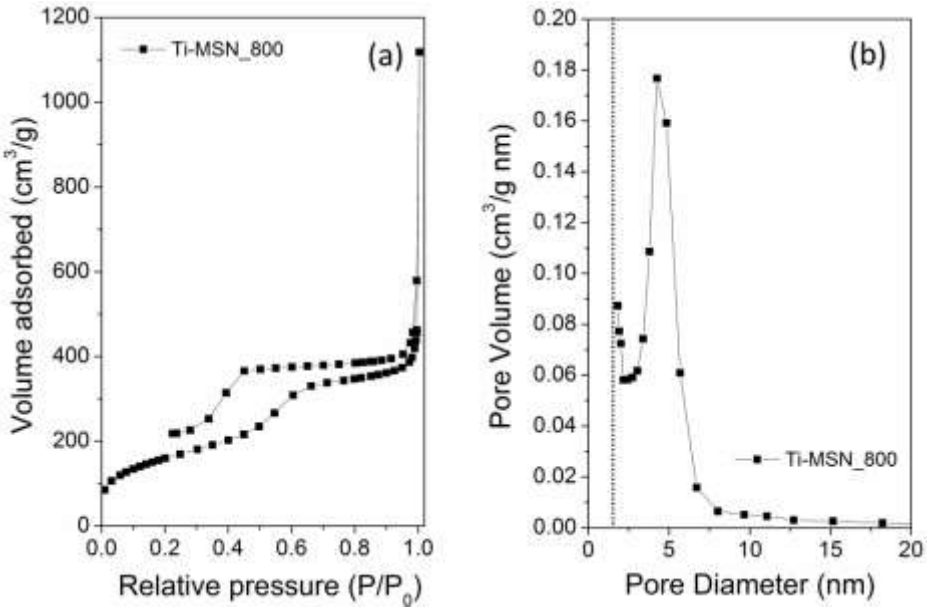

Figure 15 N_2 adsorption-desorption isotherms (a) and BJH pore size distribution (b) of $10TiO_2$@MSN_800 sample.

In order to understand how Bi^{3+} ions act when it is added to $10TiO_2$@MSN system, FE-SEM analysis were conducted. Figure 16 displays that at 600°C and at 800°C the spherical morphology of the silica matrix is not changed.

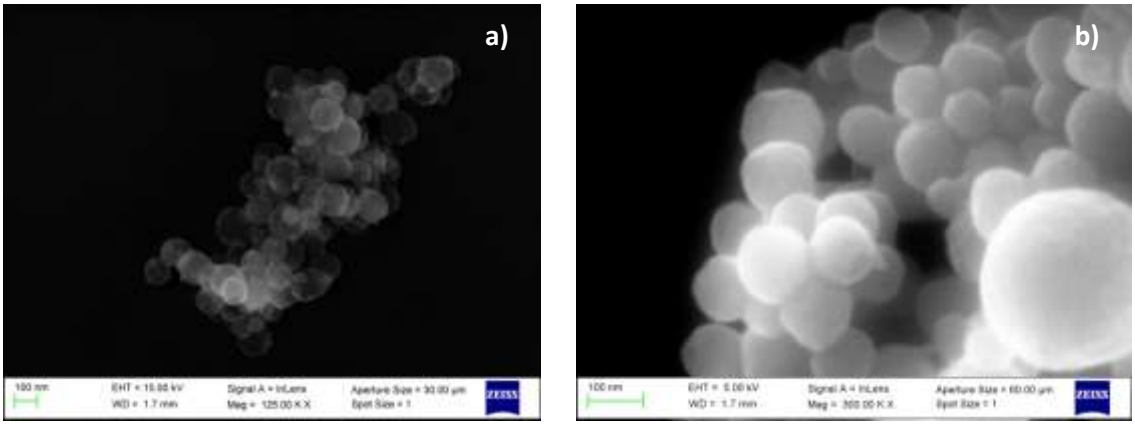

Figure 16 FE-SEM micrographs of 1.15Bi/Ti@MSN_600 (a) and 1.15Bi/Ti@MSN_800 (b) samples.

The backscattered electron image of a selected area of the 1.15Bi/Ti@MSN_800 sample (Figure 17b), shows the distribution of the heavy element (lighter areas of the image) in the sample.

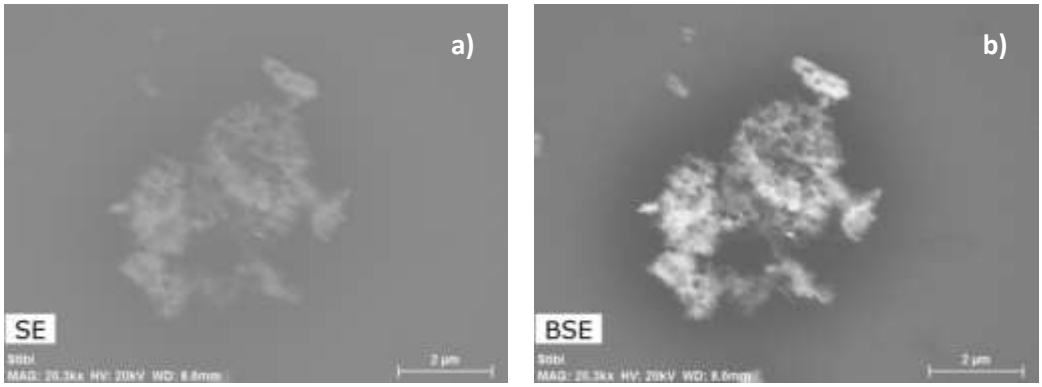

Figure 17 FE-SEM micrographs of 1.15Bi/Ti@MSN_800 specimen collected with secondary electrons (a) and backscattered electrons (b).

With the purpose of evaluating the homogeneity of the samples, an elemental mapping at microstructural level by energy dispersive X-ray spectroscopy (EDS) was performed. The analysis confirms the presence of Ti and Bi and the homogeneity of the distribution of both the elements into the selected area (Figure 18 a,b,c).

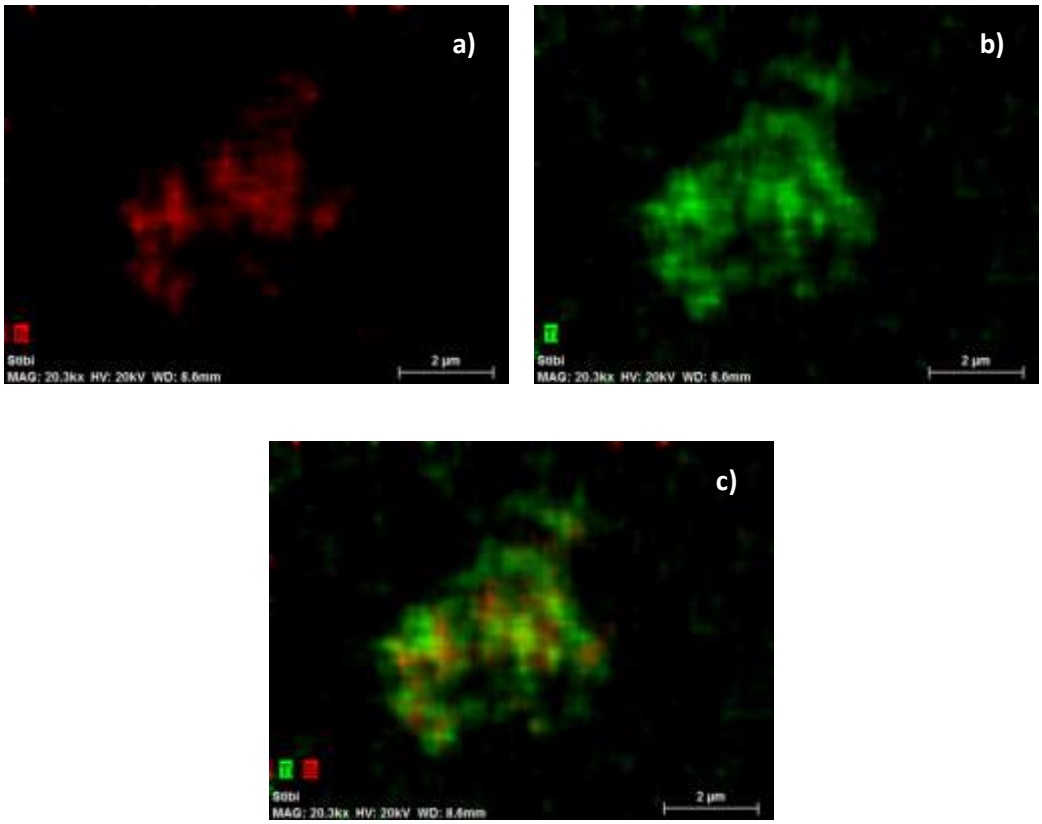

Figure 18 Elemental EDS map of Bi (a), Ti (b) and Bi/Ti (c)

The effect of the calcination temperature on 1.15Bi/Ti@MSN_*y* was confirmed by TEM analysis. As shown in Figure 19a and b, at 500°C the ordered mesoporous structure is retained in the inner area of the particles, while it is partially lost in the superficial layer, due to the bismuth ions that act as low melting agent. Bismuth and titanium elements, as confirmed by EDX analysis, impregnate homogeneously the system and the growth of small particles inside the channels of MSN is revealed by High Resolution images (HRTEM), as reported in Figure 19d.

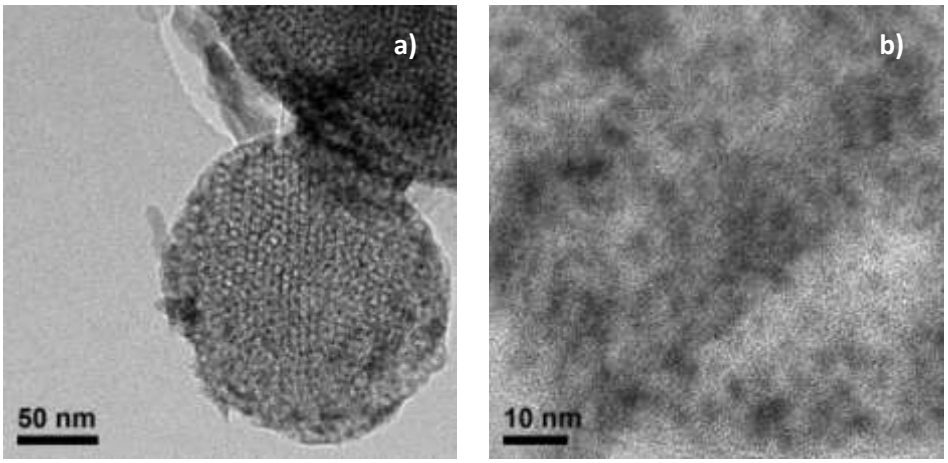

Figure 19 TEM micrographs of 1.15Bi/Ti@MSN_500 sample.

As reported in Figure 20a, at 600°C the mesoporous structure is still distinctive visible in the inner part, but the pore organization is less evident. On the MSN surface layers, the self-sealing process starts to be more consistent, with the consequent closure of the channels. High resolution and EDX analysis confirm the formation of small crystallites of bismuth titanate (Figure 20b) into the silica matrix.

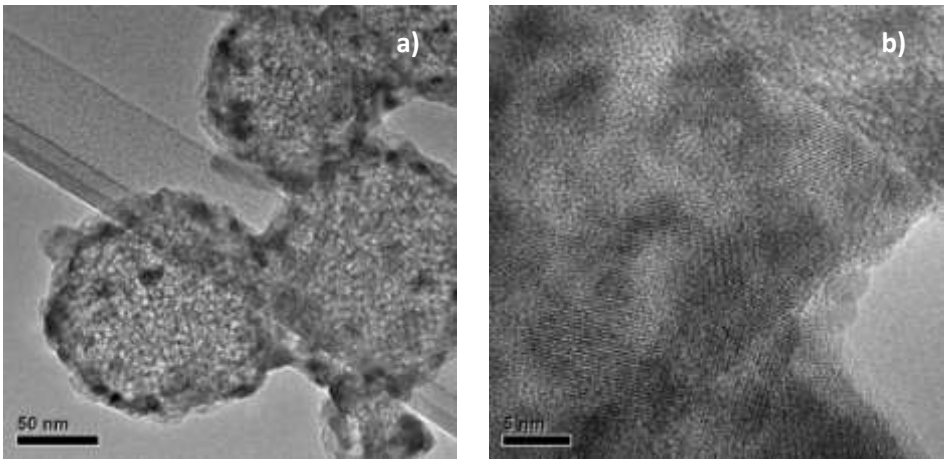

Figure 20 TEM micrographs of 1.15Bi/Ti@MSN_600 sample.

As shown in Figure 21a, with the increasing of the calcination temperature at 700°C, the mesoporous structure is still present, but it is not more organized in an ordered manner. Furthermore, at this temperature, bismuth ions are able to strongly interact with the silica matrix leading to the completely closure of the superficial channels during the self-sealing process. TEM analysis reveal also the formation of small nanoparticles into the mesoporous

silica nanoparticles (Figure 21b). This means that thanks to the self-sealing property, the photocatalysts are no longer available to the surrounding environment. Also for this sample, EDX analysis confirms the homogeneous presence of Bi, Ti, O and Si elements.

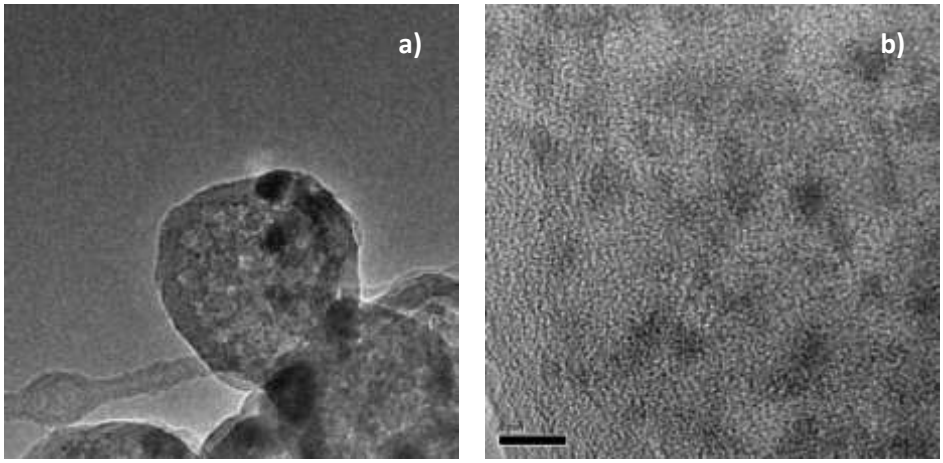

Figure 21 TEM micrographs of 1.15Bi/Ti@MSN_700 sample.

Compared to the other samples treated at lower temperatures, the mesoporous structure is completely lost in the sample calcined at 800°C, as shown in Figure 22a. TEM investigations prove that at this temperature the self-sealing process is even more evident and it occurs in a homogeneous manner, assuring the complete closure of the superficial pores. High resolution confirm the presence of small crystallites grown inside the silica matrix (Figure 22b) and EDX analysis confirm that Bi, Ti, O and Si elements are present.

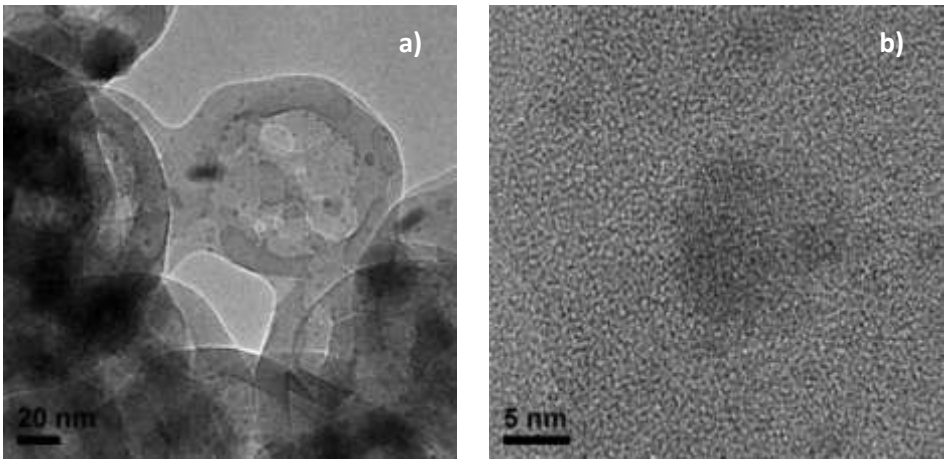

Figure 22 TEM micrographs of 1.15Bi/Ti@MSN_800 sample.

With the aim to analyze the first 5-10 nm of the surface of the nanoparticles and clarify the role of Bi^{3+} in the self-sealing process, XPS spectra of MSN, 10TiO_2@MSN, 1.15Bi/Ti@MSN_600 and 1.15Bi/Ti@MSN_800 were also collected. The silicon, oxygen, titanium and bismuth atomic fractions are summarized in Table 8 and the binding energy values of the XPS main bands are reported in Table 9.

Table 8 Si, O, Ti and Bi atomic fraction as obtained by XPS data in MSN, 10TiO2@MSN, 1.15Bi/Ti@MSN_600 and 1.15Bi/Ti@MSN_800 samples.

	MSN	10TiO_2@MSN	1.15Bi/Ti@MSN_600	1.15Bi/Ti@MSN_800
Si	33%	27%	30%	32.3%
O	67%	67%	65%	64%
Ti	-	6%	2%	1.5%
Bi	-	-	3%	2.2%

Table 9 XPS binding energy of the main detected bands of MSN, 10TiO_2@MSN, 1.15Bi/Ti@MSN_600 and 1.15Bi/Ti@MSN_800 samples. In case of more than one component underlying, the different BE values are given with the relative component intensity as obtained by the fitting procedure.

Sample	Si		O	Ti	Bi	
	Si2p	*Si2s*	*O1s*	*Ti2p*	*Bi4d*	*Bi4f*
MSN	103.3	-	532.7	-	-	
10TiO_2@MSN	103.3	-	530.2 (29%) 532.7 (71%)	458.6	-	
1.15Bi/Ti@MSN_600	103.3	154.2	530.1 (13%) 532.7 (87%)	458.0	441.8	159.0
1.15Bi/Ti@MSN_800	103.3	154.1	530.0 (10%) 532.6 (90%)	457.7	441.5	158.8

XPS spectra of MSN (Figure 23) displays Si2p and O1s bands centered at 103.3 eV and 532.7 eV of BE, respectively, typical values for silica matrix.[19] The quantitative analysis agree with the presence of silicon dioxide, being the atomic fraction ratio O/Si about 2.

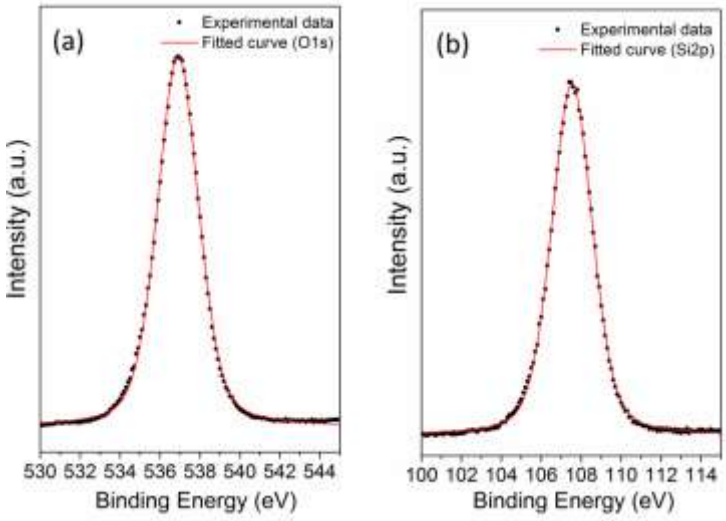

Figure 23 XPS Si2p (a) and O1s (b) bands for MSN sample.

In the 10TiO_2@MSN sample, besides the Si2p and O1S bands, a Ti2p doublet is clearly visible (Figure 24), whose Ti2$p_{3/2}$ peak is centered at 458.6 eV of BE. This value is compatible with Ti^{4+} presence.[19] The Si2p band is the same as for MSN sample. O1s peak is the overlap of two different components: the first, less intense, centered at 530.2 eV, is in agreement with presence of TiO_2;[19] the second, more intense and centered at 532.7 eV, is related to oxygen atoms forming SiO_2. The calculated stoichiometry of titanium oxide is in agreement with the presence of Ti dioxide, within experimental errors. Converting the atomic fraction to weight percentage, it results that TiO_2 represents about 23% of the sample instead of the loaded 10%. Since XPS analysis can provide information only on the first 5-10 nm from the sample surface, it means that the surface of the sample is richer in TiO_2 than the core.

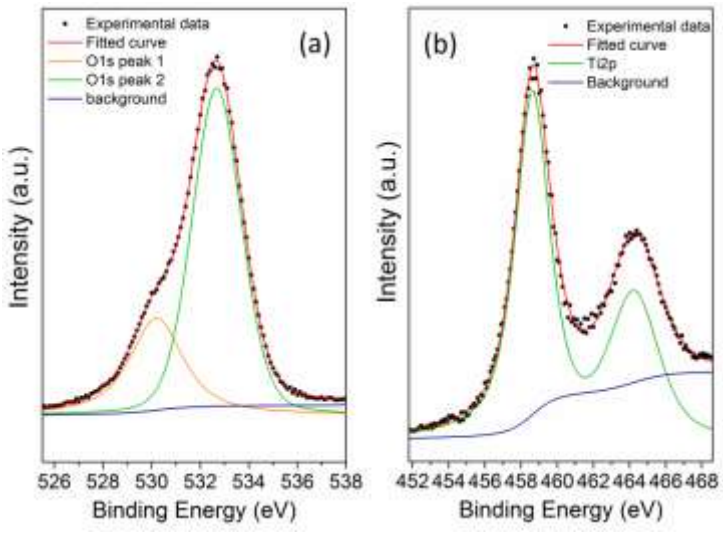

Figure 24 XPS O1s (a) and Ti2p (b) bands for the 10TiO_2@MSN sample.

In addition to Si, O, and Ti XPS related bands, 1.15Bi/Ti@MSN_600 sample shows also bands due to Bi, in particular Bi4d and Bi4f (Figure 25). The $4d_{5/2}$ and $4f_{7/2}$ doublet components fall at 441.8 eV and 159.0 eV of BE, respectively: these values agree with the presence of Bi^{3+}.[19] Even if Bi4f band is usually used for the quantitative analysis, in our case we are forced to use $Bi4d_{5/2}$ band since the former strongly interferes with Si2s signal. $Ti2p_{3/2}$ doublet component (Figure 25c) was centered around 458.0 eV of BE, thus suggesting the presence of Ti^{4+}.[19] O1s band can be seen as overlap of two components (Figure 25a): the first, due to oxygen atoms forming TiO_2, Bi_2O_3, and/or mixed compounds such as bismuth silicate or titanate, corresponded to about 13% of the total intensity; the second is related to oxygen forming SiO_2, having 87% of the total O1s intensity. The hypothesis of the presence of TiO_2, Bi_2O_3, and/or more complex oxides is in agreement also with the related atomic fractions, as can be deduced by data reported in Table 8. If compared to $10TiO_2$@MSN sample, here the amount of titanium at the surface of the sample decreases from 6% to 2%. This result is not depending on the fitting parameters: by fixing larger values of the Ti2p band intensity, we could not obtain an acceptable fit of the experimental spectrum. This suggested that titanium compounds are deeper inside the silica matrix, probably because of the surface mesopores closing as a consequence of bismuth introduction. Moreover, the amount of Bi is 3%, slightly higher than Ti: this is compatible with the possibility that a part of oxidized bismuth forms bismuth titanate, while the remaining part is forming bismuth silicate.

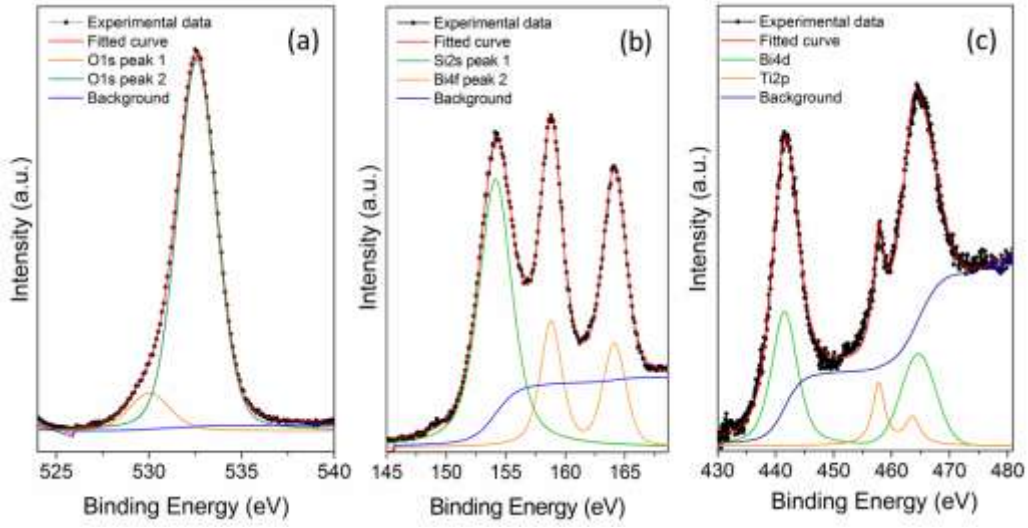

Figure 25 XPS O1s (a), Si2s+Bi4f (b) and Bi4d+Ti2p (c) bands revealed by the 1.15Bi/Ti@MSN_600 sample.

The bands detected for 1.15Bi/Ti@MSN_800 show very similar BE position of those found for 1.15Bi/Ti@MSN_600. As reported in Table 8, the amount of both Ti and Bi decrease,

passing from 2.0% to 1.5% and from 3.0% to 2.2%, respectively. Also in this case, the difference is not an artifice of the fitting procedure, as evidenced also by a direct comparison of the spectra recorded for the two different samples. This suggested that bismuth titanate could be more and more covered by silica, located deeper and deeper below the surface of the silica particle.

In summary, the XPS results are in agreement with the hypothesis previously reported and depicted in Figure 26: as the temperature of the thermal treatment increases, bismuth titanates nanocrystals grow inside the silica network and simultaneously the Bi^{3+} ions acts as a low-melting point agent for silica, leading to a self-sealing process, that prevents the photocatalytic activity of bismuth titanates.

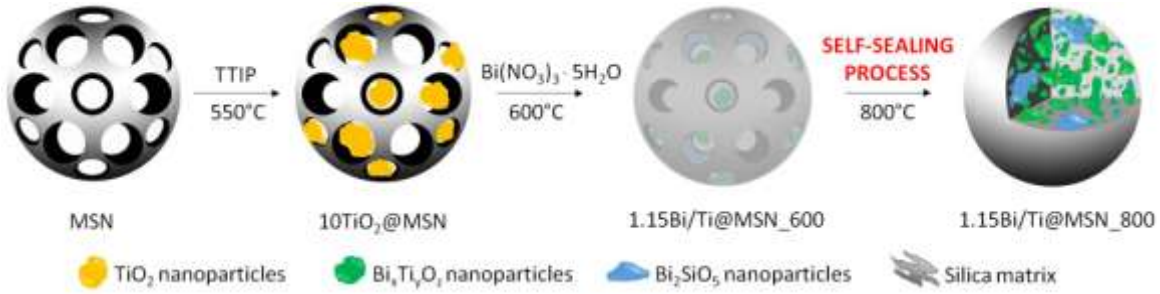

Figure 26 Schematic process of the growth of $Bi_xTi_yO_z$ into MSN: MSN is impregnated with TTIP and calcined at 550°C to form TiO_2 nanoparticles ($10TiO_2$@MSN); subsequently, the adding of $Bi(NO_3)_3{\cdot}5H_2O$ and the thermal treatment at 600°C lead to the formation of $Bi_2Ti_2O_7$ and Bi_2SiO_5 nanoparticles inside the silica channels, furthermore in the inner part the mesoporous structure is still kept, while at the surface a self-sealing process occurs (1.15Bi/Ti@MSN_600); finally, with the arising calcination temperature to 800°C, also $Bi_4Ti_3O_{12}$ phase grows, a complete collapse of the inner mesoporous structure occurs and the self-sealing process in the particles is completed (1.15Bi/Ti@MSN_800).

Optical reflectivity measurements were performed on the samples to obtain absorption information and to evaluate the corresponding bandgap. For clarity of exposition, in Figure 27a, only the spectra of $10TiO_2$@MSN and 1.15Bi/Ti@MSN_800 samples are shown. It is notable that the formation of $Bi_xTi_yO_z$ spread the absorption in the UVA region -only partially accessible by the $10TiO_2$@MSN sample with a significant theoretical impact on the UV-filter properties. As previously discussed, since anatase phase and both $Bi_2Ti_2O_7$ and $Bi_4Ti_3O_{12}$ phases are indirect bandgap semiconductors,[8c] the bandgap energy of the systems was estimated from the Tauc plot[18] of the Kubelka-Munk absorption (K-M), plotting $(K\text{-}M \cdot h\nu)^{1/2}$ versus $h\nu$ (Figure 27b). Following this approach, absorption edges at about 3 eV are observed for 1.15Bi/Ti@MSN_*y* samples: compared to $10TiO_2$@MSN sample, which shows an absorption edge at about 3.65 eV, 1.15Bi/Ti@MSN_*y* samples show a significant blue shift.

The bandgap energies obtained for $10TiO_2$@MSN and 1.15Bi/Ti@MSN_*y* samples are higher than the values reported in literature for both anatase (≈3.2 eV)[20] and bismuth

titanates (≈2.9 eV for $Bi_2Ti_2O_7$ and ≈3.1 eV for $Bi_4Ti_3O_{12}$ respectively).[8c] This can be due to the quantum confinement of the nanocrystals well dispersed in the silica matrix.

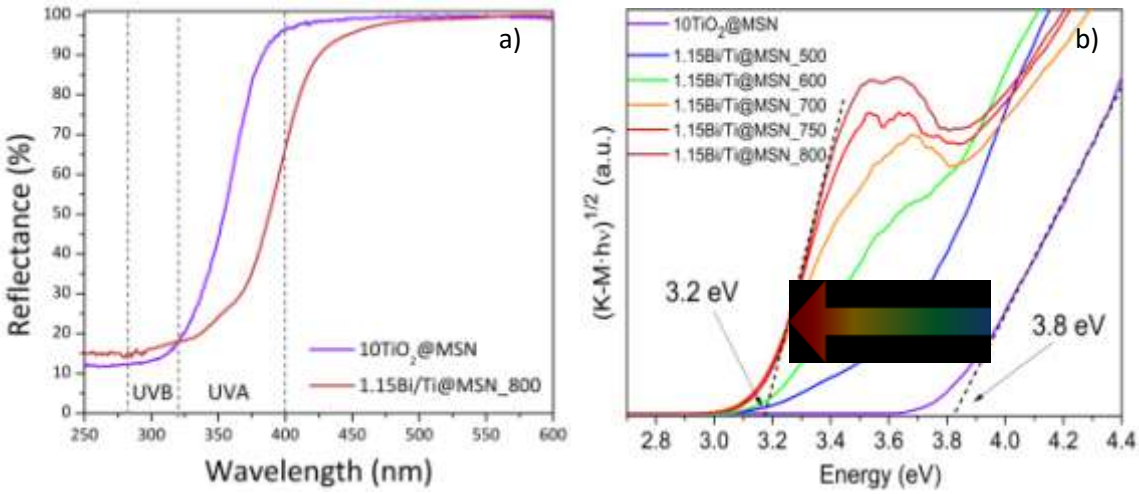

Figure 27 DR-UV spectra (a) and Kubelka-Munk function *vS* Energy (b) of $10TiO_2$@MSN and 1.15Bi/Ti@MSN_*y* samples

Photocatalytic activity

In order to verify the influence of the bismuth ion on the $10TiO_2$@MSN system on the photocatalytic activity of the system, the degradation of MO was tested, comparing the $10TiO_2$@MSN and the 1.15Bi/Ti@MSN_*y* samples. As shown in Figure 28, after 30 min of equilibration in the dark, the amount of MO adsorbed on the materials is negligible.

The $10TiO_2$@MSN sample displays a high photocatalytic activity toward MO, completely degraded after 90 minutes of UV irradiation. With the introduction of bismuth ions and the consequent formation of Bi-composites (1.15Bi/Ti@MSN_*y* samples), a strong reduction on the photodegradation of the dye occurs. In particular, the trend observed for the MO degradation shows that, as the calcination temperature increases, the photocatalytic efficiency tails off. After 240 minutes under UV light, there is a degradation of about 29.6% for 1.15Bi/Ti@MSN_500, 28.6% for 1.15Bi/Ti@MSN_600, 26.5% for 1.15Bi/Ti@MSN_700 and 11% for 1.15Bi/Ti@MSN_800.

The results, theoretically inconsistent with the photocatalytic ability of the bismuth titanates, are in agreement with the scenario in which:

(i) at low annealing temperatures the pores are not completely sealed and the MO is able to reach partially the photocatalyst;

(ii) increasing the calcination temperature, bismuth titanates grow but at the same time a self-sealing process starts to occur;

(iii) at the higher calcination temperatures the silica network collapses, preventing the direct contact between MO and the photocatalyst.

The photocatalytic tests demonstrate that the new system can be considered safe because the self-sealing process isolate the photocatalytic nanocrystals from the environmental molecules, causing the photocatalytic inactivity.

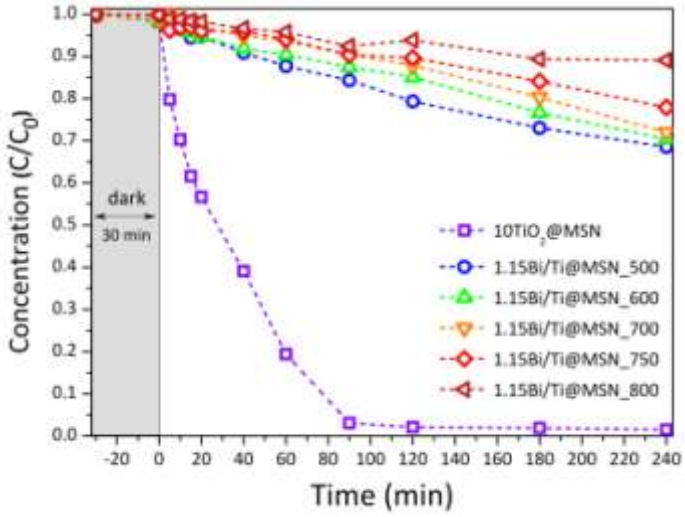

Figure 28 Performances of adsorption and MO photodegradation on $10TiO_2$@MSN and 1.15Bi/Ti@MSN_*y* series under UV irradiation.

5.5 Conclusions

In summary, a novel approach for the development of bismuth-based safe self-sealing nanomaterials as inorganic sunscreen UV filters was reported.

The growth mechanism of $Bi_xTi_yO_z$ nanocrystals into MSN was analyzed in detail as function of the bismuth concentration and of the annealing temperature.

The concomitance loss of the silica mesoporous structure and the key role of bismuth ions in the self-sealing process was discussed by means of N_2 adsorption-desorption, FE-SEM, TEM and XPS analysis.

The synthesized samples display excellent UV properties and at the same time a reduced photocatalytic activity, fundamental requirements for the design of an inorganic UV filter.

The double role of bismuth ions in the spreading of the UV shield properties and the suppression of the photocatalytic properties make the proposed nanosystem a perfect candidate for the development of the next generation nanomaterials for the sun shields.

Moreover, the ability of bismuth to act as local low-melting ion for silica network, leading to a self-sealing process, can be exploited in the design of a wide range UV filter nanomaterials with the aim of cutting their photocatalytic ability.

References

[1] G. Dong, H. Fan, H. Tian, J. Fang, Q. Li, *RSC Advances* **2015**, *5*, 29618-29623.

[2] S. Dong, J. Feng, M. Fan, Y. Pi, L. Hu, X. Han, M. Liu, J. Sun, J. Sun, *RSC Advances* **2015**, *5*, 14610-14630.

[3] S. Sanna, V. Esposito, J. W. Andreasen, J. Hjelm, W. Zhang, T. Kasama, S. B. Simonsen, M. Christensen, S. Linderoth, N. Pryds, *Nat Mater* **2015**, *14*, 500-504.

[4] aJ. A. Salvador, S. A. Figueiredo, R. M. Pinto, S. M. Silvestre, *Future Medicinal Chemistry* **2012**, *4*, 1495-1523; bG. G. Briand, N. Burford, *Chemical Reviews* **1999**, *99*, 2601-2658; cJ. A. Salvador, S. A. Figueiredo, R. M. Pinto, S. M. Silvestre, *Future Med. Chem.* **2012**, *4*, 1495–1523.

[5] J. Shen, J. J. Cha, *Nanoscale* **2014**, *6*, 14133-14140.

[6] aM. Mehring, *Coordination Chemistry Reviews* **2007**, *251*, 974-1006; bP. Riente, A. Matas Adams, J. Albero, E. Palomares, M. A. Pericàs, *Angewandte Chemie International Edition* **2014**, *53*, 9613-9616.

[7] aD. J. Singh, S. S. A. Seo, H. N. Lee, *Physical Review B* **2010**, *82*, 180103; bS. Murugesan, M. N. Huda, Y. Yan, M. M. Al-Jassim, V. Subramanian, *The Journal of Physical Chemistry C* **2010**, *114*, 10598-10605; cO. Merka, D. W. Bahnemann, M. Wark, *Catalysis Today* **2014**, *225*, 102-110.

[8] aJ. R. Esquivel-Elizondo, B. B. Hinojosa, J. C. Nino, *Chemistry of Materials* **2011**, *23*, 4965-4974; bW. Wei, Y. Dai, B. Huang, *The Journal of Physical Chemistry C* **2009**, *113*, 5658-5663; cC. Turner, P. M. Johns, E. M. Thatcher, D. B. Tanner, J. C. Nino, *The Journal of Physical Chemistry C* **2014**, *118*, 28797-28803.

[9] aD. Hou, W. Luo, Y. Huang, J. C. Yu, X. Hu, *Nanoscale* **2013**, *5*, 2028-2035; bX. Lin, P. Lv, Q. Guan, H. Li, H. Zhai, C. Liu, *Applied Surface Science* **2012**, *258*, 7146-7153; cL. Jing, W. Zhou, G. Tian, H. Fu, *Chemical Society reviews* **2013**, *42*, 9509-9549; dD. Damjanovic, *Report on Progress in Physics* **1998**, *61*, 1267-1324.

[10] A. E. Nogueira, E. Longo, E. R. Leite, E. R. Camargo, *Journal of colloid and interface science* **2014**, *415*, 89-94.

[11] W. F. Yao, H. Wang, X. H. Xu, J. T. Zhou, X. N. Yang, Y. Zhang, S. X. Shang, *Applied Catalysis A: General* **2004**, *259*, 29-33.

[12] A. Hardy, S. Van Elshocht, C. De Dobbelaere, J. Hadermann, G. Pourtois, S. De Gendt, V. V. Afanas'ev, M. K. Van Bael, *Materials Research Bulletin* **2012**, *47*, 511-517.

[13] A. Hardy, S. Van Elshocht, C. De Dobbelaere, J. Hadermann, G. Pourtois, S. De Gendt, V. V. Afanas'ev, M. K. Van Bael, *Materials Research Bulletin* **2012**, *47*, 511-517.

[14] K. Takeshi, K. Yoshihito, I. Yasushi, I. Hiroshi, *Japanese Journal of Applied Physics* **2002**, *41*, L1164.

[15] aJ. Duan, Y. Liu, X. Pan, Y. Zhang, J. Yu, K. Nakajim, H. Taniguchi, *Catalysis Communications* **2013**, *39*, 65-69; bA. K. R. Police, S. Basavaraju, D. K. Valluri, M. Subrahmanyam, *Journal of Materials Science & Technology* **2013**, *29*, 639-649; cL. Zhang, W. Wang, S. Sun, J. Xu, M. Shang, J. Ren, *Applied Catalysis B: Environmental* **2010**, *100*, 97-101; dL. Zhang, W. Wang, S. Sun, D. Jiang, E. Gao, *CrystEngComm* **2013**, *15*, 10043-10048.

[16] G. Zaccariello, E. Moretti, L. Storaro, P. Riello, P. Canton, V. Gombac, T. Montini, E. Rodríguez-Castellón, A. Benedetti, *RSC Advances* **2014**, *4*, 37826.

[17] J. Ren, G. Liu, Y. Wang, Q. Shi, *Materials Letters* **2012**, *76*, 184-186.

[18] J. Tauc, R. Grigorovici, A. Vancu, *physica status solidi (b)* **1966**, *15*, 627-637.

[19] A. V. Naumkin, A. Kraut-Vass, C. J. Powell, S. W. Gaarenstroom, *NIST X-ray Photoelectron Spectroscopy Database*, **2012**.

[20] H. Tang, K. Prasad, R. Sanjinès, P. E. Schmid, F. Lévy, *Journal of Applied Physics* **1994**, *75*, 2042-2047.

6 *In vitro* tests on culture of human PBMCs

Preliminary *in vitro* tests on culture of human PBMCs were conducted on MSN, 10TiO_2@MSN, TiO_2 (Degussa, P25, Germany), and on *x*Bi/Ti@MSN_800 series. In this chapter, the results of the metabolic activity of the cells, the apoptosis, the nuclear morphology and the oxidative stress are reported.

6.1 Results and discussion

Citotoxicity tests

As described in detail in Chapter 2, cytotoxicity tests were performed on MSN, 10TiO_2@MSN and TiO_2 samples by MTT assay in order to study the metabolic activity of the cells exposed to the samples. In MSN, 10TiO_2@MSN and TiO_2, for lymphocytes exposed to the vehicle alone (complete RPMI medium, 10% FCS used for diluting the particles to be applied to the cells) no evident variations on the metabolic activity were observed at 6 h and 24 h for both PHA-treated and untreated lymphocytes. Instead, cell death is associated with a 48-hour exposure of the PHA-activated cells to the vehicles with the two highest doses of TiO_2 and MSN; resting not-PHA treated cells result less sensitive, since the MTT signal decreases only with the highest TiO_2 dose of 100 µg/ml. The cell viability of lymphocytes exposed to increasing amounts of the test samples as assessed by MTT gave results overlapping to those obtained with the Annexin V/PI method. Relevant data are reported in Figure 1.

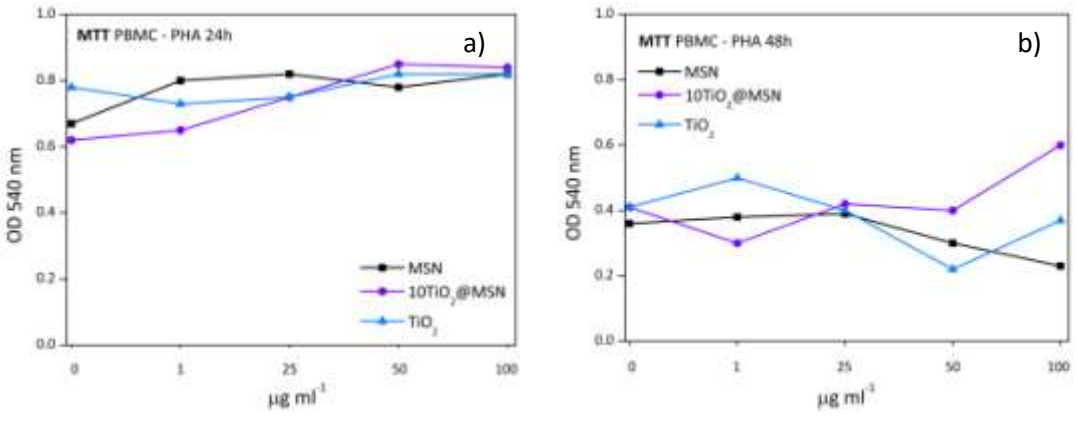

Figure 1 MTT assay after 24h (a) and 48h (b) for MSN, 10TiO_2@MSN and TiO_2 samples.

For *x*Bi/Ti@MSN_800 series the citotoxicity was also determined. After 6h a reduction of the signal is revealed only for 1.15Bi/Ti@MSN_800 at the highest concentrations (100 and 200 μg mL^{-1}). This means that the highest reduction of the metabolic activity occurs in this sample. The other samples do not show significant effects, as reported in Figure 2. After 48h, as the concentration increases, a reduction of the viable cells occurs for all the samples, independently from their nature (data not shown).

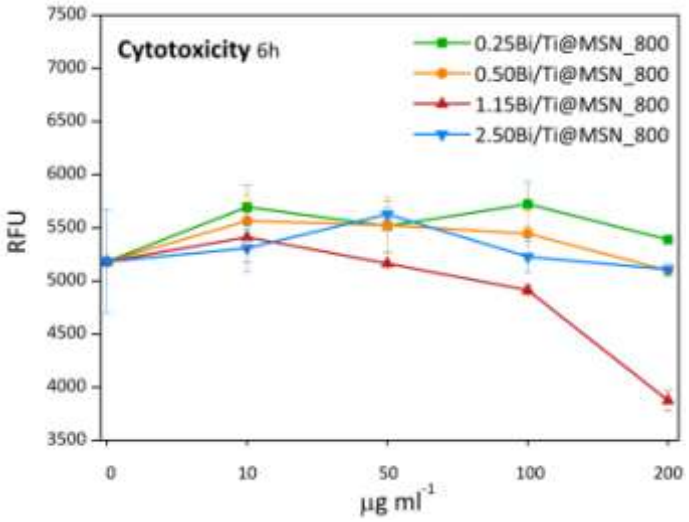

Figure 2 Metabolic activity after 6h for *x*Bi/Ti@MSN_800 samples.

Apoptosis

Human PBMC maintained in complete culture medium were 90-95% viable from 6 h up to 48 h in culture. As expected for primary cells in vitro, viability decreased down to 80-85% after 72 h in culture (data not shown). Changes in cell viability of PHA-activated PBMCs showed a more complex pattern.

For all the nanoparticles tested, dose-dependent early apoptosis was detected after 6h either in both PHA- (Figure 3a) and not PHA-treated cells (data not shown). After 24 h, also late apoptotic cells were detected in the PHA-activated cultures (Figure 3c), presumably deriving from the early apoptotic ones having had accumulated further damage (Figure 3b), whereas the non stimulated cells show no changes compared with the earlier timepoint (data not shown). For PHA-stimulated cells only, early apoptotic cells increased further at 48h, showing a dose-dependent relationship for TiO_2 (Figure 3d). Also late apoptotic cells were more abundant at this timepoint (Figure 3e), but not dependency on the dose was evident for any type of nanoparticles.

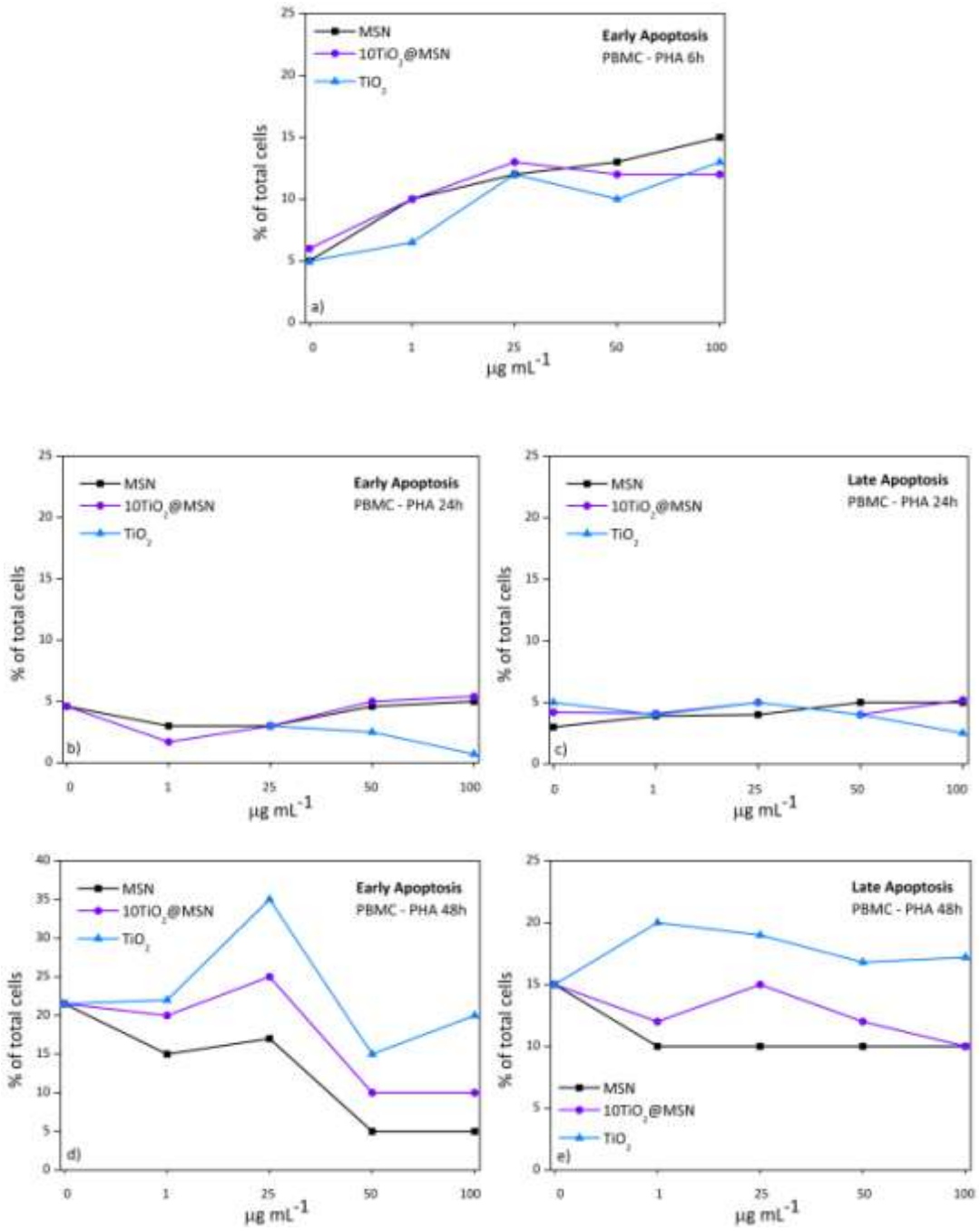

Figure 3 Early and late apoptosis after 6h, 24h and 48h on PBMCs-PHA for MSN, $10TiO_2$@MSN and TiO_2 samples.

In order to confirm the results on apoptosis induction for cells exposed to 25 µg/mL, a nuclear staining was performed and reported in Figure 4. Normal green highly condensed and weakly condensed chromatin with organized nucleoli and structures, corresponding to viable cells, are present in both cell samples, as well as the typically enlarged bright green nuclei with less condensate chromatin due to DNA replication; also one telophase is evident in the TiO_2-treated sample. In the TiO_2 sample are more abundantly present early apoptotic cells are

characterized by weakly green stained nuclei showing less organized chromatin, where the nucleolus is clearly visible. Late apopototic cells, more represented in TiO_2-exposed cells, are visible as bright green micronuclei or disrupted nuclei.

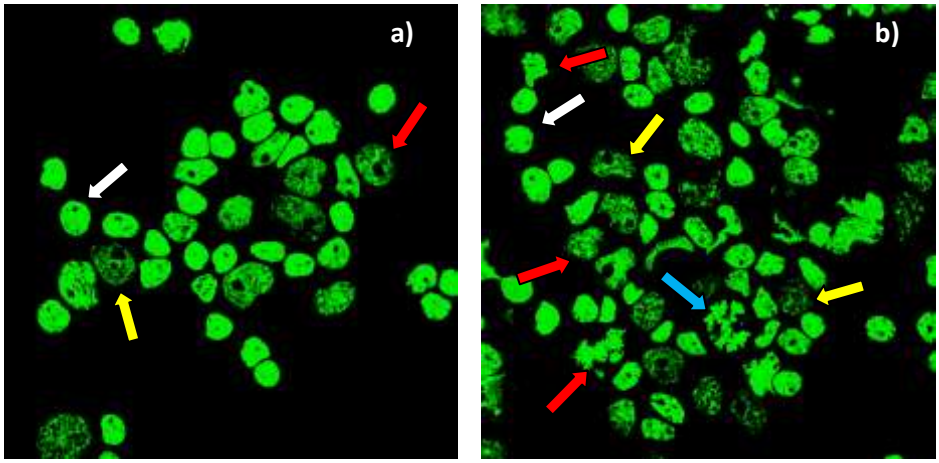

Figure 4 Confocal fluorescence images of nuclear morphology of MSN (25 µg/ml) (a) and TiO_2 (25 µg/ml) (b). White arrow: viable; yellow arrow: early apopototic; red arrow: late apoptotic; blue arrow: anaphase.

Oxidative stress

The level of the oxidative stress was evaluated through the indirect measure of the reactive oxygen species (ROS).

For MSN, TiO_2 and 10 TiO_2@MSN, in PBMCs, either PHA-stimulated or not, ROS increased in a time-dependent manner up to 48h and decreased at 72 hours. PHA-stimulated lymphocytes, showed a generally higher ROS level (not shown). However, in both conditions, TiO_2 induced the ROS increment in a dose-dependent way at 6h, 24h and 48h. Also the exposure to the two highest doses of 10 TiO_2@MSN was associated with induction of ROS at 24h and 48h, but at a less extent. Representative diagrams of the results are shown in Figure 5.

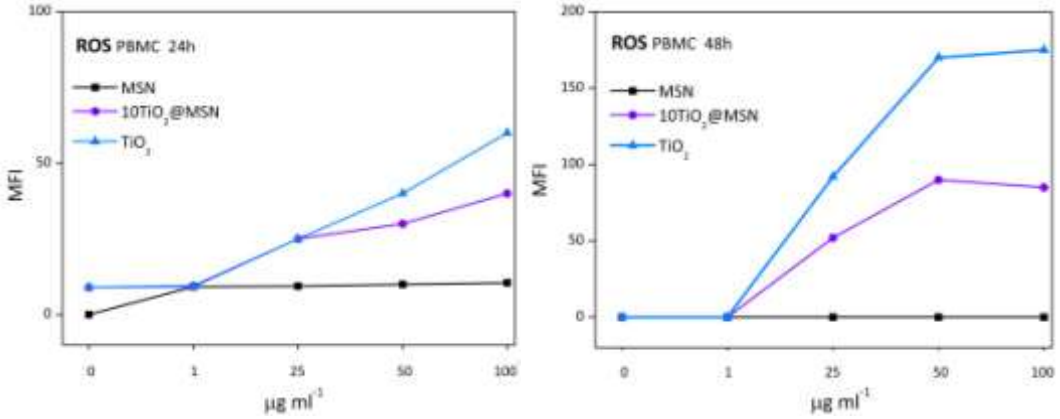

Figure 5 ROS evaluation after 24h (a) and 48h (b) on MSN, $10TiO_2$@MSN and TiO_2 samples.

For *x*Bi/Ti@MSN_800 series, after 24h and 48h of exposition to the samples at the cytotoxic (50 µg mL^{-1}) and no cytotoxic (10 µg mL^{-1}) doses, the level of the oxidative stress of the cells increases compared to the cells not exposed, as reported in Figure 6. This effect could be due to the different nature of the nanosystems. Moreover, a slightly higher value in ROS was registered after 24 hours of exposure only for 1.15Bi/Ti@MSN_800 at a concentration that does not shown cytotoxic activity, while no difference in ROS content was observed for the *x*Bi/Ti@MSN_800 series at 50 µg mL^{-1}. From these results, no evident difference between the samples was evidenced. Finally, it can be concluded that the cytotoxic effects are not ascribed to oxidative stress, but they could be associated to other mechanisms that lead to membrane's damages.

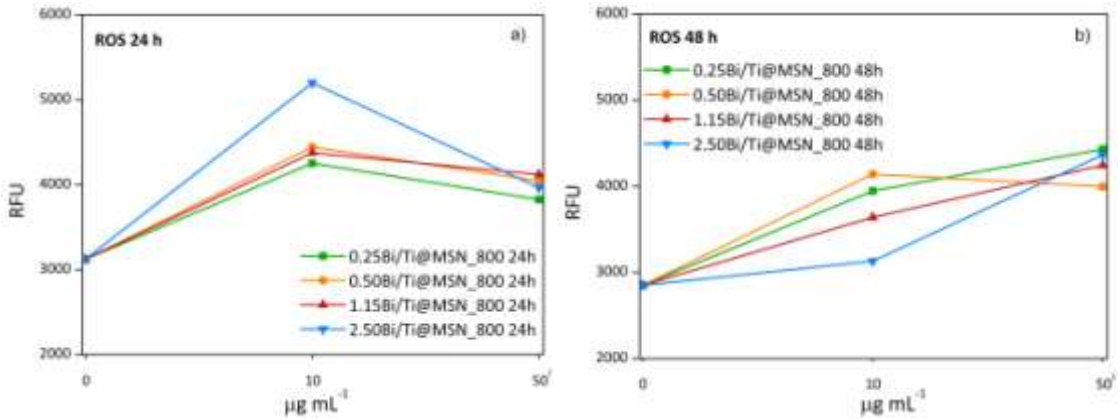

Figure 6 ROS evaluation after 24h (a) and 48h (b) on *x*Bi/Ti@MSN_800 series.

6.2 Conclusions

With the experimental conditions used in this study, MSN, 10TiO_2@MSN and TiO_2 samples appear to promptly induce low degree (not much different form that found for primary PBMCs in vitro) of apoptosis in human PBMCs cultures. However, after 48h of exposure to TiO_2 sample induces significant apoptosis in PHA-activated target lymphocytes and this effect appear to be mediated by TiO_2-mediated oxidative stress. A role in producing this effect might be addressed to soluble compounds possibly released by TiO_2-nano in the culture medium, as suggested by the reduction of the metabolic activity shown by the cells exposed to medium conditioned with TiO_2-nano. ROS have been detected also in cells exposed to the two highest concentrations of 10TiO_2@MSN: since MSN alone do not induces ROS this finding might meet the concept of a soluble form of TiO_2-mediated cytotoxic activity on PBMCs. Fluorescent microscopy confirms the higher apoptotic damage at nuclear level associated with the TiO_2 exposure.

In *x*Bi/Ti@MSN_800 series a reduction in the metabolic activity of exposed cells was observed only for 1.15Bi/Ti@MSN_800 at concentrations higher than 50 µg/mL but no ROS increase was registered at the investigated times of exposure. Because of the lack in ROS differences no analysis of the apoptosis profile was performed so far for *x*Bi/Ti@MSN_800 series. These findings have only to be considered preliminary tests conducted on a model cell characterized by high sensitivity to stimuli and representing a good preliminary cell standard for tests on the biological properties of the new material formulations. However, the samples will be tested with specific *in vitro* models, such as 3D dermis equivalent, or *in vivo* tests in order to obtain useful information for the understanding of the biocompatibily of these formulations with the respect to their final application.

7 Sunscreen prototype

As emerged from the results of this thesis, widely discussed in Chapter 3, 4 and 5, the *x*Bi/Ti@MSN_*y* system reveals the best characteristics for our purpose. In particular, the 1.15Bi/Ti@MSN_800 is the sample that best meets the two requirements of an inorganic UV filter, in fact it shows excellent UV blocking property up to 388 nm and a negligible photocatalytic activity.

From this result, in collaboration with the dermo-cosmetic company Kalis s.r.l (Treviso, Italy), a prototype was formulated in order to test the cosmetic properties of 1.15Bi/Ti@MSN_800 into a real sunscreen. SPF rating, λ*c* value, viscosity and pH were determined, comparing the prototype with a sun milk containing a commercial inorganic UV filter.

7.1 Samples preparation

By adding 20 g of 1.15Bi/Ti@MSN_800 sample, an O/W sun milk (labeled as SM1) was prepared for the determination of the Sun Protection Factor (SPF) in vitro. The SM1 sample was compared to a sun milk that uses the commercial UV filter known as Parsol TX[1] (SM2) sample. The list of ingredients of the prepared sun milk is reported in Table 1.

Table 1 List of ingredients and relative function in the prepared sun milk.

Ingredient	Function
Oil phase	
Octyl palmitate	Emollient
Arlatone 985	Co-emulsifier
Mulsifan CSA21	Emulsifier
Vitamin E acetate	Antioxidant
Abil 350	Emollient
Aperoxid TLA	Antioxidant
Water phase	
Water	
Glycerol	Humectant
Bioscontrol Sinergy BAS	Preservative
EDTA	Chelating

[1] Parsol TX consists of a 100% rutile – type titanium dioxide (TiO_2) core with a very tight double coating of silica and dimethicone.

7.2 Results and discussions

The SPF were measured using an UV-vis Jasco V 530 Spectrophotometer. The sun milk samples were applied on a Transpore Tape® (2mg/cm^3, 5x5 cm^2) [1] and the transmittance spectra were collected between 280 and 400nm. From the transmittance data, the UVA/UVB ratio and the critical wavelength λ_c (nm) were also calculated. The results are shown in Table 2.

Table 2 SPF, UVA/UVB, λ_c, η and pH values of the prepared sunscreen prototypes SM1 and SM2.

Sunscreen sample	UV filter	SPF	UVA/UVB	λ_c (nm)	η (cPS)	pH
SM1	Bi/Ti-MSN_800	3.4 ± 0.4	0.83 ± 0.01	385 ± 1	9936	6.33
SM2	Parsol TX	3.7 ± 0.2	0.76 ± 0.02	385 ± 1	6240	4.56

The research shows that the synthesized UV filter has satisfied some properties:

(i) the SPF value is 3.4 and it corresponds to a filter efficiency[2] equal to 1.13. This value is comparable to that obtained for SM1 (equal to 1.23);

(ii) according to the UK Boot's Star System[2], the UVA/UVB ratio value obtained represents a maximum UVA protection (4 stars, >0.8);

(iii) the λ*c* value satisfies the requirements of the European Commission exceeding the established threshold[3].

The viscosity (η) and the pH values of the sunscreens were measured by a Brookfield RTV DV II viscometer and by a Metrohm 713 0,001 pH-meter, respectively. Due to the presence of the silica, that acts as texturing agent, the viscosity of the SM1 sample is higher than the viscosity of the SM2 sample. Thanks to the light basicity of silica, the pH is very close to the physiological pH of the skin, consequently the addition of alkalizing agents (*i.e.* NaOH) into the cosmetic formulation is not needed. Finally, SM1 sample has a good spreadability and gives a pleasant feeling when applied to the skin, being light and not oily.

[2] The filter efficiency is the ratio of SPF and UV filter concentration (%): the higher this value, the less filter is required to achieve a certain SPF value.

7.3 Conclusions

In summary, a sunscreen prototype was prepared in order to evaluate the properties of the synthesized UV filter from a cosmetic point of view.

The results proved to live up to expectations, since the SPF is comparable with a commercial sunscreen formulation and both the UVA protection and the critical wavelength values satisfy the requirements established by the European Commission. Moreover, the prepared sunscreen has excellent properties, with good viscosity and pH value.

References

[1] S. Schalka, V. M. S. d. Reis, *Anais Brasileiros de Dermatologia* **2011**, *86*, 507-515.

[2] *The Boots Co PLC, Nottingham, England* **1991**.

[3] A. Springsteen, R. Yurek, M. Frazier, K. F. Carr, *Analytica Chimica Acta* **1999**, *380*, 155-164.

8 General conclusions

The purpose of the research activity was focused on the development of an innovative UV filter to apply in cosmetic field for the protection of human skin against UV radiations.

Since the inorganic sunscreens such has TiO_2 and ZnO are strong photocatalysts, able to damage the organic compounds, recently new nanomaterials has been proposed.

The goal of the research activity was meant to accomplish a nanostructured UV filter with a wide range of ultraviolet protection and, at the same time, a reduced photocatalytic activity.

Mesoporous silica nanoparticles were chosen as matrix to host the inorganic sunscreen, since its channels could be able to control the growth of the UV filter, with such sizes as to avoid the whitening effect.

The first attempt was to grow titanium dioxide nanoparticles inside the pores of the silica matrix, via wet impregnation. The study was conducted loading different concentration of TiO_2, in order to establish at what threshold the matrix was able to accommodate the particles. The sample with the minimum concentration of titania exhibited the best UV performance, however it showed a high photocatalytic activity, since the organic molecules used for the photodegradation tests were completely decomposed after the UV irradiation.

From these preliminary results, a strategy was adopted: to avoid the direct contact between the photocatalyst and the surrounding environment, the aforementioned synthesized UV filters were covered on the surface with a non-porous silica shell via the Stöber method. A detailed study was conducted modifying the experimental conditions in order to understand the role of the reagents and of the reaction time on the formation of the coating. Shell thickness with a range from 8±1 to 193±10 nm were observed The obtained results evidenced that the precursor concentration of the silica layer (TEOS) play an important role on the coating. The shell led to a complete reduction of the photocatalytic activity, since it acted as a physical barrier between the active photocatalyst and the external environment. Moreover, the presence of the shell does not influence the UV properties of the filters.

Finally, another approach was followed for the design of an efficient sunscreen by the adding of a Bismuth salt to the MSN loaded with TiO_2 nanoparticles to form bismuth titanates ($Bi_xTi_yO_z$). The role of the precursor concentration and of the annealing temperature were examined to evaluate how they influenced the morphology of the system and the growth of the nanoparticles. From the experimental results, it was emerged that the introduction of Bismuth ions led to a self-sealing process, since they acted as low melting-point agent for the silica ma-

trix. Thanks to this effect, the closure of the channels at the surface of MSN occurred and the inorganic nanoparticles $Bi_xTi_yO_z$ resulted to be embedded inside the matrix. This effect was evident already at the lowest Bi concentration and it was more evident at the highest thermal treatment. The introduction of Bi ions positively influenced the UV properties with an absorption edge up to 388 nm and the photocatalytic properties since the semiconductor could not available to the external environment. In conclusion, with this strategy, the development of bismuth-based safe self-sealing nanomaterials as inorganic sunscreen UV filters was possible. The bismuth ions, playing a double role in the spreading of the UV shield properties and in the suppression of the photocatalytic properties, make the proposed nanosystem an excellent candidate for the development of the next generation nanomaterials for the sun shields. Moreover, the interesting properties of bismuth emerged during this studies can be exploited in the design of a wide range UV filter nanomaterials with the aim of cutting their photocatalytic ability.

In collaboration with a dermo-cosmetic company, Kalis s.r.l (Treviso, Italy), a sunscreen formulation was prepared using the synthesized UV filter with the best performances in order to evaluate its properties also from a cosmetic point of view. The prototype showed excellent properties, with a suitable pH value and good viscosity, due to the basicity and the texturizing properties of the silica matrix. The calculated SPF, the UVA protection and the critical wavelength were comparable to the values obtained for a commercial sunscreen.

In conclusion, the results indicate that the bismuth titanate in silica matrix can represent a valid alternative to the traditional materials based on Titanium bioxide and Zinc oxide. In fact, the interesting properties emerged from this study can be widely exploited in the design of a wide range UV filter nanomaterials with the aim of cutting their photocatalytic ability.

Acknowledgments

I wish to acknowledge, above all, my tutor and supervisor Prof. Alvise Benedetti, for giving me the possibility to work as a member of his group and guiding my research activity during these years.

I would like to acknowledge Prof. Pietro Riello for his constant help and precious suggestions which helped me to improve the quality of this doctoral thesis.

I am grateful to a lot of people for their contribution to this work, in particular I kindly acknowledge: Prof. Enrico Sabbioni for giving me the opportunity to collaborate with important research centers; Prof. Fabio Brunetta and all his staff of the dermo-cosmetic company Kalis srl for the formulation of the solar prototypes; Prof. Enrique Rodríguez-Castellón of the Universidad de Málaga for performing XPS analysis; Dr. Simone Manenti and Prof. Flavia Groppi of LASA (Laboratorio Acceleratori e Superconduttività Applicata, University of Milan), INFN (Istituto Nazionale di Fisica Nucleare, Milano), and LENA (Laboratory of Applied Nuclear Energy, University of Pavia) for the NAA measurements; Prof. Elti Cataruzza and Prof. Antonella Glisenti of Università degli Studi di Padova for the XPS analysis; Prof. Mario di Gioacchino and Dr. Claudia Petrarca for performing the *in vitro* culture tests; Prof. A. Alimonti, Dr. Beatrice Bocca and Dr. Flavia Ruggieri for SF-ICP-MS analysis; Prof. Paolo Fornasiero, Dr. Tiziano Montini and Dr. Valentina Gombac of Università di Trieste for carrying out the photocatalytic experiment; Prof. Rossano Amadelli and Dr. Luca Samiolo of Università degli Studi di Ferrara for the DR-UV measurements; Prof. Patrizia Canton, Dr. Davide Cristofori and Dr. Nicolò Mazzucco for the FE-SEM and TEM analysis; Dr. Loretta Storaro and her research group (Dr. Elisa Moretti, Mr. Aldo Talon and Mrs. Martina Marchiori) for giving me the possibility to access in the laboratory and for carrying out porosimetric measurements; Mr. Tiziano Finotto for performing XRPD analysis and for his immeasurable availability; Dr. Erica Cretaio and Dr. Agnese Antognoli for their support for the discussion about the citotoxic results.

I also wish to thank Prof. Hitoshi Masaki and Dr. Taeko Mizutani of Tokyo University of Technology for giving me the possibility to work in their estimeed research group and for kindly helping me during my pleasant experience in Tokyo. I will always remember Prof. Masaki, Dr. Mizutani and all the TUT students fondly: they have made this experience the most beautiful of my life. 心から 有り難う, thank you so much.

I would like to thank “Via Torino”: thank to all my collegues, some of whom have also become my dear friends.

Estratto per riassunto della tesi di dottorato

L'estratto (max. 1000 battute) deve essere redatto sia in lingua italiana che in lingua inglese e nella lingua straniera eventualmente indicata dal Collegio dei docenti.

L'estratto va firmato e rilegato come ultimo foglio della tesi.

Studente: Gloria Zaccariello matricola: 826290

Dottorato: Scienze Chimiche

Ciclo: XXVII

Titolo della tesi[1] **:** Inorganic nanosized UV filters for cosmetic applications

Estratto: L'attività di ricerca di questo lavoro di tesi riguarda lo studio di filtri inorganici con un ampio range di schermatura UV e ridotta attività fotocatalitica da applicare in cosmetica per la protezione della pelle contro gli effetti dei raggi UV. Sono stati sintetizzati campioni a base di TiO_2 in nanoparticelle di silice mesoporosa (MSN), dimostrando però un'elevata attività fotocatalitica. Al fine di evitare il contatto diretto tra il fotocatalizzatore e l'ambiente circostante, i filtri sintetizzati sono stati rivestiti con una shell di silice non porosa, portando ad un abbattimento dell'attività fotocatalitica, senza pregiudicare le proprietà UV. Infine, sono stati sviluppati nanomateriali autosigillanti a base di $Bi_xTi_yO_z$ in MSN. Il doppio ruolo degli ioni Bi^{3+} nell'aumento delle proprietà UV e nell'abbattimento della fotocatalisi fa sì che il materiale proposto sia un perfetto candidato per lo sviluppo di filtri UV di prossima generazione. Inoltre, le interessanti proprietà emerse possono essere ampiamente sfruttate nell'ambito dei filtri solari con l'obbiettivo di abbattere il fotodegrado delle matrici organiche presenti nella formulazione.

Abstract: The research activity of this PhD thesis deals with the synthesis of inorganic UV filters with a wide UV shielding properties and low photocatalytic activity to use in cosmetic for the protection of the skin against UV rays. TiO_2-based nanosystem were loaded in mesoporous silica nanoparticles (MSN), showing a high photocatalytic activity. In order to avoid the direct contact between the photocatalyst and the external environment, the synthesized filters were coated with a non porous silica layer. Finally, a new self-sealing material based on $Bi_xTi_yO_z$ in MSN was developed. The growing process of this new nanosystem is discussed underlining the key role of the Bi^{3+} ion that, acting as a low-melting point agent for the silica framework, led to a self-sealing mechanism. The excellent UV shielding properties combined with a radical suppression of the photocatalytic activity make the proposed nanosystem a perfect candidate for the development of the next generation nanomaterials for sunscreen formulations.

[1] Il titolo deve essere quello definitivo, uguale a quello che risulta stampato sulla copertina dell'elaborato consegnato.

Firma dello studente

_____

Università
Ca'Foscari
Venezia

DEPOSITO ELETTRONICO DELLA TESI DI DOTTORATO

DICHIARAZIONE SOSTITUTIVA DELL'ATTO DI NOTORIETA'

(Art. 47 D.P.R. 445 del 28/12/2000 e relative modifiche)

Io sottoscritto ……

nat … a …… (prov. ……) il ……

residente a …… in …… n. ……

Matricola (se posseduta) …… Autore della tesi di dottorato dal titolo:

……

……

……

Dottorato di ricerca in ……

(in cotutela con ……)

Ciclo ……

Anno di conseguimento del titolo ……

DICHIARO

di essere a conoscenza:

1) del fatto che in caso di dichiarazioni mendaci, oltre alle sanzioni previste dal codice penale e dalle Leggi speciali per l'ipotesi di falsità in atti ed uso di atti falsi, decado fin dall'inizio e senza necessità di nessuna formalità dai benefici conseguenti al provvedimento emanato sulla base di tali dichiarazioni;

2) dell'obbligo per l'Università di provvedere, per via telematica, al deposito di legge delle tesi di dottorato presso le Biblioteche Nazionali Centrali di Roma e di Firenze al fine di assicurarne la conservazione e la consultabilità da parte di terzi;

3) che l'Università si riserva i diritti di riproduzione per scopi didattici, con citazione della fonte;

4) del fatto che il testo integrale della tesi di dottorato di cui alla presente dichiarazione viene archiviato e reso consultabile via internet attraverso l'Archivio Istituzionale ad Accesso Aperto dell'Università Ca' Foscari, oltre che attraverso i cataloghi delle Biblioteche Nazionali Centrali di Roma e Firenze;

5) del fatto che, ai sensi e per gli effetti di cui al D.Lgs. n. 196/2003, i dati personali raccolti saranno trattati, anche con strumenti informatici, esclusivamente nell'ambito del procedimento per il quale la presentazione viene resa;

6) del fatto che la copia della tesi in formato elettronico depositato nell'Archivio Istituzionale ad Accesso Aperto è del tutto corrispondente alla tesi in formato cartaceo, controfirmata dal tutor, consegnata presso la segreteria didattica del dipartimento di riferimento del corso di dottorato ai fini del deposito presso l'Archivio di Ateneo, e che di conseguenza va esclusa qualsiasi responsabilità dell'Ateneo stesso per quanto riguarda eventuali errori, imprecisioni o omissioni nei contenuti della tesi;

7) del fatto che la copia consegnata in formato cartaceo, controfirmata dal tutor, depositata nell'Archivio di Ateneo, è l'unica alla quale farà riferimento l'Università per rilasciare, a richiesta, la dichiarazione di conformità di eventuali copie.

Data _____ **Firma** _____

AUTORIZZO

- l'Università a riprodurre ai fini dell'immissione in rete e a comunicare al pubblico tramite servizio on line entro l'Archivio Istituzionale ad Accesso Aperto il testo integrale della tesi depositata;
- l'Università a consentire:
  - la riproduzione a fini personali e di ricerca, escludendo ogni utilizzo di carattere commerciale;
  - la citazione purché completa di tutti i dati bibliografici (nome e cognome dell'autore, titolo della tesi, relatore e correlatore, l'università, l'anno accademico e il numero delle pagine citate).

DICHIARO

1) che il contenuto e l'organizzazione della tesi è opera originale da me realizzata e non infrange in alcun modo il diritto d'autore né gli obblighi connessi alla salvaguardia di diritti morali od economici di altri autori o di altri aventi diritto, sia per testi, immagini, foto, tabelle, o altre parti di cui la tesi è composta, né compromette in alcun modo i diritti di terzi relativi alla sicurezza dei dati personali;
2) che la tesi di dottorato non è il risultato di attività rientranti nella normativa sulla proprietà industriale, non è stata prodotta nell'ambito di progetti finanziati da soggetti pubblici o privati con vincoli alla divulgazione dei risultati, non è oggetto di eventuali registrazione di tipo brevettuale o di tutela;
3) che pertanto l'Università è in ogni caso esente da responsabilità di qualsivoglia natura civile, amministrativa o penale e sarà tenuta indenne a qualsiasi richiesta o rivendicazione da parte di terzi.

A tal fine:
- dichiaro di aver autoarchiviato la copia integrale della tesi in formato elettronico nell'Archivio Istituzionale ad Accesso Aperto dell'Università Ca' Foscari;
- consegno la copia integrale della tesi in formato cartaceo presso la segreteria didattica del dipartimento di riferimento del corso di dottorato ai fini del deposito presso l'Archivio di Ateneo.

Data _____ **Firma** _____

La presente dichiarazione è sottoscritta dall'interessato in presenza del dipendente addetto, ovvero sottoscritta e inviata, unitamente a copia fotostatica non autenticata di un documento di identità del dichiarante, all'ufficio competente via fax, ovvero tramite un incaricato, oppure a mezzo posta

Firma del dipendente addetto ……

Ai sensi dell'art. 13 del D.Lgs. n. 196/03 si informa che il titolare del trattamento dei dati forniti è l'Università Ca' Foscari - Venezia.
I dati sono acquisiti e trattati esclusivamente per l'espletamento delle finalità istituzionali d'Ateneo; l'eventuale rifiuto di fornire i propri dati personali potrebbe comportare il mancato espletamento degli adempimenti necessari e delle procedure amministrative di gestione delle carriere studenti. Sono comunque riconosciuti i diritti di cui all'art. 7 D. Lgs. n. 196/03.